



TECHNISCHE
UNIVERSITÄT
WIEN

Vienna University of Technology

Unterschrift des Betreuers

DIPLOMARBEIT

FIELD RESPONSE STUDIES ON THE SUBSTITUTION-DRIVEN MODIFICATIONS OF TERNARY $\text{Ce}_3\text{Pd}_4\text{Si}_4$

Ausgeführt am Institut für Festkörperphysik der technischen Universität Wien unter der
Anleitung von

Ao.Univ. Prof. Univ. Prof. Dipl.-Ing. Dr. techn. Ernst Bauer

durch

Nicolas Robisch, BSc
Matrikelnummer: 0726671
Brigittagasse 2/23, 1200 Wien

December 8, 2014

Unterschrift Student

Abstract

Strongly correlated electron systems are known to exhibit a variety of extraordinary low temperature properties. The presence of $4f$ -electrons in cerium-based intermetallics leads to an interplay of RKKY interactions and the Kondo effect accompanied by the occurrence of ground states like magnetic order or even superconductivity. Moreover, crystalline electric field effects play an important role for the behaviour of these compounds. External parameters like magnetic fields may strongly modify the system's properties at low temperatures.

In this diploma thesis, the ternary system $\text{Ce}_3\text{Pd}_4\text{Si}_4$ has been studied as regards its physical properties. The aim of this diploma thesis was to describe which modifications occur in the aforementioned system, when one of the components is replaced by an element of the same group in the periodic table. Therefore, six specimen were prepared; two where silicon was substituted by germanium in different stoichiometric ratios and four where nickel replaced palladium. Resistivity measurements were performed using a four-point sensing method in the low temperature region (0.4 K to 300 K), inter alia in the presence of external magnetic fields up to 12 T. The magnetic susceptibility was measured in terms of the temperature-dependent and the field-dependent magnetisation. Additionally, heat capacity measurements were carried out in order to particularise the physical behaviour in line with the theoretical models.

Subsequent analysis revealed for the Si – Ge substitution series Kondo lattice behaviour in the presence of crystalline electric field splitting. Yet the smallest substitution rate caused a transition into an antiferromagnetic groundstate in the measurement range, which wasn't observed in initial $\text{Ce}_3\text{Pd}_4\text{Si}_4$. In $\text{Ce}_3\text{Pd}_4\text{Si}_{2.8}\text{Ge}_{1.2}$, even two magnetic phase transitions were spotted. The volume of the unit cell increases, as silicon is exchanged for germanium, thus a release of chemical pressure is eminent. The four specimen of the Pd – Ni substitution series exhibit a strange and unexpected modification of magnetic properties. While lower substitution rates yield as well the appearance of an antiferromagnetic ground state, the Kondo behaviour changes drastically for higher substitutions. A shift of the resistivity maximum from temperatures around 5 K to 60 K is accompanied by a drop of the magnetoresistivity and the magnetic entropy by one order of magnitude.

These findings are considerable, as they prove the fact that the substitution of a non-magnetic host material in a compound can modify magnetic properties remarkably.

Kurzfassung

Stark korrelierte Elektronensysteme können ungewöhnliche physikalische Eigenschaften bei tiefen Temperaturen zeigen. Die Präsenz magnetischer Momente von $4f$ -Elektronen in Cer-basierten intermetallischen Verbindungen kann über ein Wechselspiel des Kondoeffekts mit der RKKY-Wechselwirkung zum Auftreten von Grundzuständen wie magnetischer Ordnung oder unkonventioneller Supraleitung führen. Auch kristallelektrische Felder spielen bei dieser Art von Systemen eine große Rolle. Externe Parameter wie zum Beispiel Magnetfelder können das Tieftemperaturverhalten dieser Verbindungen modifizieren.

In dieser Diplomarbeit wurde das ternäre System $\text{Ce}_3\text{Pd}_4\text{Si}_4$ in Hinblick auf seine physikalischen Eigenschaften untersucht. Das Ziel war, herauszufinden, welchen Veränderungen das System unterliegt, wenn eine der Komponenten durch ein Element derselben Gruppe des Periodensystems ersetzt wird. Insgesamt wurden sechs verwertbare Proben hergestellt, zwei in denen Silizium in verschiedenen stöchiometrischen Verhältnissen durch Germanium ersetzt wurde und vier bei denen das Übergangselement Nickel Palladium ersetzte. An diesen Proben wurde mit einer Vierpunktmethode der spezifische Widerstand ermittelt. Dieses geschah in einem Temperaturbereich von 0.4 bis 300 Kelvin, wobei auch in extern erzeugten Magnetfeldern mit einer Stärke von bis zu 12 Tesla gemessen wurde. Um einen genaueren Einblick in die magnetischen Eigenschaften der Materialien zu erhalten, wurden außerdem Messungen der magnetischen Suszeptibilität χ_m bzw. der Magnetisierung $M(T, H)$ in Abhängigkeit von Feld und Temperatur durchgeführt, wobei eine Variable stets konstant gehalten wurde. Messungen der Wärmekapazität des Materials rundeten die Untersuchungen ab. Diese wurden ebenfalls bei tiefen Temperaturen und in Anwesenheit externer Magnetfelder durchgeführt.

Im Rahmen der Auswertung der Daten konnte herausgefunden werden, dass die Proben der Si – Ge Substitutionsreihe Kondogitter-Verhalten in Anwesenheit einer Kristallfeldaufspaltung zeigen. Schon die kleinste Substitutionsrate führte zum Auftreten eines magnetischen Phasenübergangs innerhalb des Messbereichs in einen antiferromagnetischen Grundzustand. Dieser wurde bei der Ausgangsverbindung $\text{Ce}_3\text{Pd}_4\text{Si}_4$ nicht beobachtet. In $\text{Ce}_3\text{Pd}_4\text{Si}_{2.8}\text{Ge}_{1.2}$ wurden sogar zwei magnetische Phasenübergänge gefunden. Das Ersetzen von Silizium durch Germanium bewirkt des Weiteren eine Vergrößerung der Gitterparameter und damit der Einheitszelle, was mit einem Abfallen von sogenanntem chemischen Druck einhergeht. Die vier Proben der Pd – Ni Substitutionsreihe zeichneten sich vor allem durch die Veränderung ihrer magnetischen Eigenschaften aus. Bei niedrigeren Substitutionsraten wurde, wie auch in der Germaniumreihe, Kondogitterverhalten und ein antiferromagnetischer Grundzustand beobachtet. Jedoch zeigten sich bei höheren Substitutionsraten diverse Veränderungen, unter anderem eine Verschiebung des Maximums des spezifischen Widerstandes von 5 K zu 60 K. Gleichzeitig sanken sowohl die Werte des Magnetowiderstandes als auch der magnetischen Entropie um eine Größenordnung.

Die hier erzielten Ergebnisse sind auch deshalb hervorzuheben, da sie zeigen, dass die Substitution eines nichtmagnetischen Elements in einer Verbindung deren magnetische Eigenschaften sehr wohl fundamental verändern kann.

Danksagung

Die Entstehung einer wissenschaftlichen Abschlussarbeit ist für jedermann ein langer Weg. Deswegen ist es um so erfreulicher, wenn das Ziel erreicht ist, das man so lange angestrebt hat. Viele Hürden und Probleme müssen erst überwunden werden und oft helfen einem die wunderbaren Leute, die einen Teil des Lebensweges an der eigenen Seite gehen, in überaus hohem Maße. Deswegen sei an dieser Stelle allen, die für die Entstehung dieser Arbeit körperlichen, geistigen oder sonstigen Beistand geleistet haben aufs Herzlichste gedankt. Auch viele Menschen, die hier nicht direkt beteiligt waren, bin ich zu Dank verpflichtet, da sie mich in zahlreichen Lebenslagen, in Höhen und Tiefen, unterstützt und an mich geglaubt haben und mich dort hin gebracht haben, wo ich heute stehe. Und selbst wenn hier doch nicht die Gelegenheit ist, all die lieben und wichtigen Menschen zu erwähnen, möchte ich doch besonders einigen meinen aufrichtigsten Dank aussprechen:

Meinen Eltern Günter und Inge Robisch dafür, dass sie mich auf- und erzogen haben, mich immer unterstützt haben, mir das Studium ermöglichten und mir helfen die Steine auf meinem Lebensweg beiseite zu rollen. Auch meiner restlichen Familie gilt an dieser Stelle besonderer Dank für die gemeinsame Zeit, die sie mir in meinem Leben bis jetzt geschenkt hat.

Meiner Lebensgefährtin Birgit Steininger dafür, dass sie es schafft, mir trotz meiner teils anstrengenden Art immer wieder zuzuhören und Mut zuzusprechen, für meinen Platz in ihrem Herzen und für sehr viele Dinge, die sich auf unserem gemeinsamen Lebensweg bisher abgespielt haben und noch werden. Auch deiner Familie sei mein offener Dank für die vielen schönen Stunden ausgesprochen, liebe Birgit.

Meinem Betreuer Prof. Ernst Bauer für seine kontinuierliche Unterstützung in allen Stadien der Entstehung dieser Diplomarbeit. Sein unermüdlicher Einsatz für die Wissenschaft und die Betreuung seiner Studenten ist vorbildhaft, genauso wie die Gelassenheit mit denen er Problemen ins Auge sieht. Seine Tür steht, nicht nur symbolisch, immer für die Anliegen seiner Studenten und Kollegen offen.

All den lieben anderen Kollegen des Institutes, die mir auf die ein oder andere Art bei der Entstehung dieser Arbeit sowie der vorausgegangenen Experimente zur Seite gestanden sind, darunter Prof. Herwig Michor, Dr. Leonid Salamakha, Dr. Friedrich Kneidinger, DI Patrick Heinrich, DI Igor Knapp, Peter Hundegger u.v.m. sowie meine netten Diplomandenkollegen Pantea Pezeshkpour, Ivan Messner, Serge Tako, Joachim Jeitler, Christine Mair und Ronja Kamelreiter für die vielen Gespräche auf Augenhöhe und sonstigen Zerstreungen.

All meinen Freunden und Bekannten, die ich auf die eine oder andere Art in meinem Herzen trage (m.B.d.A): Lydia, Miriam, Katharina, Hanna, Michi, Angela, Marion, Renuka, Tobias, Philip, Sandra, Hannes, Stefan...

Allen engagierten Mitarbeitern der Fachschaft Physik dafür, dass sie sich so umfangreich dafür einsetzen, das Leben der Studenten zu erleichtern und für die vielen Feste und sonstigen Events, die sie organisiert haben.

Den Mitgliedern der Fachschafts-Theatergruppe, für den vielen Spaß, den ich in ihrer Mitte hatte.

Contents

1. Introduction	1
2. Theoretical background	3
2.1. Transport phenomena	3
2.1.1. The electrical resistivity	3
2.1.2. Heat capacity	6
2.1.3. Magnetic susceptibility	8
2.2. Strongly correlated electron systems	10
2.2.1. The Anderson model	10
2.2.2. The Coqblin-Schrieffer model	11
2.2.3. Crystalline electric field (CEF) effects	12
2.2.4. Kondo effect	12
2.2.5. Concentrated Kondo systems	14
2.2.6. Kondo lattice	14
2.2.7. RKKY-Interactions	16
2.2.8. Fermi- and non-Fermi liquid behaviour	17
3. Experimental realisation	21
3.1. Sample preparation	21
3.2. X-ray powder diffraction analyses	21
3.3. Resistivity measurements	23
3.3.1. ⁴ He bath cryostat	24
3.3.2. ³ He refrigerator system	25
3.4. Magnetization measurements	29
3.5. Heat capacity measurements	32
4. Results & discussion	35
4.1. Ce ₃ Pd ₄ Si _{4-x} Ge _x compounds	35
4.1.1. Ce ₃ Pd ₄ Si _{3.4} Ge _{0.6}	36
4.1.2. Ce ₃ Pd ₄ Si _{2.8} Ge _{1.2}	42
4.2. Ce ₃ Pd _{4-x} Ni _x Si ₄ compounds	48
4.2.1. Ce ₃ Pd _{3.75} Ni _{0.25} Si ₄	49
4.2.2. Ce ₃ Pd _{3.5} Ni _{0.5} Si ₄	53
4.2.3. Ce ₃ Pd ₃ NiSi ₄	57
4.2.4. Ce ₃ Pd ₂ Ni ₂ Si ₄	57
4.3. Overall analysis	66
4.4. Outlook	72
5. Summary	73
A. Buildup of the ³He cryostat	79
B. X-ray diffraction patterns	80

List of Figures

2.1. Anderson Hamiltonian band structure	11
2.2. Energy splitting of cerium ion	13
2.3. $\rho_{mag}(T)$ for Kondo single impurity and lattice systems	15
2.4. Rudermann-Kittel function	16
2.5. Doniach's phase diagram	17
2.6. Quantum critical point	19
3.1. Bragg-Brentano geometry	22
3.2. Four-terminal sensing method	23
3.3. Depiction of a puck	24
3.4. Scheme of the ^3He cryostat	26
3.5. Scheme of the ^3He measurement device	27
3.6. Sample glued on SQUID sample carrier	29
3.7. SQUID sample carrier	30
3.8. SQUID magnetometer	30
3.9. DC SQUID diagram	31
3.10. Scheme of heating pulses	33
3.11. Inner parts of a Nernst-calorimeter	34
4.1. Sketch of the crystal structure of $\text{Ce}_3\text{Pd}_4\text{Si}_4$ in projection along $[100]$ [1].	35
4.2. X-ray diffraction pattern of $\text{Ce}_3\text{Pd}_4\text{Si}_{3.4}\text{Ge}_{0.6}$	36
4.3. $\rho(T, B = 0)$ of $\text{Ce}_3\text{Pd}_4\text{Si}_{3.4}\text{Ge}_{0.6}$	37
4.4. $\rho(T, B \neq 0)$ of $\text{Ce}_3\text{Pd}_4\text{Si}_{3.4}\text{Ge}_{0.6}$	38
4.5. Magnetic field ramp of $\text{Ce}_3\text{Pd}_4\text{Si}_{3.4}\text{Ge}_{0.6}$	39
4.6. C_p of $\text{Ce}_3\text{Pd}_4\text{Si}_{3.4}\text{Ge}_{0.6}$	40
4.7. C_p/T of $\text{Ce}_3\text{Pd}_4\text{Si}_{3.4}\text{Ge}_{0.6}$	41
4.8. $\chi(T)$ of $\text{Ce}_3\text{Pd}_4\text{Si}_{3.4}\text{Ge}_{0.6}$	41
4.9. $M(\mu_0 H)$ of $\text{Ce}_3\text{Pd}_4\text{Si}_{3.4}\text{Ge}_{0.6}$ in detail	42
4.10. $\rho(T, B = 0)$ of $\text{Ce}_3\text{Pd}_4\text{Si}_{2.8}\text{Ge}_{1.2}$	43
4.11. $\rho(T, B \neq 0)$ of $\text{Ce}_3\text{Pd}_4\text{Si}_{2.8}\text{Ge}_{1.2}$	44
4.12. Magnetic Field ramp of $\text{Ce}_3\text{Pd}_4\text{Si}_{2.8}\text{Ge}_{1.2}$	44
4.13. $C_p(T)$ of $\text{Ce}_3\text{Pd}_4\text{Si}_{2.8}\text{Ge}_{1.2}$	45
4.14. C_p/T of $\text{Ce}_3\text{Pd}_4\text{Si}_{2.8}\text{Ge}_{1.2}$	45
4.15. $\chi(T)$ of $\text{Ce}_3\text{Pd}_4\text{Si}_{2.8}\text{Ge}_{1.2}$	46
4.16. $M(\mu_0 H)$ of $\text{Ce}_3\text{Pd}_4\text{Si}_{2.8}\text{Ge}_{1.2}$ in detail	47
4.17. Depicted lattice parameters of nickel samples	48
4.18. $\rho(T, B = 0)$ of $\text{Ce}_3\text{Pd}_{3.75}\text{Ni}_{0.25}\text{Si}_4$	49
4.19. $\rho(T, B \neq 0)$ of $\text{Ce}_3\text{Pd}_{3.75}\text{Ni}_{0.25}\text{Si}_4$	50
4.20. Magnetic field ramps of $\text{Ce}_3\text{Pd}_{3.75}\text{Ni}_{0.25}\text{Si}_4$	50
4.21. $C_p(T)$ of $\text{Ce}_3\text{Pd}_{3.75}\text{Ni}_{0.25}\text{Si}_4$	51
4.22. $C_p(T)/T$ of $\text{Ce}_3\text{Pd}_{3.75}\text{Ni}_{0.25}\text{Si}_4$	52
4.23. $\chi(T)$ of $\text{Ce}_3\text{Pd}_{3.75}\text{Ni}_{0.25}\text{Si}_4$	52

4.24. $\rho(T, B = 0)$ of $Ce_3Pd_{3.5}Ni_{0.5}Si_4$	53
4.25. $\rho(T, B \neq 0)$ of $Ce_3Pd_{3.5}Ni_{0.5}Si_4$	54
4.26. Magnetic field ramps of $Ce_3Pd_{3.5}Ni_{0.5}Si_4$	54
4.27. $C_p(T)$ of $Ce_3Pd_{3.5}Ni_{0.5}Si_4$	55
4.28. $C_p(T)/T$ of $Ce_3Pd_{3.5}Ni_{0.5}Si_4$	55
4.29. $\chi(T)$ of $Ce_3Pd_{3.5}Ni_{0.5}Si_4$	56
4.30. $\rho(T, B = 0)$ of $Ce_3Pd_3NiSi_4$	57
4.31. $\rho(T, B \neq 0)$ of $Ce_3Pd_3NiSi_4$	58
4.32. Magnetic field ramp of $Ce_3Pd_3NiSi_4$	58
4.33. $C_p(T)$ of $Ce_3Pd_3NiSi_4$	59
4.34. $C_p(T)/T$ of $Ce_3Pd_3NiSi_4$	59
4.35. $\chi(T)$ of $Ce_3Pd_3NiSi_4$	60
4.36. $\rho(T, B = 0)$ of $Ce_3Pd_2Ni_2Si_4$	61
4.37. $\rho(T, B \neq 0)$ of $Ce_3Pd_2Ni_2Si_4$	62
4.38. Fig. 4.37 plotted as ρ vs. $\ln(T)$	62
4.39. Magnetic field ramp of $Ce_3Pd_2Ni_2Si_4$	63
4.40. C_p of $Ce_3Pd_2Ni_2Si_4$	64
4.41. C_p/T of $Ce_3Pd_2Ni_2Si_4$	64
4.42. $\chi(T)$ of $Ce_3Pd_2Ni_2Si_4$	65
4.43. Comparison of the lattice parameters of all samples	66
4.44. $\rho(T, \vec{B} = 0)$ of initial $Ce_3Pd_4Si_4$	67
4.45. $\rho(T)$ of the entire nickel substitution series	68
4.46. $\rho(T, \vec{B} = 0)$ of all samples	68
4.47. $\rho(T, \vec{B} = 0)$ of all samples on a logarithmic scale	69
4.48. Comparison of $C_p(T)$ of all compounds	70
4.49. $C_p(T)$ of all samples plotted over a logarithmic temperature scale	70
4.50. Comparison of magnetic entropies	71
4.51. Comparison of effective magnetic moment and paramagnetic Curie temperature	71
4.52. $\rho(T)$ of higher Ni substitution rates by K. Sirak	72
A.1. Profile of 3He bath cryostat	79
B.1. X-ray diffraction pattern of sample 2	81
B.2. X-ray diffraction pattern of $Ce_3Pd_{3.75}Ni_{0.25}Si_4$	82
B.3. X-ray diffraction pattern of $Ce_3Pd_{3.5}Ni_{0.5}Si_4$	83
B.4. X-ray diffraction pattern of $Ce_3Pd_3NiSi_4$	84
B.5. X-ray diffraction pattern of $Ce_3Pd_2Ni_2Si_4$. Small impurity peaks can be spotted at 27° , 33° and 35°	85

1. Introduction

Strongly Correlated Electron Systems (SCES), a class of intermetallic compounds where electron-electron correlations play an important role, are known for extraordinary low temperature features. An unusually high effective electron mass can be verified in materials containing elements with $4f$ or $5f$ electrons, e.g. cerium. Therefore, these materials are called heavy fermion systems. The energy of the $4f$ or $5f$ shell is located in the vicinity of the Fermi energy; thus, fascinating phenomena like spontaneous magnetic ordering, intermediate valence, quantum critical behaviour and heavy fermion superconductivity can occur, especially if RKKY-interactions play an important role in the system. Since the 1960s, many theoretical concepts have been established by famous physicists to better comprehend why physical quantities behave that way. Many of these phenomena are attributed to the so-called Kondo effect, a specific interaction of the conduction electron spin \vec{s} with the total angular momentum \vec{j} of the element, containing the f electrons. Measuring transport phenomena, like electrical resistivity, magnetoresistivity or thermal conductivity as well as thermodynamical or magnetic properties (specific heat, magnetic susceptibility) is suitable to reveal information about the ground state properties of these systems.

For instance, a negative logarithmic contribution $-\ln(T)$, to the electrical resistivity $\rho(T)$ was derived from theoretical models by J. Kondo, which could explain an occurring minimum of this quantity. The physical behaviour, exceedingly at low temperatures, may be manipulated by varying external parameters, e.g. magnetic field, pressure or substitution of one element by another one. The latter can cause appreciable modifications of the lattice parameters of the unit cell and possibly an altered chemical pressure acting onto the system. Changes of the electronic structure are expected, if non-isoelectronic substitutions are carried out. It is also possible that systems develop strong changes in magnetic properties. An antiferromagnetic ground state may become paramagnetic or vice versa, or superconductivity may occur as well.

Specifically, within this diploma thesis, compounds containing cerium atoms and forming a $3 : 4 : 4$ structure are discussed. Starting from a recently published paper by Kneidinger et al. [1], ternary $\text{Ce}_3\text{T}_4\text{X}_4$ with $\text{T} = \text{Pd}$ and Ni and $\text{X} = \text{Si}$ and Ge shall be analysed. Based on the results in the aforementioned paper for the compound $\text{Ce}_3\text{Pd}_4\text{Si}_4$, two directions have been chosen in terms of substituting one component. More precisely, an attempt is made to substitute silicon by germanium and subsequently transition metal palladium by nickel. The structure of the intermetallic compounds shall be determined by x-ray powder diffraction analysis. Physical properties like electrical resistivity and magnetoresistance are studied from 0.4 K to 300 K and magnetic fields up to 12 T. Magnetic properties are gained specifically from SQUID magnetisation measurements. Moreover, specific heat measurements of the samples have been carried out at two devices.

This diploma thesis is arranged in the following way: Subsequent to this introduction, the theoretical concepts are presented in two parts. Firstly, the most common relevant models in terms of measurable transport properties in solids, are described. The second part aims at giving the reader a short overview of heavy electron systems. The Anderson model as well as the Coqblin-Schrieffer model are presented. Some aspects of the Kondo effect, RKKY interactions, crystalline electric field splitting and interactions between them are explained. A brief overview about Fermi- and non-Fermi liquids is given. The following experimental part in chapter 3 goes

into detail in terms of the preparation process of the compounds, their structural analysis and the operating mode of the measurement devices used. Chapter 4 represents the most important part, the results obtained and the conclusions and discussions. In several sections, each specimen is presented on its own with an overall discussion of the results as well as a graphic comparison at the end. A short outlook onto new results of the nickel alloys, obtained in our group by K. Sirak completes chapter 4. Results are summarised in chapter 5.

2. Theoretical background

The following chapter includes an introduction to the theoretical models which describe observed material properties shall be given. The first part consists of a general description of the relevant transport phenomena and macroscopic, measurable quantities. The second part aims at explaining theoretical basics on strongly correlated electron systems. As a matter of fact, many sections of this chapter can be found in detail in the lecture notes of *Festkörperphysik I* by Silke Bühler-Paschen, Michael Reissner and Herwig Michor [2] and, furthermore, in the lecture notes of *Strongly Correlated Electron Systems* by Ernst Bauer. At the beginning of each section, references are listed in a footnote.

2.1. Transport phenomena

2.1.1. The electrical resistivity

¹ The first successful attempt to develop a phenomenological description of electronic transport phenomena in (simple) metals was made by Drude in 1900 [4,5]. Actually it is seen as a model of kinetic gas theory for ideal gases. Electrons bounce off heavy core ions elastically, while not interacting amongst each other. Their movement is driven by an external force, for instance an electric field \vec{E} . The equation of motion looks like:

$$m \frac{d\vec{v}_D}{dt} + \frac{m}{\tau} \vec{v}_D = -e\vec{E}, \quad (2.1)$$

with the drift velocity \vec{v}_D , the mean free time between ionic collisions τ and the elementary charge e . Furthermore, it is imperative that $\Lambda = v_D \tau$, with Λ being the mean free path of a conduction electron. One can consequently derive a version of Ohm's law from Drude's assumptions:

$$\vec{j} = \left(\frac{ne^2\tau}{m} \right) \vec{E} = \sigma \vec{E}. \quad (2.2)$$

In this case n is the electron density, σ the conductivity and \vec{j} the current density.

Although it was discovered later that Drude's presumption was wrong², his model used to be a good approximation, especially in terms of the Wiedemann-Franz law.

Sommerfeld made important improvements by introducing a semi-classical model, stating that electrons are locked in 3-dimensional potential wells and periodic boundary conditions apply. The application of Fermi-Dirac statistics, substitutes Drude's drift velocity \vec{v}_D by the Fermi velocity \vec{v}_F ³ so that, unlike in Drude's model, only electrons near the Fermi surface, i.e. electrons at high energy levels in the potential well, contribute to the transport process. The most important fact, derived from Sommerfeld's model, is, however, the temperature dependence of the electronic contribution to specific heat.

Further improvements were made by Bloch, who established the so-called Bloch waves for describing electronic transport processes in solids. Bloch's model states that electrons in simple metals behave like free particles with a wave function modulated by a periodic potential function.

¹ [2, 3]

² Drude didn't know anything about quantum mechanics

³ $|\vec{v}_F| = \sqrt{\frac{2E_F}{m}}$

The Boltzmann equation

⁴ The Boltzmann equation (2.4) is another more sophisticated option to describe transport properties. The main idea is to compare the driving force of external fields and temperature gradients with the thermalisation effects which result from scattering and collision processes. $f(\vec{x}, \vec{p}, t)$ represents the distribution function of charge carriers in the system, which is usually of Fermi-Dirac type like (2.3). In the Fermi-Dirac distribution μ represents the chemical potential, $E(\vec{k})$ the energy and k_B the Boltzmann constant.

$$f(E(\vec{k})) = \frac{1}{\exp(E(\vec{k}) - \mu)/k_B T + 1}, \quad (2.3)$$

$$\frac{\partial f}{\partial t} = -\frac{\vec{p}}{m} \cdot \vec{\nabla}_{\vec{r}} f - \frac{e}{\hbar} (\vec{E} + \vec{v} \times \vec{B}) \cdot \vec{\nabla}_{\vec{k}} f + \left(\frac{\partial f}{\partial t} \right)_{\text{coll}}. \quad (2.4)$$

The first term in the Boltzmann equation describes diffusion processes, which are proportional to a density gradient, whilst the second term is a result of external forces, in this case the Lorentz force. The third term, however, describes the scattering processes and stands in general for a complicated integral equation. For the stationary case $\frac{\partial f}{\partial t} = 0$, one can state that those three terms should balance each other.

For a small displacement of $f(\vec{k})$ from the Fermi-Dirac distribution in thermal equilibrium f_0 and if this displacement is linear proportional to the external forces, one can introduce the linearised Boltzmann equation. By inserting $g(\vec{k}) = f(\vec{k}) - f_0(\vec{k})$ into (2.4) and neglecting terms of second order as well as the contribution of possible temperature gradients, one obtains

$$\left(-\frac{\partial f_0}{\partial E} \right) \vec{v}(\vec{k}) \cdot (e\vec{E}) = - \left(\frac{\partial f}{\partial t} \right)_{\text{coll}} + \vec{v}(\vec{k}) \cdot \vec{\nabla}_{\vec{r}} g(\vec{k}) + \frac{e}{\hbar} (\vec{v} \times \vec{B}) \cdot \vec{\nabla}_{\vec{k}} g(\vec{k}). \quad (2.5)$$

For a the stationary and homogenous case and using the so-called relaxation time approximation, Drude's equation (2.2) for free electrons can be derived from (2.5). Moreover one gets the additional information, that the relaxation time τ is connected to the Fermi energy and the mass m becomes $m^* = (\hbar k_F / v(E_F))$. This result explains, why Drude's theory could be used to describe some results with remarkable accuracy, although according to Boltzmann only electrons near the Fermi energy take place in transport processes.

In a simple metal, charge carriers are scattered mainly at static lattice imperfections (impurity atoms, grain boundaries, lattice dislocations,...) and phonons. Phonons are quasiparticles, which describe the thermally excited lattice vibrations. Nevertheless there are some additional small contributions to transport properties like electron-electron scattering (neglected by Drude) and scattering at magnetic moments. Luckily, if the aforementioned scattering processes are independent from each other, a rather simple law can be applied to connect their contributions, *Matthiessen's rule*. The mean free path of a charge carrier is given by $\Lambda = (n_S S)^{-1}$ with n_S being the density of scattering centers and S the scattering cross section. The independent products of $n_S S$ are added for more reasons of scattering. Thus we obtain *Matthiessen's rule*:

$$\frac{1}{\Lambda} = \sum_i \frac{1}{\Lambda_i} \quad \text{or} \quad \frac{1}{\tau} = \sum_i \frac{1}{\tau_i}, \quad (2.6)$$

$\tau \propto \Lambda$ yields the second part of equation (2.6). As the relaxation time is responsible for the magnitude and temperature dependence of the electrical resistivity ρ and $\rho \propto 1/\tau$, one can furthermore assume

$$\rho(T) = \sum_i \rho_i = \rho_0 + \rho_{ph}(T) + \rho_e(T) + \rho_{mag}(T) \dots \quad (2.7)$$

⁴ [2, 3]

Here, ρ_0 represents the scattering of charge carriers on static lattice imperfections, which is temperature-independent.

One can use the Boltzmann equation to derive an expression for the phononic part of the resistivity. In a long and complicated variational type calculation, Grüneisen and Bloch established the formula named after them:

$$\rho_{ph} = c_2 \Theta_D \left(\frac{T}{\Theta_D} \right)^5 \int_0^{\Theta_D/T} \frac{z^5 dz}{(\exp(z) - 1)(1 - \exp(-z))}. \quad (2.8)$$

The resistivity is proportional to the ratio of temperature and the Debye temperature Θ_D to the fifth power modulated by the so-called Debye-integral. The Debye temperature was established in Debye's model of specific heat (see specific heat part), which is used to describe phonons in the Bloch-Grüneisen formula. C_2 represents a temperature independent interaction strength of electrons with phonons. Further assumptions in the formula are the absence of Umklapp processes, the coupling of electrons is only possible with longitudinal phonons, the Fermi-surface has a spherical shape and the Brillouin zone is approximated by a Debye-sphere with radius q_D . For temperatures, which are either much smaller or much larger than Θ_D , some simplifications can be made by expanding the Debye integral using Debye's functions⁵:

- For $T \gg \Theta_D$ i.e. $z \ll 1$ in (2.8), one can expand the integral part to

$$J_5(z) \approx \int (x^3 - (1/12) \cdot x^5 \dots) dx \approx (1/4)x^4. \quad (2.9)$$

Thus for high temperatures $\rho_{ph}(T) \propto T$.

- If $T \ll \Theta_D$, i.e. $z \gg 1$, then the ratio $\Theta_D/T \rightarrow \infty$, which with $J_n(\Theta_D/T) \approx J_n(\infty) = n! \zeta(n)$ leads to:

$$\rho_{ph} \approx (124.4 c_2 / \Theta_D) (T / \Theta_D)^5. \quad (2.10)$$

Here, ζ represents Riemann's Zeta-function and $\zeta(5) = 1.037$.

Summing up, one can state that high temperatures will cause a linear behaviour of $\rho_{ph}(T)$, as it is well known for simple non-magnetic metals. The magnetic part in (2.7), ρ_{mag} , which represents scattering processes of charge carriers on localised magnetic moments $\vec{m}_i = \gamma \vec{s}_i$, can be described in terms of a Heisenberg Hamiltonian (s-d model)

$$H = -\mathfrak{J} \vec{S} \cdot \vec{s}. \quad (2.11)$$

\mathfrak{J} is the Heisenberg coupling constant, which is positive in the case of ferromagnetic coupling and negative for antiferromagnets. For the paramagnetic temperature range, i.e. if $T > T_{ord}$, which is the temperature of magnetic ordering, ρ_{mag} can be written as:

$$\rho_{mag}(T) = \frac{3\pi N m^*}{2\hbar e^2 E_F} |\mathfrak{J}|^2 (g-1)^2 \cdot j(j+1). \quad (2.12)$$

As one can easily notice, equation (2.12) does not show any temperature dependence. The determining part is the deGennes-factor $(g-1)^2 \cdot j(j+1)$, which contains the Landé-factor g and the total angular momentum j of the magnetic ion. For temperatures in the magnetically ordered region $\rho_{mag} = \rho_{mag}(T)$. One could inter alia take a spin wave dispersion into account, which results in a squared temperature dependence $\rho_{mag} \propto T^2$ in case of a ferromagnetic state.

⁵General definition of Debye's functions:

$$J_n(x) = \int_0^x \left(\frac{t^n}{(e^t - 1)(1 - e^{-t})} \right) dt$$

2.1.2. Heat capacity

⁶ The heat capacity c of a body describes the amount of heat ΔQ which it can absorb or emit during a temperature change ΔT . It can be defined either at constant pressure or volume and is normalized to 1 mol.

$$c_V \equiv \left(\frac{\partial' Q}{\partial T} \right)_V = \left(\frac{\partial U}{\partial T} \right)_V, \quad (2.13)$$

$$c_p \equiv \left(\frac{\partial' Q}{\partial T} \right)_p = \left(\frac{\partial(U + pV)}{\partial T} \right)_p = \left(\frac{\partial H}{\partial T} \right)_p. \quad (2.14)$$

In a solid, the difference is small $c_p - c_V = (1/\kappa)TV\alpha^2$ and $c_p > c_V$. The first relation is called Grüneisen law; κ is the compressibility and α the thermal expansion. As it is easier to realise, c_p is measured in this thesis. In Eqn. (2.13) and (2.14) U is the *intrinsic energy* of the body and H the *enthalpy*, two thermodynamical potentials, which are connected by Legendre transformations. Another important quantity connected to heat capacity is the *entropy* S . It is defined by

$$dS \equiv \frac{d'Q_{rev}}{T}. \quad (2.15)$$

The *rev* subscript means that only reversible processes will fulfil this relation. One can furthermore relate $c_{V,p} = T(\partial S/\partial T)_{V,p}$ with V and p respectively. In an analogous manner to the electrical resistivity, the heat capacity c in a solid can also be written as a sum of contributions. Without proof:

$$c = c_{ph} + c_{el} + c_{mag} + c_{nuc}. \quad (2.16)$$

As a matter of fact, c_{ph} is the phononic contribution, c_{el} the contribution of the conduction electrons, c_{mag} the magnetic contribution and c_{nuc} a nuclear contribution which is only relevant at very low temperatures and will thus be neglected in this thesis.

The lattice part of the heat capacity is most commonly described by two easy models, which were created by Debye and Einstein and later named after them. Einstein, who made the first attempt, described the lattice as N uncoupled harmonic oscillators with the same frequency ω_E , the Einstein frequency. The result for c_V , which can be obtained by differentiating U with respect to T , is

$$c_V = 3k_B N \frac{\left(\frac{\hbar\omega_E}{k_B T} \right)^2 \exp\left(\frac{\hbar\omega_E}{k_B T} \right)}{\left(\exp\left(\frac{\hbar\omega_E}{k_B T} \right) - 1 \right)^2}. \quad (2.17)$$

For high temperatures, Einstein's description matches well with experimental data, especially as c_V approaches $c_V = 3R$, which is the long known Dulong-Petit law (with R the gas constant). However, it cannot explain the T^3 behaviour of c_V , which was observed in many cases at low temperatures.

Debye made the improvement that instead of one frequency, he assumed that the N particles are coupled harmonic oscillators. Lattice vibrations can be described as sound waves with the dispersion relation $\omega = v \cdot k$. The surfaces of constant frequencies are spheres in the \vec{k} -space. This induces that the number of modes with frequencies smaller than a certain value ω_D , which is called Debye-frequency is proportional to the volume of a sphere. The number of modes thus is the volume in k -space multiplied by the volume per k -value $(2\pi/L)^3$.

$$N = \left(\frac{L}{2\pi} \right)^3 \left(\frac{4\pi k^3}{3} \right) \quad (2.18)$$

⁶ [2, 3]

Now, the density of states can be calculated as the differentiation of N with respect to the frequency ω :

$$g(\omega) = \frac{dN}{d\omega} = \frac{dN}{dk} \frac{dk}{d\omega} = \left(\frac{L}{2\pi}\right)^3 4\pi k^2 \frac{dk}{d\omega} = \left(\frac{Vk^2}{2\pi^2}\right) \frac{dk}{d\omega} = \frac{V\omega^2}{2\pi^2 v^3} \quad (2.19)$$

using $dk/d\omega = 1/v$ from the dispersion relation and $V = L^3$. With $g(\omega) = 0 \forall \omega > \omega_D$, one can calculate the intrinsic energy U

$$U = 3 \int_0^{\omega_D} d\omega \frac{V\omega^2}{2\pi^2 v^3} \left(\frac{\hbar\omega}{\exp\left(\frac{\hbar\omega}{k_B T}\right) - 1} \right) \quad (2.20)$$

using Planck's formula for a harmonic oscillator. The abbreviations $x_D = \hbar\omega_D/k_B T$, and $\hbar\omega_D/k_B = \Theta_D$ help to write formula (2.20) in a more clearly arranged way:

$$U = 9Nk_B T \left(\frac{T}{\Theta_D}\right)^3 \int_0^{x_D} dx \frac{x^3}{\exp(x) - 1}. \quad (2.21)$$

This equation can be solved for very large and very small values of T , when making a series expansion.

- For $T \gg \Theta_D$, one obtains

$$U = 3Nk_B T \Rightarrow c_V = \frac{dU}{dT} = 3Nk_B = 3R \quad (2.22)$$

the Dulong-Petit law, like it was also derived by Einstein.

- For $T \ll \Theta_D$ it follows

$$U = \frac{3}{5}\pi^4 Nk_B \frac{T^4}{\Theta_D^3} \Rightarrow c_V = \frac{12}{5}\pi^4 Nk_B \left(\frac{T}{\Theta_D}\right)^3 \quad (2.23)$$

which is the T^3 dependency of c_V observed in experiments.

Nevertheless, Debye's model does not take optical phonons branches into account⁷, which occur at higher temperatures if the unit cell contains more than one atom. Combinations of Einstein's and Debye's model have been published.

The electronic part of the heat capacity c_{el} , however, can be derived from the Sommerfeld model of free electrons. Only electrons near the Fermi-surface contribute to c_{el} . One obtains a linear temperature dependence. The slope of the straight line is called Sommerfeld's coefficient γ .

$$c_{el} = \frac{2\pi^2}{3} N(E_F) k_B^2 T = \gamma \cdot T \quad (2.24)$$

c_{el} plays an important role at low temperatures while at high temperatures the phononic part is dominant.

Furthermore, there is a magnetic contribution to heat capacity, which results from the capability of magnetic moments to flip. By absorption of heat, the magnetic moment is raised from the ground state to an excited state. If spins in the solid are dynamically coupled, a spin wave (*magnon*) can be created using little energy. Those magnon excitations contribute to the heat capacity with a factor $c_V \propto T^{3/2}$ in ferromagnets. In antiferromagnets the relation is $c_V \propto T^3$. There are other contributing parts of the heat capacity, caused e.g. by crystal electric field (Schottky contribution⁹, which will not be discussed further.

⁷The dispersion relation is taken as linear for all phonon branches

2.1.3. Magnetic susceptibility

⁸ The most common definition of magnetic susceptibility⁹ χ is the magnetization in a material M divided by an external magnetic field H , hence $M = \chi \cdot H$. This type of quantity is called response function. Generally speaking, χ is a tensor of higher order, but for isotropic and homogenous bodies, the description as a scalar is sufficient. Magnetic materials can be classified in groups, according to the value of their susceptibility. The most important groups are

- diamagnets $\chi < 0$
- paramagnets $\chi > 0$
- ferromagnets $\chi \gg 0$
- antiferromagnets $\chi > 0$

Every solid shows, at least, diamagnetic behaviour. The temperature-independent effect results from the urge of the atoms to screen external magnetic fields. This results in a negative susceptibility, which was first described by Langevin (1905) and Pauli (1920) and is called Larmor-diamagnetism, and consists only of the contribution of valence electrons:

$$\chi = -\frac{\mu_0 N_A N_e e^2}{6m_e} \bar{r}^2. \quad (2.25)$$

μ_0 is the magnetic permeability of the vacuum, N_A represents Avogadro's constant, N_e the number of electrons which do Larmor precession to screen external fields. \bar{r}^2 is the mean squared distance between electrons and the atomic nucleus. The contribution is normalised to 1 mol.

The orbital contribution of conduction electrons results in diamagnetic behaviour as well, called Landau diamagnetism. The susceptibility is proportional to the density of states at the Fermi level. Most metals don't show diamagnetic behaviour because the diamagnetic contribution is too small. The best-known example for a diamagnet is every type of superconductor. It is also called *ideal diamagnet*, as it screens an external field completely from its inside.

The second item on the list, paramagnetism, is exhibited for instance in atoms and molecules with an odd number of electrons. As $\chi > 0$, magnetic ordering is attracted by an external field but does not retain, when the external field is removed. The quantum-mechanical description of paramagnetism considering the spin-orbit interaction yields the Brillouin function. Starting from the calculation of the mean magnetic moment in a certain field direction, one receives

$$F(j, y) = \frac{\langle \mu_j \rangle}{jg\mu_B} = \left(1 + \frac{1}{2j}\right) \coth \left[\left(1 + \frac{1}{2j}\right) y \right] - \left(\frac{1}{2j}\right) \coth \left(\frac{y}{2j}\right), \quad (2.26)$$

with the abbreviation $y = jg\mu_B B_0/k_B T$. Further enclosed quantities are the total angular momentum j , the Landé factor g and μ_B the Bohr magneton $\mu_B = e\hbar/2m_e$.

For high temperatures and low fields one can simplify equation (2.26) by a series expansion and will thus reach with the general definition of the susceptibility $\chi_m = (N_A \langle \mu_j \rangle)/B_0$, the result:

$$\chi_m = g^2 j(j+1) \frac{N\mu_B^2}{3k_B T} = \mu_{eff}^2 \frac{N\mu_B^2}{3k_B T}. \quad (2.27)$$

Equation (2.27) is called Curie's law and most commonly written by summarising the constants to $\chi_m = C_m/T$ with the Curie constant C_m . For many metals and intermetallic compounds one

⁸ [2, 3, 6]

⁹the word "magnetic" in "magnetic susceptibility" will be omitted henceforth

has to take into account a slightly different law, the Curie-Weiss law:

$$\chi = \frac{C_M}{T - \theta_p}. \quad (2.28)$$

The additional quantity here is the paramagnetic Curie temperature θ_p . By fitting measured curves of susceptibility in metals and intermetallic alloys, one can obtain the effective magnetic moment from the slope of the curve. The paramagnetic Curie temperature provides insights about the possibility of the system transforming into a ferromagnetic or antiferromagnetic groundstate at low temperatures.

Another important aspect of microscopic magnetism, which is especially relevant when dealing with heavy fermion systems is the temperature independent Pauli paramagnetism. It results from the spin of the conduction electrons and the behaviour of the Fermi-Dirac distribution function. In an external field the conduction band is split into two sub-bands corresponding to the two possible spin orientations. One band is lowered in energy by $E = g\mu_B B_0$ (spin parallel to external field), the other is raised by the aforementioned energy. This causes spins to flip into the direction of the magnetic field to ensure the same Fermi energy level for both sub-bands. The number of flipped, thus unpaired spins is proportional to the density of states at the Fermi energy, $N(E_F)$. The additional magnetization can be written as the difference of spin up and spin down electrons times their magnetic moment $M = \mu(N_+ - N_-)$. This difference yields Pauli's susceptibility

$$\chi_{Pauli} = \frac{\partial M}{\partial B_0} = \mu^2 N(E_F) \quad (2.29)$$

As Pauli's contribution is usually small for simple metals and temperature independent, it is relevant mainly at low temperatures. For strongly correlated systems, which possess a high density of states at the Fermi energy, this contribution is nevertheless important.

By considering the temperature dependence of the chemical potential $\mu_{chem}(T)$, which is $\mu_{chem}(T = 0) = E_F$ in the Fermi-Dirac distribution function, one has to improve the concept by introducing Stoner's susceptibility $\chi_{Stoner} = \chi_{Pauli}(1 + aT^2 + \dots)$. The factor a is derived from the form of the density of states at the Fermi level.

Moreover, it should be mentioned that the magnetic field applied also influences the motions of the electrons thus creating another diamagnetic part of the total susceptibility, which is named after Landau. It amounts $-1/3$ of the Pauli susceptibility.

2.2. Strongly correlated electron systems

As already mentioned in the introduction, the samples analysed in this thesis are part of the material class of strongly correlated electron systems.

These types of intermetallic compounds are also called frequently fermion materials. They contain rare earth elements like Ce, Yb, U, or to put it more precisely elements with 4f or 5f electrons and are characterised by extraordinary low temperature behaviour.

2.2.1. The Anderson model

¹⁰ In 1961, Anderson [10] made a successful attempt to describe and calculate properties of metals with dissolved magnetic impurities, e.g. Kondo systems, in the model named after him. Many dependencies on different state variables like temperature, pressure, field etc. can be calculated either exactly or by approximation. The core of the model is the Anderson Hamiltonian (2.30), which characterizes the behaviour of conduction electrons with a single magnetic impurity (e.g. 3d, 4f or 5f). The energy level of the local magnetic state is located within the continuum band of conduction electrons and near the Fermi energy.

$$H = \sum_{k,\sigma} \epsilon_k n_{k,\sigma} + \sum_{\sigma} E_0 n_{d,\sigma} + U n_{d\uparrow} n_{d\downarrow} + \sum_{k,\sigma} (V_{kd} c_{k\sigma}^+ c_{d\sigma} + V_{kd}^* c_{d\sigma}^+ c_{k\sigma}), \quad (2.30)$$

here, $c_{k\sigma}^+$ represents a creation operator for conduction electrons, which are assumed as plane waves with wave vector \vec{k} and spin σ . Additionally, $c_{k\sigma}$ is the Hermitian conjugate annihilation operator. Likewise, c_d^+ and c_d represent the above-mentioned operators for a localised d or f electron, while $n_{k,\sigma}$ and $n_{d,\sigma}$ are the corresponding number operators with generally $n = c^+c$. Orbital degeneracy is not taken into account in Eqn. (2.30).

The following itemization explains the different terms of the Anderson Hamiltonian:

- Firstly, one has to describe the kinetic energy of the conduction band, which is filled up to the Fermi energy. This is done in the first term by summing up the products of energy times number of electrons for each wave vector.
- The second term specifies the energy of the localised 3d or 4f state. Here, E_0 is the unperturbed binding energy of this state.
- The third term represents the Coloumb interaction part, which splits the two spin components of the magnetic impurity. One has to note that in case of the degenerate states, an extra exchange term has to be added. For $U = 0$, the position of the impurity level and the occupation probability would be the same for spin \uparrow and spin \downarrow , thus the impurity would be non-magnetic.
- The last term is probably the most interesting and describes the hybridisation of impurity states and delocalised conduction electron states. This hybridisation forms a central part of the description of Kondo systems, as it leads to a broadening of the local states. A so-called virtual bound state in Friedel's sense is formed, having a finite lifetime. The half-width of this state Δ is given by Fermi's golden rule: $\Delta = \pi \langle V \rangle^2 N(E_0)$, with $\langle V \rangle$ being the average of the hybridisation matrix element and $N(E_0)$ the conduction electron density for a particular spin at impurity energy E_0 (for instance 4f).

The quantities E_0 , U and Δ are responsible for the formation of various regimes within the Anderson model.

¹⁰ [3, 7-9]

- If $E_0 + U \gg E_F$, $E_0 \ll E_F$ with $|E_0 + U + E_F|$ and $|E_F - E_0|$ both larger than Δ , the local magnetic moment will exist and interact antiferromagnetically with the free electrons.
- E_0 or $E_0 + U$ approaches the Fermi energy. Thus $E_0 - E_F$ or $E_0 + U - E_F$ nears Δ and electron hopping between virtual states and conduction electrons occurs in a large amount. This regime is called intermediate valence regime.
- In between the two aforementioned regimes, with only a small admixture of localized and conduction electron states, one can transform the hybridisation matrix element V into an effective exchange interaction J , with the Kondo regime as result.

A sketch of the upper descriptions can be seen in Fig. 2.1.

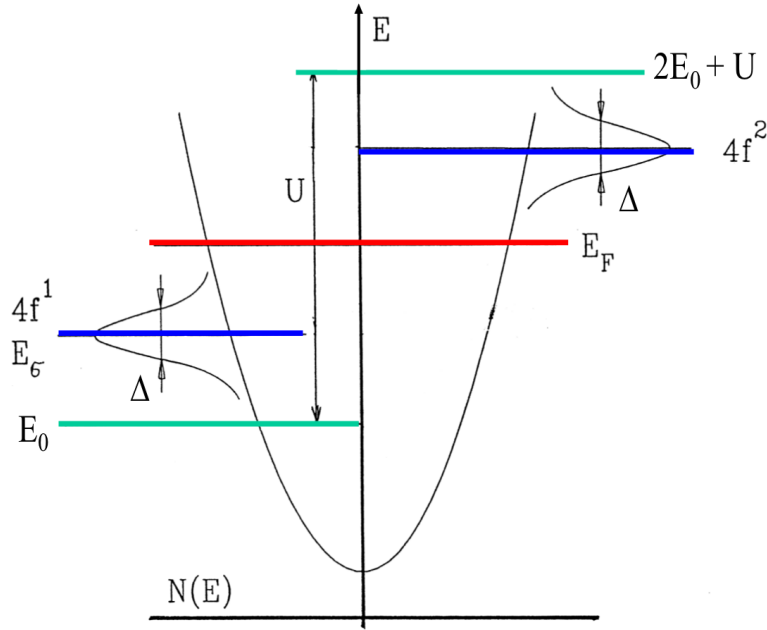


Figure 2.1.: Depiction of the band structure from the Anderson Hamiltonian

The solution of the Anderson model for the non-degenerate case can be done using a Hartree-Fock approximation. To sum up, one can say that the Anderson model and its Hamiltonian are a source for describing many physical phenomena, inter alia the physics of the Kondo problem. The Kondo impurity model 2.2.4 can be derived starting from a single impurity Anderson Hamiltonian in the limit of small mixing between the f and the conduction electrons by a Schrieffer-Wolff transformation. Furthermore, the Kondo lattice model 2.2.5 can be derived by adding $f - f$ hopping terms.

2.2.2. The Coqblin-Schrieffer model

¹¹ Being a variation of the Anderson model, the Coqblin-Schrieffer model's main application are $4f$ impurities of almost integer valency, e.g. CeAl_2 , CeCu_5 , etc. [11]. Even though it is a single-impurity model, experimental results are reproduced (mainly for $T \gg 0$) even for a high concentration of localized moments up to and including full occupation of one lattice site with a $4f$ element (Kondo lattice).

If the orbital angular momentum for such cases is not quenched due to a strong spin-orbit

¹¹ [3]

coupling, one has to take into account combined spin and orbital exchange scattering. In the case of cerium ($j = 5/2$, $l = 3$), only $l = 3$ partial-wave states of conduction electrons were considered to interact with the impurities. The Anderson Hamiltonian thus looks like $H = H_0 + H_1$ with

$$H_0 = \sum_{k,M} \epsilon_k c_{kM}^+ c_{kM} + E_0 \sum_{k,M} f_{kM}^+ f_{kM} + \frac{1}{2} U \sum_{MM'} n_M n_{M'} \quad (2.31)$$

$$H_1 = \sum_{k,M} (V_k c_{kM}^+ f_M + V_k^* f_M^+ c_{kM}). \quad (2.32)$$

The parameters included are the creation operator c_{kM}^+ for a conduction electron with the wave number k , $j = 5/2$ and z component M and the creation operator $f_{M'}^+$ for an impurity electron with $j = 5/2$ and z component M' . Applying a Schrieffer-Wolff transformation results in an effective exchange Hamiltonian with a coupling constant J . This Hamiltonian consists of two parts, one for the exchange interaction and another for the direct interaction of conduction electrons with the Ce moment. One can furthermore incorporate the influence of the crystalline electric field.

In 1972, Cornut and Coqblin [12] solved the model in order to study influences of the crystalline electric field on the electrical resistivity of Kondo systems, which contain cerium. The result was a partial lifting of the $2j + 1$ fold ground state degeneracy as a function of the symmetry of the lattice. Cornut and Coqblin calculated the relaxation time for a system with N level splitting and derived furthermore the temperature dependence of the magnetic contribution to electrical resistivity:

$$\rho_{mag}(T) \propto A - B * \ln \left(\frac{k_B T}{D_n} \right). \quad (2.33)$$

Here the first (constant) term describes a spin disorder resistivity, while the second term represents Kondo resistivity.

2.2.3. Crystalline electric field (CEF) effects

¹² In order to understand how spin disorder resistivity is modified, a short introduction about the crystal electric field shall be provided. In every crystal, a magnetic ion is distracted by a potential $V_c(\vec{r})$, which originates from the charges of other ions in the neighbourhood. The potential and the resulting field cause a partial lifting of the ground state degeneracy associated with the total angular momentum j . The detailed scheme of CEF splitting depends on j as well as on the symmetry of the field. For cerium ions, the CEF splitting is rather small compared to the spin orbit interaction (Fig. 2.2), nevertheless its influence cannot be neglected.

2.2.4. Kondo effect

¹³ In 1934 de Haas et al. noticed that a gold specimen contaminated with magnetic impurities showed a minimum in electrical resistivity at low temperatures. This anomalous behaviour was also observed in other alloys like Cu+0.057at.%Fe. As one can assume, the Fe atoms with their magnetic moments are statistically dissolved in the host metal. 30 years later J. Kondo could give a theoretical explanation by taking into account second-order scattering processes of conduction electrons by the magnetic impurities. More precisely, a first-order scattering process of the former type appears instantly either elastically or with a spin-flip and therefore a change in energy of the scattered particles (i.e. a change of m_S for the ion). Nevertheless, it doesn't produce any

¹² [3, 12, 13]

¹³ [3, 7-9, 13, 14]

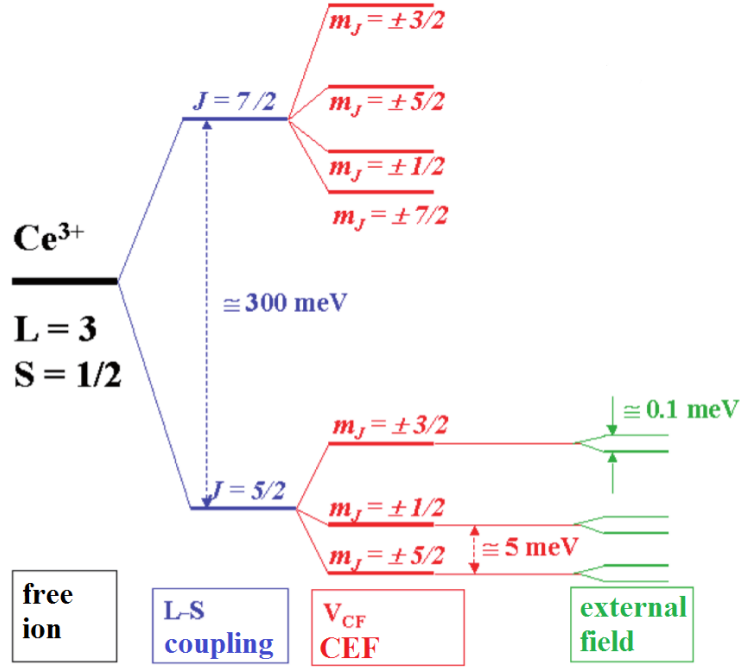


Figure 2.2.: Sketch of the energy splitting of Ce^{3+} in case of a hexagonal crystal structure. Only the two lowest multiplets are shown [2, p.30 of part 2]

temperature dependence of the electrical resistivity.

Second-order scattering, however, yields a so-called intermediate state in between a two-stage scattering process. The conduction electron as well as the magnetic impurity ion will pass this intermediate state before attaining the final state, which is the original state in case of the ion. This intermediate state is attended by e.g. a spin flip of the conduction electron as well as a compensating spin change of the magnetic impurity, which is reversed in the second stage of the scattering process (table 2.1). As Kondo could show, this type of scattering very well yields a temperature dependence of the scattering. In fact, there is also a second process in which a second electron takes part as shown in table 2.1, item II:

Conduction electrons	Magnetic Ion
I. $k \uparrow \rightarrow q \downarrow$	$m_S \rightarrow m_S + 1$
$q \downarrow \rightarrow k' \uparrow$	$m_S + 1 \rightarrow m_S$
II. $q \downarrow \rightarrow k' \uparrow$	$m_S \rightarrow m_S - 1$
$k \uparrow \rightarrow q \downarrow$	$m_S - 1 \rightarrow m_S$

Table 2.1.

Starting from the $s-d$ Heisenberg Hamiltonian $H = -J(\vec{r})\vec{\sigma} \cdot \vec{S}$, Kondo could derive an expression for the contribution to resistivity, caused by these scattering processes. Without presenting further details of the derivation, the temperature dependence of the electrical resistivity is

$$\rho_{imp} = \frac{3\pi m J^2 S(S+1)}{2e^2 \hbar E_F} \left[1 - 4JN(E_F) \ln \left(\frac{k_B T}{D} \right) \right] \quad (2.34)$$

with the cut-off parameter D and assumed negative exchange coupling ($J < 0$). This means a

negative logarithmic temperature dependence of ρ_{imp} , which is also proportional to the density of states at the Fermi energy $N(E_F)$, i.e. large for heavy fermion systems. Furthermore, Kondo could discover some important correlations. The depth of the resistivity minimum $\Delta\rho = \rho_{T=0} - \rho_{min}$ as well as its value ρ_{min} are proportional to the impurity concentration, while the temperature of the minimum isn't.

One can summarize the contributions to electrical resistivity:

$$\rho = aT^5 + c_{imp}R_0 - c_{imp}R_1 \ln(k_B T/D). \quad (2.35)$$

The first term in Eqn. (2.35) results from phononic processes, whilst the second is the impurity term. The third term accounts for the magnetic scattering processes including spin-flips. Kondo's calculations fit well with the observed behaviour for diluted magnetic systems, nevertheless the formula (2.34) yields a divergence of ρ_{imp} for $T \rightarrow 0$, which wasn't observed in experiments. For antiferromagnetic interaction, i.e. ($J < 0$), the electrical resistivity increases to a high level for small temperatures. This unphysical divergence is also present in Kondo-type calculations of the magnetic susceptibility and of the heat capacity.

Abrikosov tried to handle this problem by summing up the logarithmic terms to higher order. As these terms are summed up within a power series, they only appear in the denominator but thus yield a divergence of the denominator at a finite temperature for antiferromagnetic interaction. The temperature was called Kondo temperature T_K with $k_B T_K \approx D \exp(-1/2|J|\rho_0)$. Nonetheless, this behaviour is unphysical too, as there should be a phase transition at T_K , which wasn't observed. Moreover, the heat capacity in this model also diverges at T_K for antiferromagnetic coupling.

This failing of perturbation type calculations results from the fact that at the Kondo temperature, there is a crossover from weak to strong interactions. Many body interactions have to be taken into account, as the strong coupling of conduction electrons with the impurity magnetic moment screens the latter at a distance apart. The formation of a quasi-particle possessing a large effective mass and belonging to a singlet - non-magnetic - ground state yields the breakdown of the perturbation theory calculations.

Improvements of the model were made by Suhl, Nagaoka and Hamann by introducing an effective coupling constant, which yields a spin compensated singlet ground state at low temperatures ($S = 1/2, J < 0$). Thus, the divergence doesn't appear anymore and the resistivity curve approaches a finite value at low temperatures. Furthermore, it was stated by newer derivations that transport properties could also be described by simple power laws.

2.2.5. Concentrated Kondo systems

For low temperatures, single impurity models might not satisfyingly describe experimental results of Kondo systems, unless the concentration of diluted transition or rare earth metals is low. With increasing impurity concentration, wave functions of impurities start to overlap inducing interactions between them. Magnetic correlations may lead to short or even long range magnetic order accompanied by the blocking of spin-flip processes like described in section 2.2.4. Nevertheless in the case of $4f$ impurities, even a large number of ions can be placed in the metallic host without destruction of the Kondo effect, as $4f$ wave functions have a very small spatial extent.

2.2.6. Kondo lattice

¹⁴If the magnetic ions in a material form a regular sub-lattice in the system, significant changes of the low temperature behaviour of transport properties occur. These systems with lattice

¹⁴ [3, 7, 8]

periodicity are called Kondo lattices and are phenomenologically described by the model of Doniach [15]. While at high temperatures ($T > T_K$), all physical properties are satisfyingly illustrated by single impurity models, low temperatures yield a significant deviation. This is explained by a decoupling of magnetic ions at elevated temperatures.

As it can be observed in Fig. 2.3, single impurity systems show the well-known logarithmic increase of ρ_{mag} for decreasing temperature, while lattice systems show a breakdown of $\rho_{mag}(T)$ below a specific temperature.

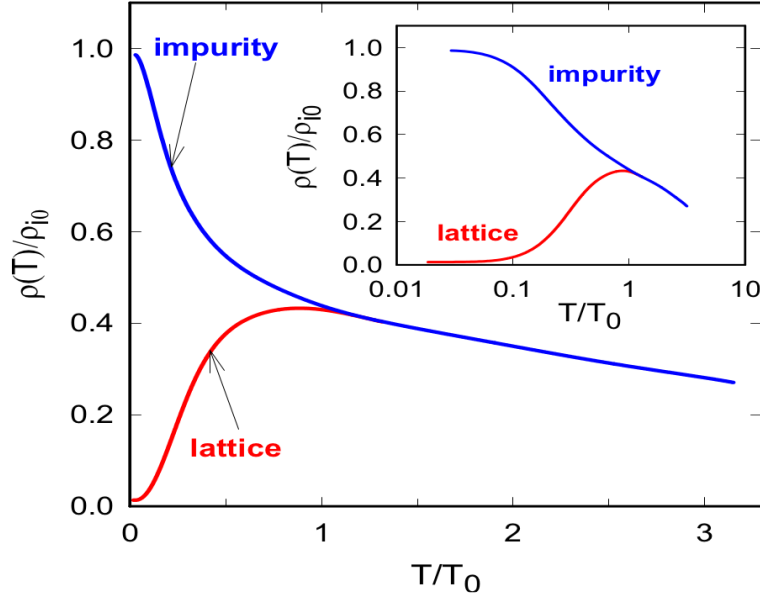


Figure 2.3.: Temperature dependence of the magnetic contribution to electrical resistivity of single impurity and lattice systems [3, p.133]

As a result, a maximum in ρ can be observed. The drop of the magnetic contribution to resistivity can be explained by intersite interactions between the magnetic moments on the various lattice sites. This leads to coherent scattering of conduction electrons, i.e. conduction electrons may pass the periodic array of magnetic ion scattering centers in form of a Bloch wave. This theory also fits perfectly with Bloch's theorem, stating that at zero temperature and excitation energy inelastic scattering is frozen out. This coherent ground state is most likely caused by antiferromagnetic correlations. With decreasing temperature, periodicity of scattering centres is improved thus conditions for Bloch waves are better fulfilled and resistivity sinks even lower.

In the low temperature region, the demagnetised system exhibits a Fermi liquid ground state. $\rho(T)$ is characterised by a simple power law, evidencing electron-electron scattering:

$$\rho = \rho_0 + AT^2. \quad (2.36)$$

The coefficient A is proportional to the electronic density of states at the Fermi level and of large magnitude, i.e. characteristic for heavy fermion systems. For single impurity Kondo effect, single fermionic levels in the conduction sea are formed thus creating a resonance in the density of states. This is called Kondo or Abrikosov-Suhl resonance. In a lattice, however, a whole band structure is constituted, a heavy electron band of width T_K .

2.2.7. RKKY-Interactions

¹⁵ In a Kondo lattice, interactions between the different lattice sites occur and are, at least for alloys containing 4*f* elements like cerium, primarily of RKKY type. In 1954 Rudermann and Kittel [16] first proposed the idea that interactions between magnetic moments are promoted by the conduction electrons. Kasuya and Yoshida improved this idea. This was an important approach how to explain long range magnetic order in rare earth element compounds, where *f* wave functions are strongly localised. Magnetic ions disturb the wave function of the conduction electron and polarise their spins \vec{s} , when they are near. The latter is caused by phase shifts of the Bloch waves of the conduction electrons and has long-range oscillations as a result. The magnetic moments of the neighbouring ions in turn, are influenced by this polarisation and align their moments, thus sensing the interaction of the first ion.

Second order perturbation theory yields for the RKKY interaction:

$$\frac{9\pi^2 Z^2 J(g-1)^2}{4E_F v_0^2} F(x) j_1 j_2 \quad (2.37)$$

with the oscillating Rudermann-Kittel function $F(x) \equiv F(2k_F R_{12}) = x^{-4}(x \cos x - \sin x)$. This function, which is also shown in Fig. 2.4, can assume both positive and negative values, which corresponds to ferro- and antiferromagnetic nature of the interaction.

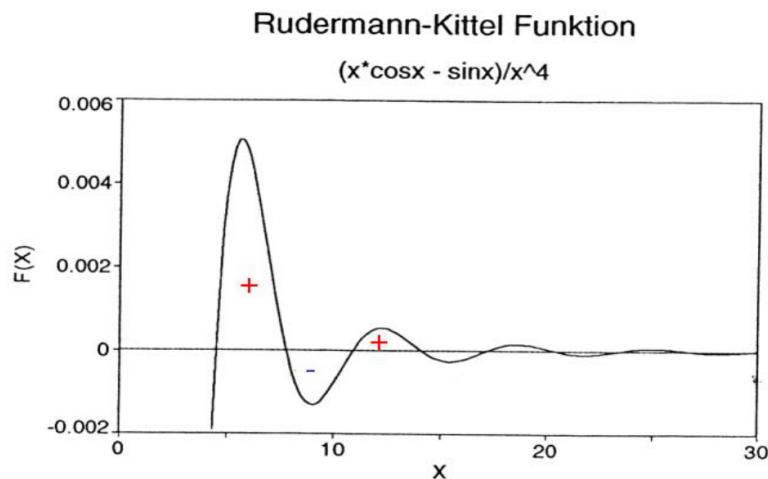


Figure 2.4.: Rudermann-Kittel function with the distance between two magnetic ions x [3, p. 136]

The strength of the RKKY interaction is quadratic in $JN(E_F)$ like $T_{RKKY} \propto |JN(E_F)|^2$ while the Kondo interaction depends exponentially on the aforementioned variable: $T_K \propto \exp(-1/|JN(E_F)|)$. This behaviour is illustrated in Doniach's phase diagram 2.5. For small values on the abscissa, Doniach's phase diagram shows that T_{RKKY} is much larger than T_K , thus while decreasing temperature, the system changes directly from the paramagnetic state into a magnetic phase with localised moments. For high values of $|JN(E_F)|$, however, T_K dominates thus localised moments are completely screened by conduction electrons. Consequently, the system remains non-magnetic forming a heavy Fermi liquid at low temperatures. Doniach could also derive the existence of a critical value $|JN(E_F)|_c$ separating the two regions of spin compensated state and state with magnetic order. Coleman later showed that the value of $|JN(E_F)|_c$ is

¹⁵ [3, 8, 15–18]

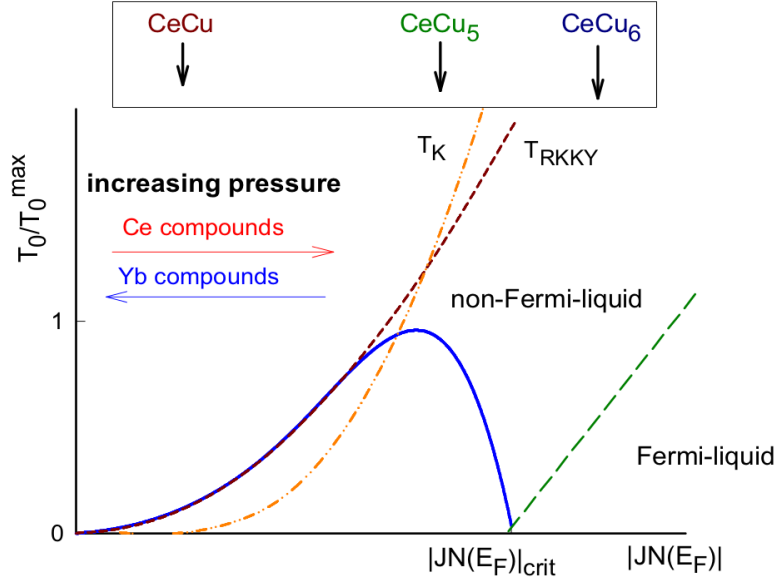


Figure 2.5.: Doniach's phase diagram [3, p.137]

dependent on the degeneracy $N = 2j + 1$ of the ground state. If N is large, the Kondo state is dominant and spin-spin correlations are nearly suppressed. At intermediate values of $|JN(E_F)|$, $T_K \approx T_{RKKY}$ and therefore the Kondo effect and long range magnetic order can occur at the same time. The appearance of Doniach's phase diagram can be modified by some external parameters like magnetic fields or pressure. As seen in Fig. 2.5, for cerium compounds the graphs are shifted towards higher values of $|JN(E_F)|$, when pressure is increased.

2.2.8. Fermi- and non-Fermi liquid behaviour

¹⁶ Developed in 1956 by Landau, the Fermi liquid theory soon became an important fundament for describing normal fermion systems inter alia many f -electron systems. Kondo lattice compounds at low temperatures, i.e. in the spin compensated state, are also suitable to be characterised by the Fermi liquid model.

The so-called one-to-one correspondence between the eigenstates of a Fermi electron gas and the Fermi liquid is the core of the theory. Electrons (as quasiparticles) are described like in a Fermi gas but interactions are taken into account by simply renormalising their effective mass m^* , which becomes much larger. By introducing a quasiparticle distribution function $n(p, \sigma)$ for quasiparticles with momentum p and spin σ and assuming only a small difference of this function from the value of a perfectly free Fermi gas at $T \rightarrow 0$, one obtains

$$n_0(p, \sigma) = 1 \text{ for } p < p_F \quad (2.38)$$

$$= 0 \text{ for } p > p_F. \quad (2.39)$$

Here, n_0 is the occupation of the ground state and p_F the Fermi momentum. The distribution (occupation) function of a Fermi liquid possesses a discontinuity at the Fermi energy, as well as the one of the Fermi gas. The difference is the breadth of the discontinuity. While in a Fermi gas the distribution function is of Heaviside form, jumping from zero to the maximum, in a Fermi liquid it is smeared. The jump height depends on the quasiparticle weight z , which is proportional to

¹⁶ [3, 8, 19, 20]

the reciprocal effective mass, i.e. the stronger the interactions, the smaller the jump.

As already mentioned before, one-to-one mapping of non-interacting to interacting electron states is assumed close to the Fermi energy in the Fermi liquid model. The second important thing leading to a description of electron states as quasiparticles is the adiabatic tuning of the interaction. The effective mass m^* is used at low temperatures to describe the thermodynamic properties of the system. While in *normal* metals, m^* is located in the dimension of the free electron mass m_e , values a thousand times larger are observed in heavy fermion systems.

In order to obtain the behaviour of important physical transport properties, one has to calculate the density of states at the Fermi energy, which is

$$N(0) = \frac{m^* k_F}{\pi^2 \hbar^2}, \quad (2.40)$$

where the effective mass of the quasiparticles m^* is related to the bare mass m_e by a so-called symmetric Landau parameter

$$\frac{m^*}{m_e} = 1 + \frac{F_1^s}{3}. \quad (2.41)$$

With this knowledge, the temperature independent Pauli susceptibility can be derived:

$$\chi = \frac{\mu_0 \mu_B m^* k_F}{\pi^2 \hbar^2} \frac{1}{1 + F_0^a} \quad (2.42)$$

F_0^a is an antisymmetric Landau parameter.

Specific heat capacity c_V within the Fermi liquid model looks like

$$\frac{c_V}{T} \equiv \gamma = \frac{m^* k_F k_B^2}{3 \hbar^2} \quad (2.43)$$

This equation, compared to Eqn. (2.24) is enhanced only by the ratio m^*/m_e . One can directly obtain information about the effective mass from γ . One can also define the Wilson ratio R_W , a connection between heat capacity and Pauli susceptibility

$$R_W \equiv \frac{\pi^2 k_B^2 \chi}{3 \mu_0 \mu_B^2 \gamma} = \frac{1}{1 + F_0^a} \quad (2.44)$$

For non-interacting systems, R_W becomes 1.

Like it is mentioned in section 2.2.6, the electrical resistivity behaves like $\rho = \rho_0 + AT^2$ with A being proportional to $N(E_F)^2$. Furthermore, the empirical Kadowaki-Woods relation between A and γ is given by $A/\gamma^2 \approx 10 \mu\Omega\text{cmK}^4\text{mol}^2\text{J}^{-2}$.

Strongly correlated electron systems which don't exhibit the simple power laws in temperature dependence at specifically low temperatures are called *non-Fermi liquid*. This behaviour results in general from the exceptional features of the momentum distribution function close to E_F . Macroscopic physical properties show a temperature dependence strongly deviating from the one of a Fermi liquid, e.g. a diverging c_V/T for low temperatures. The most important theoretical scenarios to describe non-Fermi liquid behaviour in f-electron systems are:

- the assumption of proximity to a quantum critical point. A continuous phase transition occurs at $T = 0$ either spontaneously or by tuning the transition by an external state variable.
- multichannel Kondo models
- models based on the disorder of materials

Quantum critical point (QCP)

¹⁷ Classical critical points are characterised by a phase transition at a certain temperature, e.g. a ferro- or antiferromagnetic transition. If this point is continuously tuned to zero temperature by some external parameter like pressure, magnetic field or chemical substitution, a quantum critical point is reached. In Fig. 2.6, this can be seen with magnetic field as external variable. At the QCP, the low-temperature thermodynamics is determined by collective modes corresponding to fluctuations of the order parameter, rather than by single-fermion excitations as in a Fermi liquid. That's why non-Fermi liquid properties are observed.

Several theoretical explanations for non-Fermi liquid behaviour near a QCP have been suggested: Firstly, scattering of heavy quasiparticles by strong spin fluctuations near the spin-density wave instability was suspected. Another imaginable scenario is the breakdown of the Kondo effect due to strong RKKY interactions, while the third possibility is the formation of a so-called Griffith phase near the QCP.

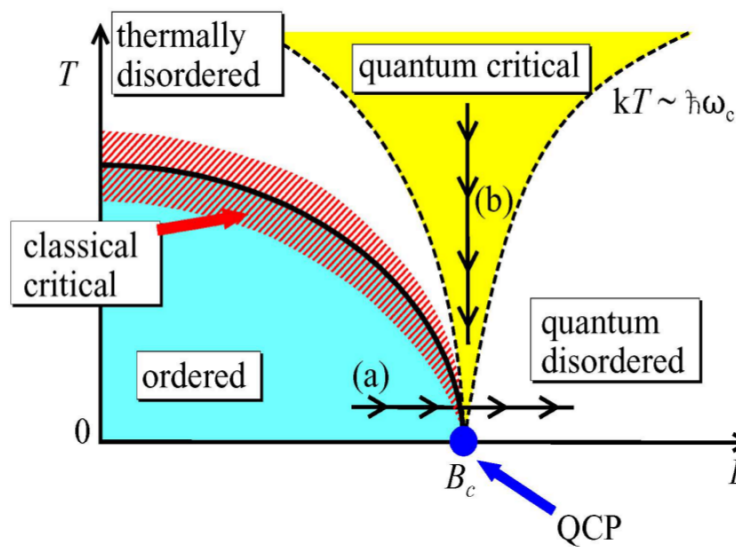


Figure 2.6.: Generic phase diagram and non-Fermi liquid region close to a magnetic instability for heavy fermion systems [3, p. 147]

¹⁷ [3]

3. Experimental realisation

3.1. Sample preparation

99.9 mass % pure component metals cerium, palladium, silicon, germanium and nickel were weighted according to stoichiometric proportions to get a total sample mass of approximately 2.5 g with an accuracy of 10^{-5} g. For easy-oxidizing cerium, the preparation of the accurate initial mass was done in a glovebox under argon atmosphere. For the synthesizing process, the author used the institute's high frequency induction melting generator¹. The pure metals were placed properly in a water-cooled copper pipe with crucible-like slots. To prevent oxidations during the melting process, there has to be a controlled atmosphere around. This objective was achieved by evacuation of the quartz cylinder which surrounds the pipe and subsequent flushing with argon gas. The latter process was repeated for at least 3 times. Furthermore, the buttons in the slots are turned over and remelted again to make sure their homogeneity. For further reasons of homogenisation, the standard procedure is to wrap the alloys into tantalum foil and seal them in an evacuated quartz tube, which is annealed at 800 °C for at least one week (*tempering process*). This temperature was applied for instance by Lipatov et al. in [21].

The mass loss during the induction melting process was in each case less than 0.5 %, thus making the sample quality rather high. The change of mass during the tempering process was negligible. In order to obtain the exact dimensions, needed for further experiments, a diamond buzz saw was used to cut the samples.

3.2. X-ray powder diffraction analyses

In order to determine the structure quality of the alloys i.e. comparing it with theoretical structures, x-ray powder diffraction (XRD) at room temperature was applied. For this purpose a Siemens D5000 diffractometer² was used. The sample is ground into a fine powder and spread onto a greased glass plate which then is placed like in Fig. 3.1. Thus a diffraction pattern is produced according to Bragg's law.

CuK α radiation was used guided by the program *Diffpac-At V 3.0*. The angle step size was 0.02° for a total angle 2θ between 10° and 100° and a step time between 9 and 15 seconds. The collected data were evaluated using the Windows programm *PowderCell V 2.4*.³ Starting from results published in [1], more precisely the lattice parameters of Ce₃Pd₄Si₄, the generated theoretical diffraction pattern was adapted to the measured data by means of Rietveld refinement, thus collecting information about the change of the lattice parameters and their dimensions. Moreover, the analysis of diffraction data can be used to determine if there are impurity phases in our alloy. For the results of this thesis only good quality samples, i.e. containing a vanishingly

¹The system generates a high frequency alternating current (by means of LC resonant oscillating circuit) passing through a coil with low resistance. The strong and rapidly changing magnetic field induces turbulent current flows in our original metals thus heating them over the melting point according to Joule's first law.

²For single- of polycrystals consisting of a goniometer to realize $\theta - 2\theta$ scan (Bragg-Brentano geometry [22])

³W. Kraus & G. Nolze, *Federal Institute for Materials Research and Testing, Berlin, 2000*

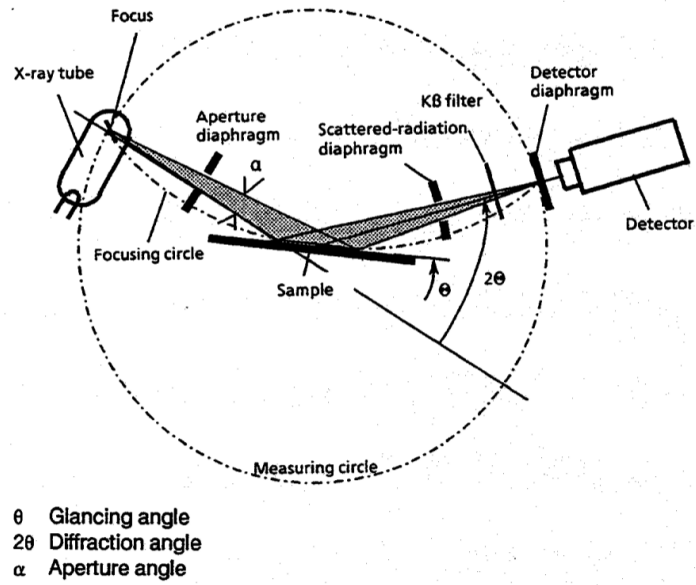


Fig. 2-1 Diffractometer beam path in $\theta/2\theta$ mode

Figure 3.1.: Depiction of x-ray diffractometry in Bragg-Brentano geometry as shown in the Siemens D5000 manual, page 2-1 [23]

small ratio of impurity phases, have been used.⁴ Diffraction results are presented for each sample in chapter 4.

⁴The author has also tried to prepare more samples of the $\text{Ce}_3\text{Pd}_4\text{Si}_x\text{Ge}_{4-x}$ series but failed at higher Ge concentrations, as there were forming too many impurity phases inside, when using the aforementioned preparation process. Also, a second heat treatment at 900°C for 1 week, suggested by the supervisor, didn't improve the situation. Unfortunately there are still no phase diagram data available for these special alloys, thus making it difficult to determine an accurate temperature. [24] and [21] can give an input for this problem.

3.3. Resistivity measurements

In order to obtain measurement results of high quality for this transport phenomenon, one has to create samples of a well-measurable geometry. As mentioned before, a diamond buzz saw was used to cut the alloys. In several steps, samples were glued onto a copper pad, sawed trough, detached with acetone until a cuboid was obtained. Thus, formula (3.1) can be used to calculate electrical resistivity from the measured resistance, or rather voltage divided by current.

$$\rho = \frac{A}{l} \cdot \frac{U}{I} \text{ with } \frac{U}{I} = R \text{ (Ohm's law)} \quad (3.1)$$

A is the area $A = w \cdot h$ with the width w and the height h ; l is the length, ρ is the resistivity and R the total resistance. Length, width and height of the cuboid were determined with the help of a *Zeiss Stemi 2000-C* microscope having an *AxioCam ERc 5S* installed and the suitable computer program *AxioVision40 V 4.8.2.0*. The length should be much longer than the other dimensions to secure that there is enough interspace between the contacts. The more cuboid our sample is, the better, i.e. surfaces should be as parallel as possible. Having no major cracks in the samples ensures a homogenous current flow and good measurement results. Crackless samples are more likely to withstand the mechanical stress when being cooled and heated up again.

Four-terminal sensing was used for carrying out the resistivity measurements with the main advantage⁵ that the resistance of feeding wires does not influence our quantitative results. For this purpose, 4 gold-wires with a diameter of $50 \mu\text{m}$ are spot-welded⁶ onto the surface alongside a line. 2 of the contacts have to be near to each other, respectively. The interspace between those two pairs is proportional to the measurement accuracy. The outer contacts are used for leading a current through the sample, while at the inner ones the potential drop is measured as voltage according to Ohm's law. The current passing through the voltmeter produces a negligible error. In order to ensure the contact sticking on the sample, Epotek H20E silver two-component glue was applied onto the welding contacts. A theoretical scheme of the four-terminal connections as well as a foto of a connected sample can be seen in figure 3.2.

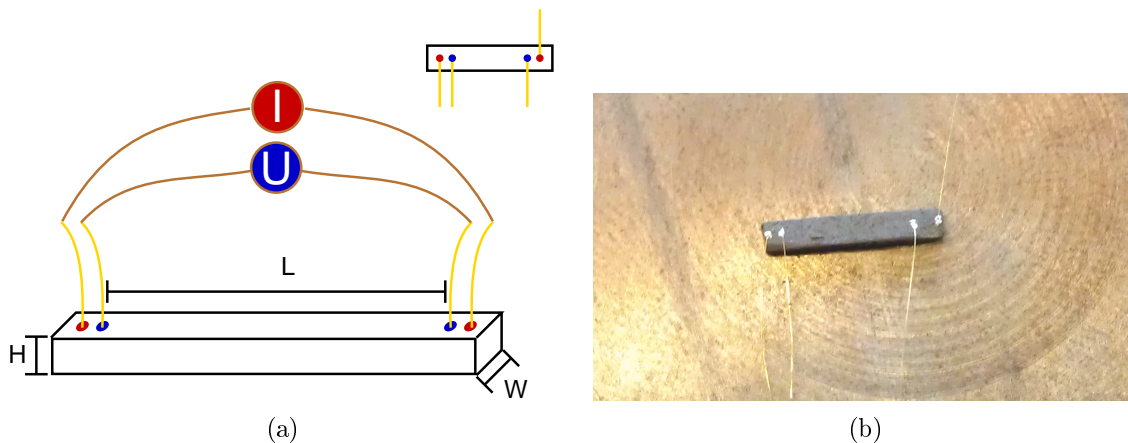


Figure 3.2.: Theoretical description of four-terminal sensing method 3.2a, presented on a sample 3.2b. [25, p. 31]

⁵compared to two-terminal sensing

⁶Wire and sample are molten together by a high current flow for a certain time. Time and current have to be adapted for each sample in order to keep them safe

The sample carriers for many transport phenomena measurements are called pucks. The sample is placed in the middle of the puck platform as shown in Fig. 3.3a and 3.3b. As the small square in the middle of the puck is conducting, an isolator has to be put between it and the sample. We used cigarette paper, which was glued onto the square using an isolating glue: GE varnish⁷. Now the sample was fixed onto the paper with the contacts to the top and the latter are soldered onto the puck as also shown in Fig. 3.3. On the bottom side of the puck, there are 4 contact pins, which will then be connected to our sample holder in the resistivity measurements devices. In general the pucks are rotationally invariant, thus can be placed in either way.

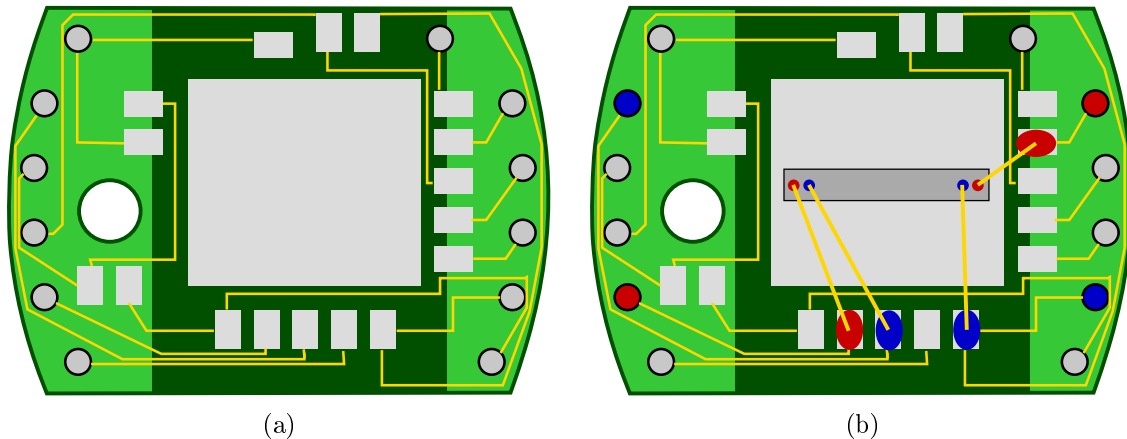


Figure 3.3.: Depiction of an empty 3.3a and an occupied puck 3.3b. In accord with Fig. 3.2, the red marked contacts are used for current input whereas at the blue ones, voltage is measured. [25, p.33]

3.3.1. ⁴He bath cryostat

For resistivity measurements from room temperature down to the condensing temperature of ⁴He, a Precision Cryogenic Systems, Inc. cryostat [27] was used. Students of the Vienna University of Technology [28] built a rod for inserting into this cryostat, with a sample carrier at the bottom. The sample carrier is similar to the one presented in Fig. 3.4 in [25, p. 37] except for the number of samples, which can be measured simultaneously (2). The cryostat consists of an outer and an inner chamber, which are separated by an ultra high vacuum (UHV) for reasons of thermic isolation.

First the rod is placed in the cryostat and fixed, then the cables are connected. The cryostat is cooled down by transferring liquid helium⁸ from a dewar using a specially designed transfer tube (which consists of an inner and an outer pipe and UHV in the interspace). This helium is always regained again by a special recovery system except for small losses and then re-liquified. Warming up is done by natural heat exchange with the environment.

A LakeShore model 370 AC resistance bridge is used for collecting resistivity data, as the accuracy is very high compared to the excitations. Currents down to 3.16 pA with almost no DC component can be produced by the current source to minimise noises and avoid resistor heating. As aforementioned, four-terminal sensing is used. Excitation current with a frequency of 13.7 Hz is fed to the outer leads, while voltage is measured at the inner leads (high input

⁷General Electric 7031 varnish, a polyvinyl phenolic varnish [26]

⁸or rather cold helium vapour

impedance). Other advantages of the AC method are greater sensitivity by the use of AC filters, the applicability of a preamplifier⁹ and the natural averaging of remaining thermal EMF or offset. Resistances from 2 m Ω to 2 M Ω can be measured. More accurate information can be found in the respective manual.

The LakeShore bridge is connected to a computer, which has the controlling program installed. Before starting, one has to enter the samples' dimensions and other properties. Resistance is measured with a certain rate depending on the temperature change. Usually, the measuring interval is smaller for low temperatures, but this can be changed in the computer program's settings. Starting with the cooling process, resistance is measured but for reasons of accuracy, only the data, collected at rising temperatures, will be evaluated¹⁰. The data points are written into a *.BRG* text file in two columns (temperature and calculated resistivity for each sample, respectively). One has to note, that the device is only able, to measure one sample at a certain instant of time, thus temperature points for the two samples are different, when performing a drift.

3.3.2. ³He refrigerator system

Resistivity measurements ranging from 300 mK to room temperature and in magnetic fields up to 12.5 T can be done in the Institute's high field laboratory. A top-loading bath cryostat made of fiber aluminium and constructed by *CRYOGENIC* is connected to a ³He storage dump, which can hold up to 25 l of gas. On the one hand, ³He gas serves as a heat exchanger as it surrounds samples and inset, on the other hand it takes an important part in the cooling procedure, thus losses should be strictly avoided¹¹. The cryostat is constructed in layers. Starting on the outside, there is a high purity aluminium radiation shield and a superinsulation blanket of alternative layers of reflective aluminised mylar and nylon netting to reduce the thermal radiation from the surroundings [29]. A cask filled with approximately 30 l of liquid N₂ serves as second thermal shielding in order to keep the evaporation rate of liquid ⁴He low. Moreover, the interspace is evacuated (UHV). Below the LN₂ tank, the ⁴He tank is placed, as shown in Fig. 3.4 Liquid helium up to 40 l is filled into the tank; it takes an important part in the cooling process¹².

As seen in the two figures, the ⁴He chamber contains a superconducting coil system for resistivity measurements in magnetic fields. The inner coil is made from multifilamentary Nb₃Sn wound on a stainless steel former while the outer one is made from NbTi on an aluminium former. Fields up to 12.5 T can be reached in persistent mode. This means, that the heater is heated over the superconducting transition temperature, then fed with an amount of current¹³ from an external power source. After a stabilizing process, the heater is switched off, thus the superconducting coil is in its persistent mode. One can turn off the supply current, i.e. the above heater, and as it drops, magnet current will circulate through a special superconducting switch (which is resistive at higher temperatures), thus keeping up the magnetic field. Even higher fields can be reached using the so-called λ -plate, but this option wasn't used.

In order to reach temperatures down to 300 mK, ³He has to be pumped¹⁴. For this purpose, a bin for collecting liquid ³He is needed at the bottom of the measurement chamber, the so-called 1K-pot. Furthermore, one needs a pump in order to reduce the vapour pressure. If the latter

⁹The device has a build-in preamplifier with a transformation factor 10

¹⁰The cooling rate is not as constant as the thawing rate

¹¹Moreover, one litre of ³He gas is priced at over 2000 US\$ on the world market

¹²One uses a transfer tube for filling like for the ⁴He cryostat. The level of liquid helium is measured using a superconducting wire, which is placed in the tank. From the resistance, one could infer the helium level, which is also monitored.

¹³corresponding to the desired field

¹⁴The ³He gas has the advantage of a much higher vapour pressure and also doesn't become superfluid above a few mK, as it is fermionic.

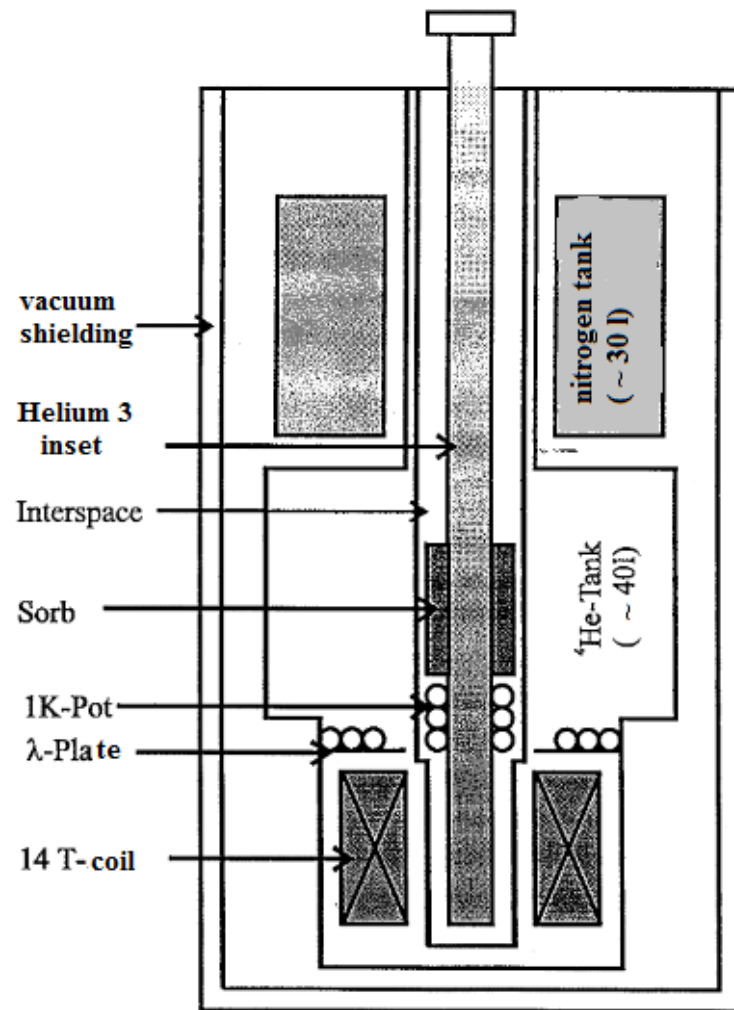


Figure 3.4.: Scheme of the ^3He cryostat [30, p. 16] (translated to English)

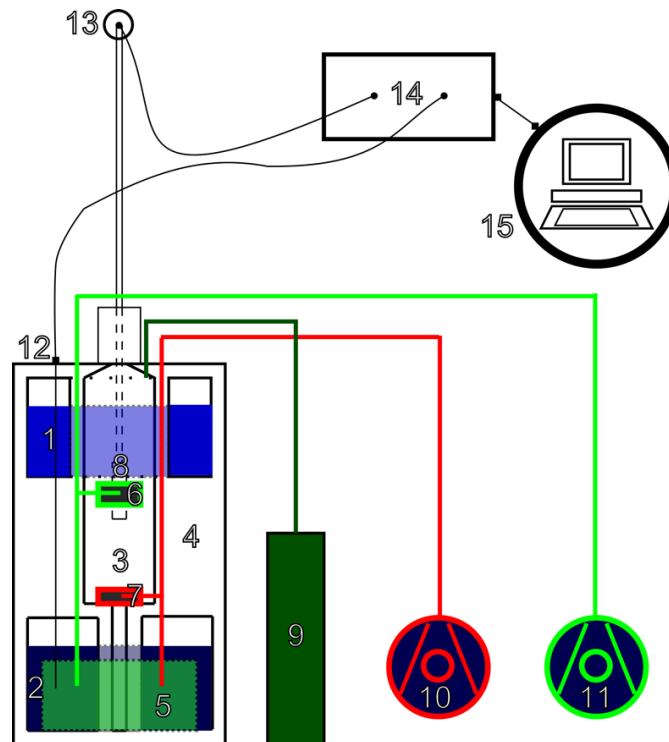


Figure 3.5.: Schematic plot of the ^3He measurement device: 1.) LN_2 reservoir 2.) ^4He reservoir 3.) Measurement chamber in ^3He atmosphere 4.) superinsulation 5.) Superconducting hybrid magnet 6.) Sorb 7.) 1-K Stage 8.) Sample rod and sample platform 9.) ^3He dump 10.) External 1-K pump 11.) External Sorb pump 12.) Power supply connection of the magnet 13.) Fischer connectors 14.) Power supply/temperature controllers/ Lakeshore Bridge 370 AC/ pressure gauge 15.) Computer [25, p. 36]

is reduced, the boiling temperature is also decreased by removing vaporization heat, thus much lower temperatures can be reached. In this cryostat, a sorption pump is used, which is placed in the measurement chamber like seen in Figs. 3.4 or 3.5. It consists of a bulk of charcoal with a large surface, which can be used to cool down a big amount of gas. Adsorption and absorption effects are used. Both the 1K-pot and the Sorb are built up of a ^3He and a ^4He site, which are thermally connected. Two independent capillaries starting at the ^4He reservoir pass through 1K-pot and sorb, respectively and are connected to two external pumps. The pumping rate i.e. pressure can be regulated using two needle valves and is also measured by two manometers and displayed. By pumping gas from the reservoir through the two aforementioned components, temperatures of about 2 K can be reached. ^3He , which has its boiling point at 3.19 K, condenses in the cooled 1K-pot, thus covering the samples. Now, one cools the sorb to gather ^3He atoms and thus removes heat from the samples. The 1-K pot as well as the sorb and the sample have a CERNOX temperature sensor installed. Temperatures are monitored by a *Lakeshore* temperature controller, which also has the option to heat samples and Sorb.

Similarly to the ^4He bath cryostat, the pucks are placed in a sample holder, which is located at the bottom of the inset rod. This sample holder (FRITZ [25, p. 34 ff.]) can be used to measure 4 samples at the same time. The same resistance bridge as with the ^4He device is used. A computer program saves the data points to a *.DRF* text file, if a temperature drift (constant field, varying temperature) is measured and to a *.RMP* text file if one measures a field ramp (constant temperature, varying field). A more detailed picture of the set-up can be seen in appendix A.

3.4. Magnetization measurements

Magnetization or magnetic susceptibility measurements were carried out in a superconducting quantum interference device (SQUID) by *CRYOGENIC*. This type of magnetisation measurement device has the highest known sensitivity, $10 \times 10^{-11} \text{ A m}^2$ to $10 \times 10^{-12} \text{ A m}^2$. Magnetic fields up to 6 T can be applied by a superconducting magnet. Measurements can be performed from 2 K to room temperature. It consists of a heat-isolating cryostat (vacuum mantle), which similar to the one described in the last section contains a LN_2 reservoir below the top and a L^4He reservoir at the measurement height. A so-called variable temperature inset holds the coil (2nd order gradiometer coil), the pick-up system and the SQUID [31]. Details shall be explained below. Samples have to be dimensioned in cylindrical shape in the ideal case and weight in the range of 10^1 mg . They are glued onto a light sample carrier, which consists of a cylindrical filament¹⁵ and a few plastic place holders. The filament is split on the top and connected via two loops of thin copper wire which form a universal joint so that the lower part, which contains the sample, may move flexibly. The upper part, however, contains the connector, like shown in Fig. 3.7.

For reasons of elaborateness, one glues the sample twice: first using a super glue gel to connect it to the filament and secondly covering the whole surface with liquid super glue (Fig. 3.6). Measurement errors resulting from a possible magnetic moment of the glue will be neglected.

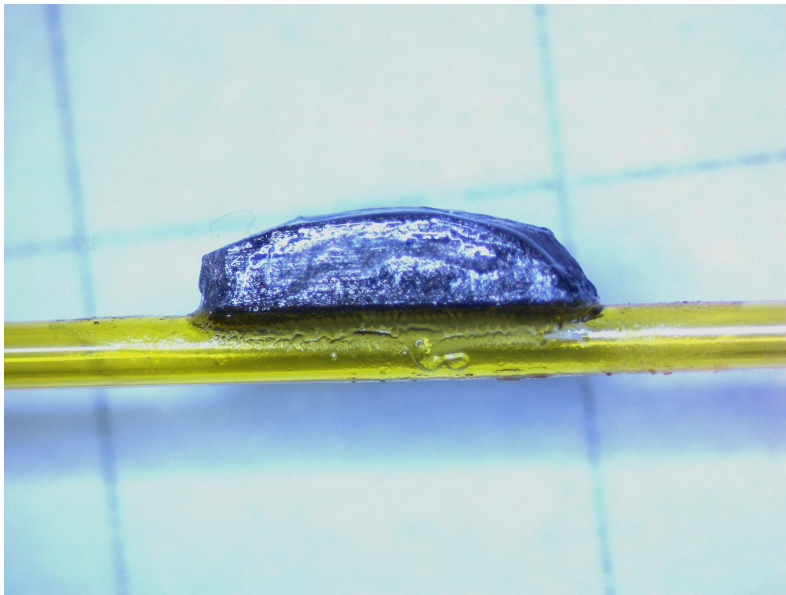


Figure 3.6.: A sample piece glued on the SQUID sample carrier [32, p. 25]

Subsequently, one connects the sample carrier to a stainless steel rod, which is then inserted cautiously into the device. As magnetization measurements should be done under vacuum conditions, the whole system has a leak-proof sealing, although the rod has to be moved in vertical direction. This is done by a stepper motor attached at the top.

The core of the measurement system consists of a 2nd order gradiometer coil made of superconducting wires like shown in Fig. 3.8. The major advantage of this type of coil is the compensation of stray magnetic fields and field gradients. As the wire is superconducting, only four conductor loops are needed.

¹⁵a light fibre from the eighties used for purposes other than intended

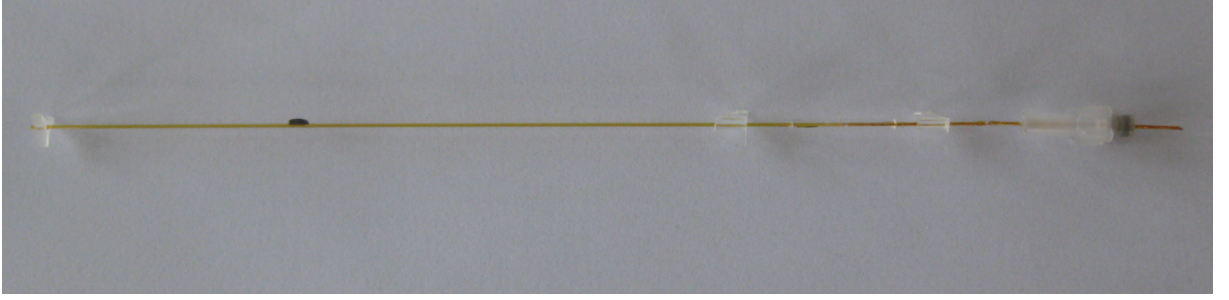


Figure 3.7.: SQUID sample carrier. Right hand the connector with the universal joint left of it. Left hand the position of the sample as seen in detail in Fig. 3.6 above. [32, p. 25]

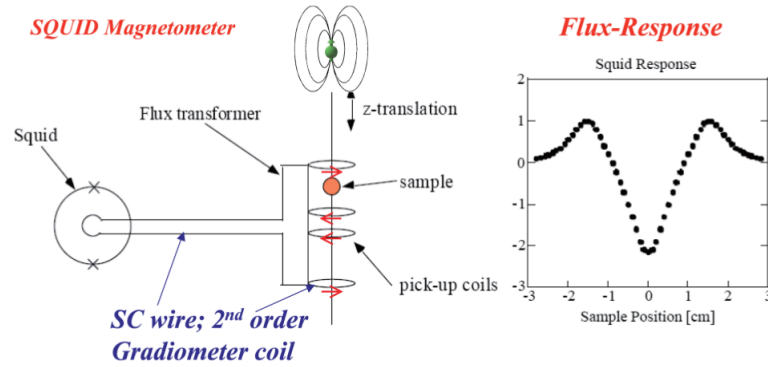


Figure 3.8.: Scheme of the core of the used SQUID magnetometer and graph of a perfect flux response [33, p. 5]

This coil interacts via a flux transformer (made of superconducting wire) with a DC SQUID¹⁶, a superconducting ring, cut into two parts and connected via Josephson junctions¹⁷ [35]. As Josephson's junctions are very thin, the wave function of one superconductor reaches the other superconductor, thus cooper pairs can tunnel from one to another with a certain probability. A constant current I_b is fed into the ring, splitting into two parts (Fig. 3.9). This corresponds to the formula

$$I_b = I_{J1} \sin(\Delta\varphi_1) + I_{J2} \sin(\Delta\varphi_2) \quad (3.2)$$

with $\Delta\varphi_1$ and $\Delta\varphi_2$ being the phase difference of the wave functions at the tunnel junctions. In the absence of an external magnetic field and if both junctions are of the same composition I_{J1} will be I_{J2} and constant. The phase shift at both contacts is $\Delta\varphi = \arcsin(I_b/2I_J)$. If $\vec{B} \neq 0$, there will be an additional screening current in the superconductor, which modifies the phase shift in the 2 Josephson junctions. Starting with the magnetic flux Φ , one can state

$$\Phi = \int \vec{B} \cdot d\vec{F} = \oint \vec{A} \cdot d\vec{s} = \frac{\hbar}{2e} \oint (\nabla\varphi) \cdot d\vec{s} = \frac{\Phi_0}{2\pi} (\Delta\varphi_1 - \Delta\varphi_2)$$

using the Ginzburg-Landau equations. One can furthermore write

$$\Delta\varphi_{1,2} = \Delta\varphi \pm \frac{\pi\Phi}{\Phi_0} \quad (3.3)$$

¹⁶invented in 1962 by Jaklevic et al. [34]

¹⁷isolating oxide layers of a thickness of 20 Å to 30 Å

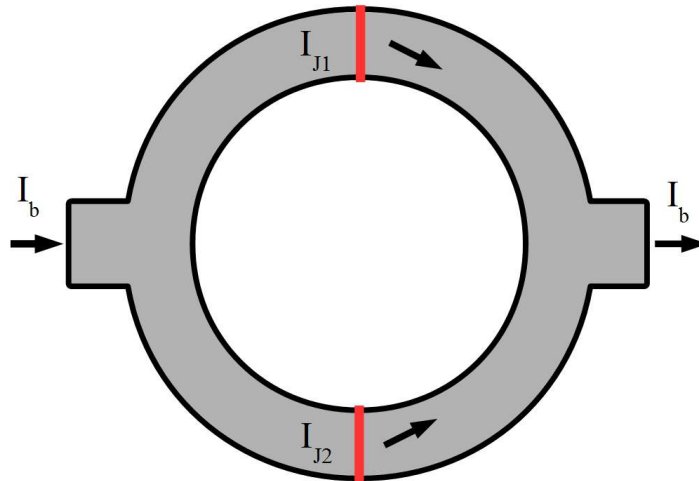


Figure 3.9.: Diagram of a DC SQUID. The current I_b enters and splits into two paths. The red barriers represent the Josephson junctions, which together separate the two superconducting regions.

as $\Delta\varphi_1 = \Delta\varphi_2 = \Delta\varphi$. Inserting this into 3.2 and using some trigonometric identities, one obtains

$$I = 2I_J \sin(\Delta\varphi) \cos\left(\frac{\pi\Phi}{\Phi_0}\right) \quad (3.4)$$

The Josephson current is modulated by the cosine term in equation 3.4 dependent on the external magnetic flux. The final result is a field dependent interference pattern, as the direction of the screening current changes direction every time, it increases by half integer multiples of Φ_0 . Using this technique, single flux quanta can be counted¹⁸. If the Josephson current exceeds the critical current I_c in one of the SQUID's branches, a voltage appears at the junction, which is proportional to Φ_0 and measured. One period of voltage variation corresponds to an increase of one flux quantum.

The sample is moved through the pick-up system several times during every measurement. The stepper position has to be calibrated before each measurement, in order to ensure a central position of the sample in the pick-up system. Finally, data is collected using a lock-in technique and interpreted by a computer.

¹⁸ $\Phi_0 = 2 \times 10^{-15}$ Wb

3.5. Heat capacity measurements

For heat capacity (as from now also called “specific heat”) measurements, two devices were used. Firstly, one of the Institute’s *Quantum Design PPMS* with ^3He inset [36] (lowest possible temperatures 0.4 K) and, secondly, a Nernst-calorimeter [37] (lowest possible temperatures 1.6 K, fields up to 11 T) constructed by the Institute’s former scientific staff [38, 39]. Both devices use the adiabatic ($C_p = (\partial Q/\partial T)_p$) relaxation time principle, but different masses. For the PPMS a sample mass of the order of 1 mg and cuboid shape is needed, if one wants to measure a heavy fermion compound¹⁹. One side has to be polished with fine sandpaper, then some μg Apiezon N vacuum grease have to be applied for improving the thermal contact. The sample is then fixed onto a sapphire platform with the Apiezon covered side to the bottom. The platform contains a heater as well as a thermometer and is connected to the ^3He puck by 4 wires to minimise thermal contact. This puck has 8 pins installed at the bottom, which have to be plunged into the ^3He inset rod. For more accurate information about the PPMS set-up, inter alia the ^3He cleaning process, I would like to refer to [25, Appendix C] and of course to the manual [36].

During the measuring process step heating is carried out. A certain amount of heat Q is transferred into the well-isolated sample by turning on the heater for a certain time. A temperature curve is being recorded. After the switch-off of the heater, the temperature relaxes to a value T_2 which is higher than the initial value T_1 . The relaxation time depends on the mass and the temperature itself. Via an evaluation software, specific heat can be calculated from the pulses.

The form of the pulses is explained by the fact, that when heating a spacious sample from one side, one obtains a temperature gradient, which will, due to the second law of thermodynamics, abate in time. A linearised integration method is used for evaluation of the pulses. Using the PPMS, specific heat measurements in the range of 0.4 to 20 K were carried out. With the Nernst calorimeter, however, the measurement range, in the case of this thesis, was selected from 1.7 to over 100 K for zero-field measurements. The inner parts of the Institute’s Nernst-calorimeter are shown in Fig. 3.11 in form of a schematic diagram. A ^4He bath cryostat with super-insulation contains a superconducting NbTi coil (by Cryogenic Consultants), which surrounds the sample. It is only operated in persistent mode. The sample has to be placed on a sapphire platform (containing the heater), adhered by Apiezon grease. This platform is connected to the rest of the device using nylon threads. Temperature sensors and radiation shields need to be placed near the sample. The vacuum cell containing the calorimeter’s core has to be sealed using an indium sealing, a wire which has to be pressed from indium chunks. The system’s vacuum configuration consists of a rotary vane rough pump and an oil diffusion pump. Temperatures below 4.2 K can be reached by pumping helium vapour from the ^4He reservoir²⁰. ^4He is also used as a heat exchange gas. It can be filled into the vacuum chamber so as to cool the sample and then removed again. One has to be careful not to put too much exchange gas into the chamber as for the measurement process again a good thermal isolation is needed. The cooling rate should not exceed 100 mK s^{-1} . Another possibility to reach a higher vacuum is to heat the chamber briefly to ablate helium molecules from surfaces.

The PPMS raw data have to be modified using a Mathematica programm [25, Appendix A]. With the calorimeter of Nernst’s type, data can be smoothed using the computer program. This was done by Herwig Michor, who helped the author to operate the device. The output data is written into a text file in two columns; one for the temperature and one for C_p/T .

¹⁹The electronic contribution to the specific heat is high at low temperatures, so is the Sommerfeld coefficient in our case, thus little mass is needed

²⁰A helium leak-proof rotary vane pump serves one to reach temperatures of 1.6 K the lowest

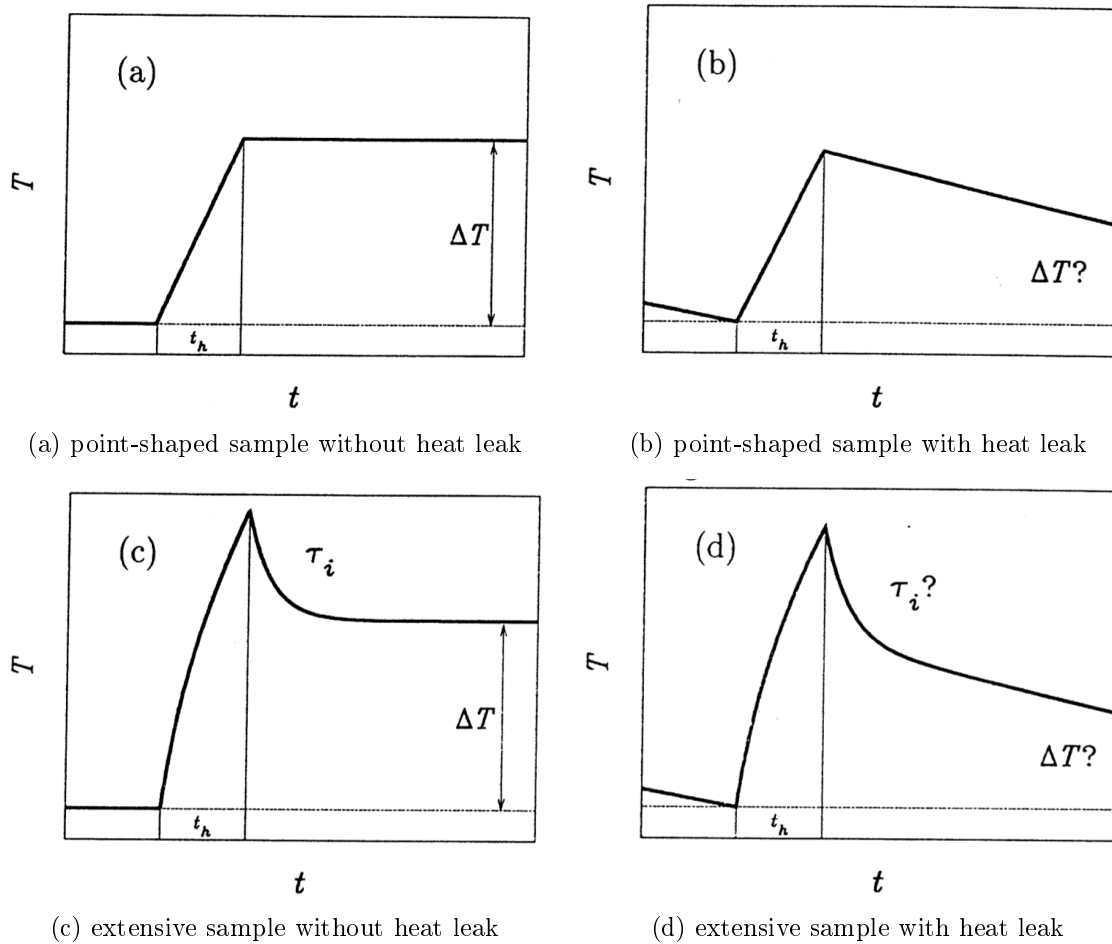


Figure 3.10.: Scheme of heating pulses. In a real quasi-adiabatic calorimeter, heat losses are unpreventable. In order to obtain qualitatively acceptable results, the evaluation (linearised integration method) has to count back from 3.10d to 3.10c. In doing so, the relaxation time τ_i can be ascertained [38, p. 5].

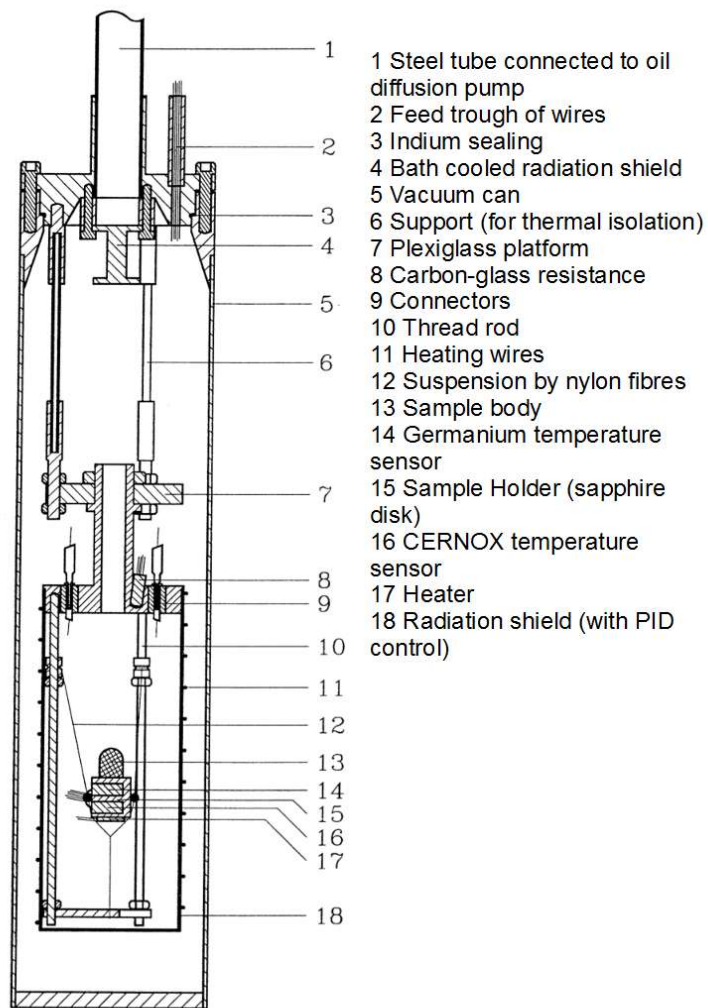


Figure 3.11.: Scheme of the inner parts of the Nernst-calorimeter (translated to English) [38, p. 23]

4. Results & discussion

The subsequent part of this thesis deals with the results obtained from measurements with the self-prepared intermetallic compounds, which all belong to the group of $RE_3T_4X_4$ (with RE = rare earth T = transition metal and X = Si, Ge, Sn). Members of this group exhibit a number of extraordinary properties, e.g. the Kondo behaviour, complex magnetism or intermediate valency. Especially low temperature behaviour is of high interest.

As it was already mentioned in the introduction, two series of samples were considered. Firstly, the substitution series of $Ce_3Pd_4Si_{4-x}Ge_x$, which was already studied before in [40], and, secondly, the series $Ce_3Pd_{4-x}Ni_xSi_4$. The latter was a completely new research, which gave the more interesting informations about this 3 – 3 – 4 group of heavy fermion materials.

It is known that a number of compounds containing rare earth elements feature Kondo lattice behaviour in the presence of RKKY interactions and crystalline electric field effects. Lipatov et al. [21] reported on the existence of the initial compound $Ce_3Pd_4Si_4$ in their work on the system Ce-Pd-Si. They stated that the aforementioned compound crystallises in $U_3Pd_4Si_4$ type with additional information: orthorhombic space group $Immm$ (no. 71); $a = 0.41618$, $b = 0.42640$, $c = 2.45744$ nm. Furthermore, the structure of this compound can be explained as a combination of AIB_2 -type and $BaAl_4$ layers, as shown in Fig. 4.1. Measurements of electrical resistivity, heat capacity and magnetic susceptibility give information about ground state properties. As it was done for $Ce_3Pd_4Si_4$ in [1], these properties shall be analysed here and compared with the results in this paper. This is done in the following sections for each sample separately and subsequently for all samples together as an overview.

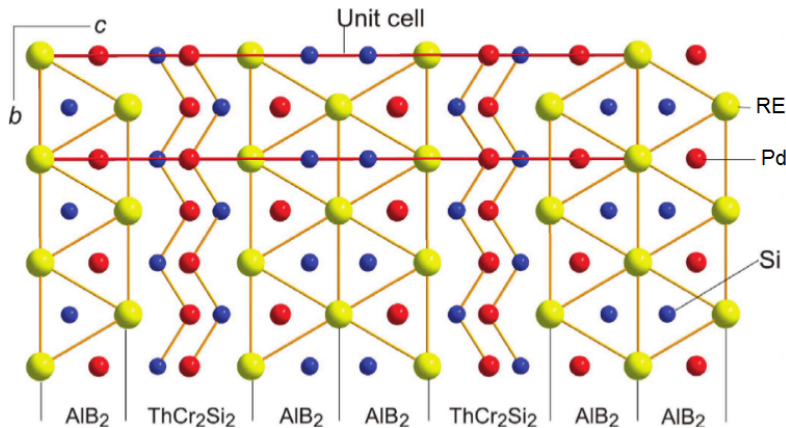


Figure 4.1.: Sketch of the crystal structure of $Ce_3Pd_4Si_4$ in projection along $[100]$ [1].

4.1. $Ce_3Pd_4Si_{4-x}Ge_x$ compounds

A rich variety of existing ternary germanium compounds in the system Ce-Pd-Ge was presented in [24]. Many of these intermetallics exhibit antiferromagnetic ground states, e.g. the dense

Kondo compound CePd_2Ge_2 [41]. The border compounds of this substitution were already investigated by Kneidinger et al. [1] and Im et al [42].

Unfortunately, it turned out that the preparation of these substitution compounds was accompanied by strong difficulties. 8 samples were prepared in this series, of which only 2 were of sufficient quality to be analysed as regards their physical behaviour. Too many impurity phases appeared in the other 6 samples¹, which were all tempered firstly at 800 °C and subsequently at 900 °C. None of the steps to improve the sample quality were effective. A crystallographic analysis yielded strong impurity phases of CePd_2Si_2 .

Eventually, only 2 samples were fully analysed and described of this series: $\text{Ce}_3\text{Pd}_4\text{Si}_{3.4}\text{Ge}_{0.6}$ and $\text{Ce}_3\text{Pd}_4\text{Si}_{2.8}\text{Ge}_{1.2}$.

4.1.1. $\text{Ce}_3\text{Pd}_4\text{Si}_{3.4}\text{Ge}_{0.6}$

It is quite obvious that a compound with only a small substitution of one element behaves like the initial substance, at least as respects its crystal structure. A sample of 2.97 g mass was prepared according to the desired stoichiometric composition, as described in section 3.1. The molar mass of this compound is $M = 985.11$ g. X-ray diffraction and subsequent analysis at the computer using the programme package *Powder Cell* yield a pattern, which is shown in Fig. 4.2. Rietveld refinement was done starting from the literature data in [1]. One can easily notice from the solid line in Fig. 4.2, that differences between observed and calculated peak data are small, i.e. an acceptable sample quality is secured.

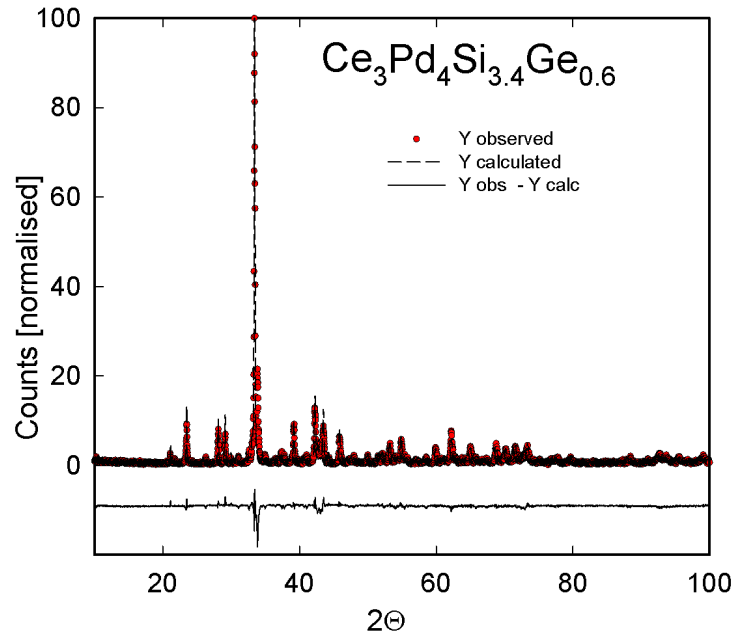


Figure 4.2.: X-ray diffraction pattern of $\text{Ce}_3\text{Pd}_4\text{Si}_{3.4}\text{Ge}_{0.6}$.

Results for the lattice parameters are shown in Table 4.1. The alloys with the substituted metalloid exhibit an increase of cell volume.

A common four terminal sensing method was used to obtain the temperature-dependent resistivity with both devices described in section 3.3. In the low temperature region, resistivity was also measured with applied external magnetic fields in the range up to 12 T.

¹ $\text{Ce}_3\text{Pd}_4\text{Si}_{2.2}\text{Ge}_{1.8}$, $\text{Ce}_3\text{Pd}_4\text{Si}_{1.6}\text{Ge}_{2.4}$, $\text{Ce}_3\text{Pd}_4\text{Si}_{0.2}\text{Ge}_{3.8}$, $\text{Ce}_3\text{Pd}_4\text{Si}_{0.4}\text{Ge}_{3.6}$, $\text{Ce}_3\text{Pd}_4\text{Si}_{0.6}\text{Ge}_{3.4}$, $\text{Ce}_3\text{Pd}_4\text{Si}_{0.8}\text{Ge}_{3.2}$

sample	a	b	c	V [nm ³]
$Ce_3Pd_4Si_4$	0.41618	0.42640	2.45744	0.4359
$Ce_3Pd_4Si_{3.4}Ge_{0.6}$	0.41647	0.42808	2.45684	0.4380
$Ce_3Pd_4Si_{2.8}Ge_{1.2}$	0.41602	0.42928	2.46171	0.4396

Table 4.1.: Cell parameters of $Ce_3Pd_4Si_{3.4}Ge_{0.6}$ are opposed to the lattice parameters of initial $Ce_3Pd_4Si_4$ and for better clarity also with $Ce_3Pd_4Si_{2.8}Ge_{1.2}$. All dimensions are given in nm.

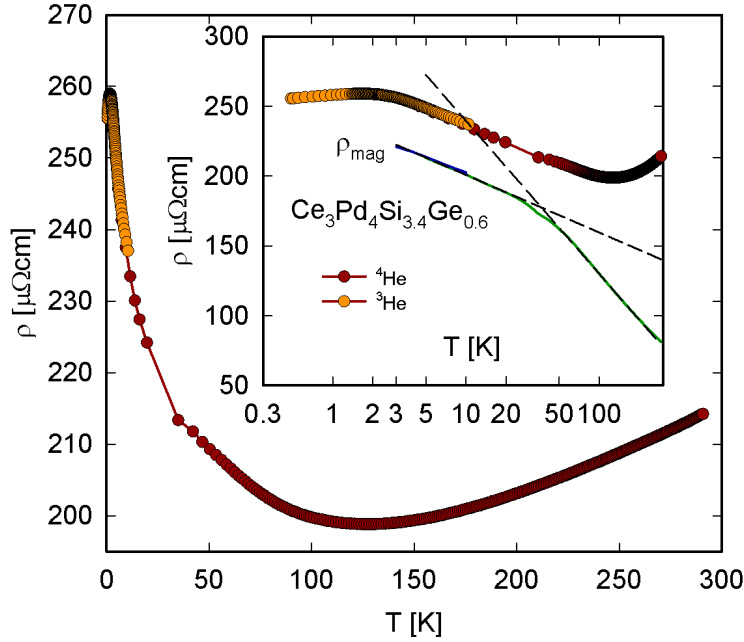


Figure 4.3.: Temperature dependent resistivity $\rho(T)$ of $Ce_3Pd_4Si_{3.4}Ge_{0.6}$ plotted on a linear and a logarithmic (inset) temperature scale. The inset picture also shows the magnetic contribution $\rho_{mag}(T)$ which is estimated by $\rho_{mag} \approx \rho(Ce_3Pd_4Si_{3.4}Ge_{0.6}) - \rho(La_3Pd_4Si_4)$. The dashed lines represent a least squares fit according to Eqn. (2.33) for different crystalline electric field levels (see text).

Fig. 4.3 shows the temperature dependent resistivity of the sample studied. Like with the other samples, a resistivity measurement of $\text{La}_3\text{Pd}_4\text{Si}_4$, taken from [1,25], was used as a non-magnetic reference, to calculate the magnetic part of resistivity. This is done simply by subtracting the electron-phonon interaction part (ρ of the La compound) from the total resistivity and by assuming that the phonon contribution to both compounds is similar. The temperature dependent resistivity $\rho(T)$ is typical for Kondo lattice systems. It exhibits a weak maximum at about 1.6 K, dropping at lower and higher temperatures. At about 125 K, there is a local minimum of $\rho(T)$. At more elevated temperatures the phonon contribution dominates the electrical resistivity. In 1972, Cornut and Coqblin investigated in their famous paper [12], the influence of the crystalline electric field (CEF) onto the Kondo effect. The 6-fold degenerate state of the total angular momentum splits in presence of the external CEF into 2 or 3 multipletts. In the case of cerium, it is possible to have a Kondo effect on each crystal field level, as far as they're well separated. Therefore, more than one thermal region with a logarithmic behaviour of $\rho(T)$ can be observed according to Eqn. (2.33), the lowest one representing the ground state. In Fig. 4.3, the two logarithmic contributions are marked by black dashed lines. From the ratio of the slopes, one can conclude the ratio of the multiplett number. For $\text{Ce}_3\text{Pd}_4\text{Si}_{3.4}\text{Ge}_{0.6}$, the calculated ratio is 2.65, which is near 2.

Fig. 4.4a shows the shift of $\rho(T)$ when an external magnetic field is applied. Strong external magnetic fields lower the resistivity in Kondo lattice systems due to the suppression of Kondo interaction. Long-range AFM, in general, becomes suppressed in external fields, too. The low temperature maximum in $\rho(T)$ is field dependent and shifts from 1.6 K at zero magnetic field to approximately 8 K at an external field of 12 T (fig. 4.4b). This is also common with cerium based Kondo lattice systems. Formally, a shift of the $\rho(T)$ maximum to higher temperatures means a raise of the Kondo temperature T_K .

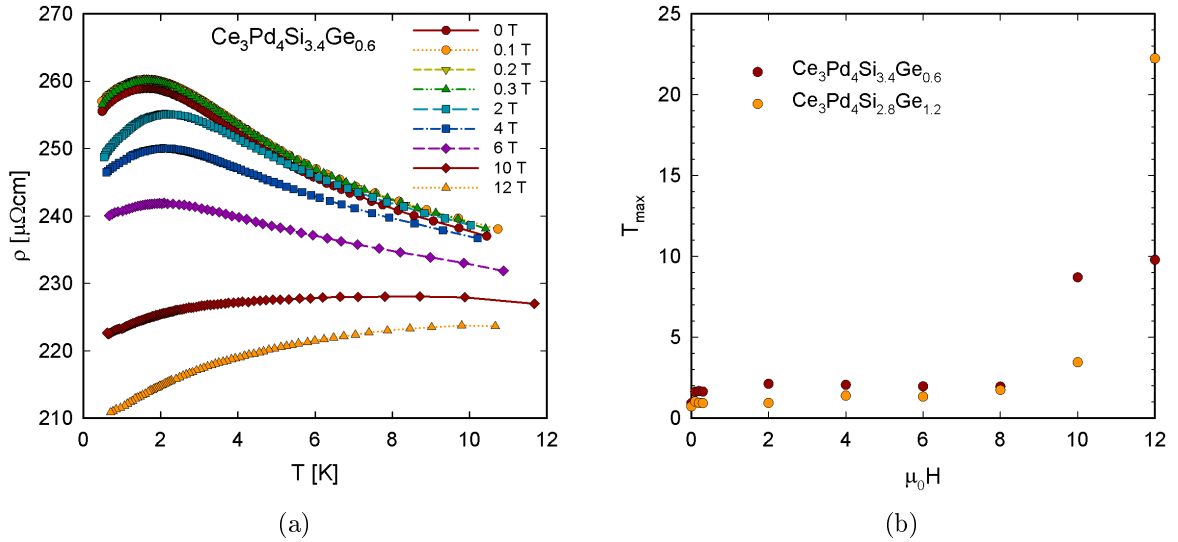


Figure 4.4.: Fig. (a) shows the low temperature dependent resistivity $\rho(T)$ of $\text{Ce}_3\text{Pd}_4\text{Si}_{3.4}\text{Ge}_{0.6}$ at different externally applied magnetic fields. Fig. (b) takes a closer look onto the shift of the low temperature resistivity maximum as a function of the external magnetic field for the two germanium compounds.

Moreover, measurements of magnetoresistivity have been carried out, i.e. modifying the external field in a small step size at a constant temperature and collecting resistivity data. The

proper definition of magnetoresistivity is

$$\frac{\Delta\rho}{\rho} := \frac{\rho(T, \vec{B}) - \rho(T, \vec{B} = \vec{0})}{\rho(T, \vec{B} = \vec{0})}. \quad (4.1)$$

Theories to describe magnetoresistivity, which can be divided into a classical and a quantum part, are various. The classical part is always present and can be derived from the Boltzmann equation. It is determined by the so-called magnetic operator. The quantum mechanical part is determined by magnetic scattering processes, which occur e.g. for compounds containing 4f-impurities. In heavy fermion systems, a large magnetoresistivity is frequently observed. At high temperatures compared to T_K , it is negative like seen in Fig. 4.5, whereas at temperatures $T \ll T_K$, it can have positive values. For systems where RKKY-interactions are predominant compared to Kondo interaction, long-range magnetic ordering is possible in either a ferromagnetic or a antiferromagnetic ground state. If an external magnetic field is applied, the unscreened magnetic moments become oriented toward the field direction. Fig. 4.5 furthermore shows a bend for the two 2 lowest temperatures at approximately 1 T. This is a sign for a metamagnetic state as part of a magnetic field induced ordering transition.

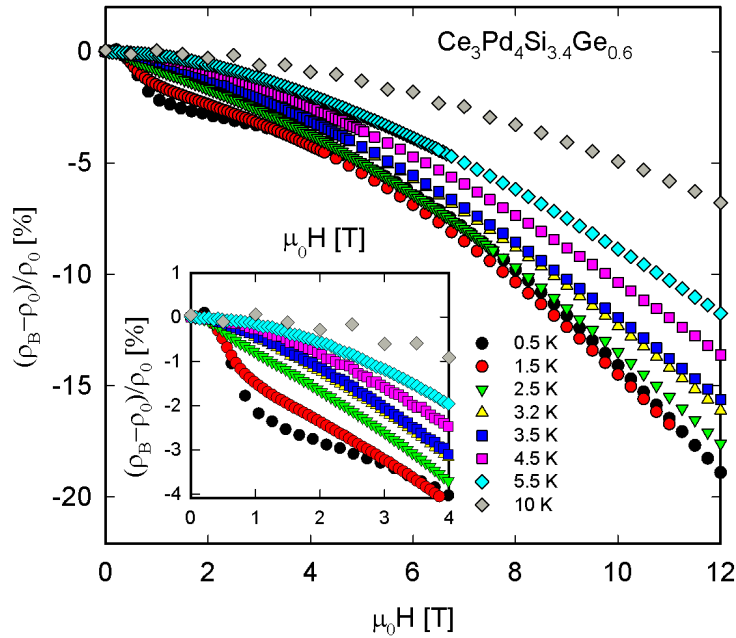


Figure 4.5.: Isothermal magnetoresistivity measurement of $Ce_3Pd_4Si_{3.4}Ge_{0.6}$ at different temperatures for external magnetic fields in the range of 0 T to 12 T. The inset displays details of the entire picture at low fields.

(Molar) heat capacity, as shown in Figs. 4.6 and 4.7 (as C_p/T), was measured using the PPMS. The results were analysed and normalised to one atom of cerium. Similarly to the measurements of other properties, magnetic fields have been applied in order to discover alterations of $C_p(T, \vec{B})$. It has to be stated here that strong scattering in $C_p(T)$ occurred for higher applied magnetic fields, mainly in the low temperature region. This was regarded as a general problem in every measurement, therefore the results for higher fields should be understood critically. Nevertheless, a general tendency can be perceived. A local maximum in C_p is situated at about 2 K, which must be of magnetic origin, because it is suppressed by external magnetic fields. A minimum occurs at about 6 K. The inset in Fig. 4.6 reveals an inflexion point at about 2 K,

which might also be a sign for magnetic ordering. Unfortunately, more accurate measurements were blocked by the PPMS device.

In Fig. 4.7, where C_p/T is plotted versus T , the dashed line represents calculated magnetic entropy. This quantity is gained by subtracting the approximate phonon contribution to specific heat, i.e. C_p/T of the lanthanum based sample, and subsequent integration of the difference curve. Below 2 K, however, the lanthanum data can't be used as it becomes superconducting, thus an approximation was made. An entropy of $R \cdot \ln(2)$ is not reached within the permitted limits.

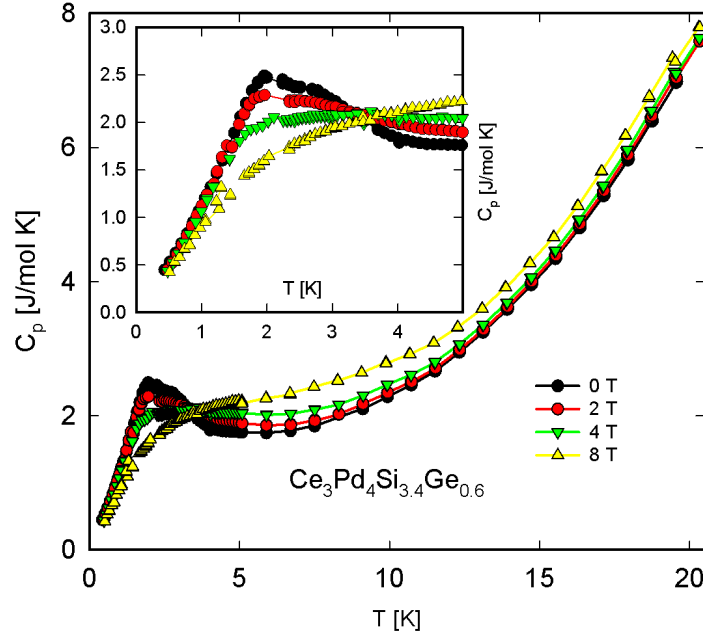


Figure 4.6.: Temperature dependent heat capacity $C_p(T)$ of $Ce_3Pd_4Si_{3.4}Ge_{0.6}$ for three cerium atoms. The inset shows details at low temperatures.

Fig. 4.8 shows the temperature dependent magnetic susceptibility obtained with the SQUID magnetometer, described in section 3.4. It is plotted as $1/\chi(T)$. Field scaling of the experimental data evidences good sample quality and the absence of magnetic impurities. In order to get information about the magnetic state of the cerium ion, one applies a modified Curie-Weiss law:

$$\chi(T) = \chi_0 + \frac{C}{T - \theta_p} \quad (4.2)$$

This law takes into account a temperature independent Pauli contribution χ_0 . It is possible to gather information on the effective magnetic moment μ_{eff} (from the Curie constant C) as well as on the paramagnetic Curie temperature (θ_p) by fitting experimental data in Fig. 4.8 (above 50 K) to Eqn. (4.2). The fitting procedure was executed using a least squares fit with the help of *TableCurve2D v.5.01*. Results for the named quantities are displayed in Fig. 4.8, too. The effective magnetic moment $\mu_{eff} = 2.51\mu_B$ is close to that of the Ce- $4f^1$ electronic configuration [$\mu_{eff}(Ce^{3+}) = 2.54\mu_B$]. The negative paramagnetic Curie temperature ($\theta_p = -33$ K) yields antiferromagnetic interactions among the Ce ions in the context of CEF effects. This is correspondent with the results obtained for $Ce_3Pd_4Si_4$ in [1]. The result from [42] for θ_p of $Ce_3Pd_4Ge_4$ is equal ($\theta_p = -33$ K). Deviations from the CW behaviour at lower temperatures can be accounted for by moderate crystal field splitting of the Ce^{3+} ground multiplet.

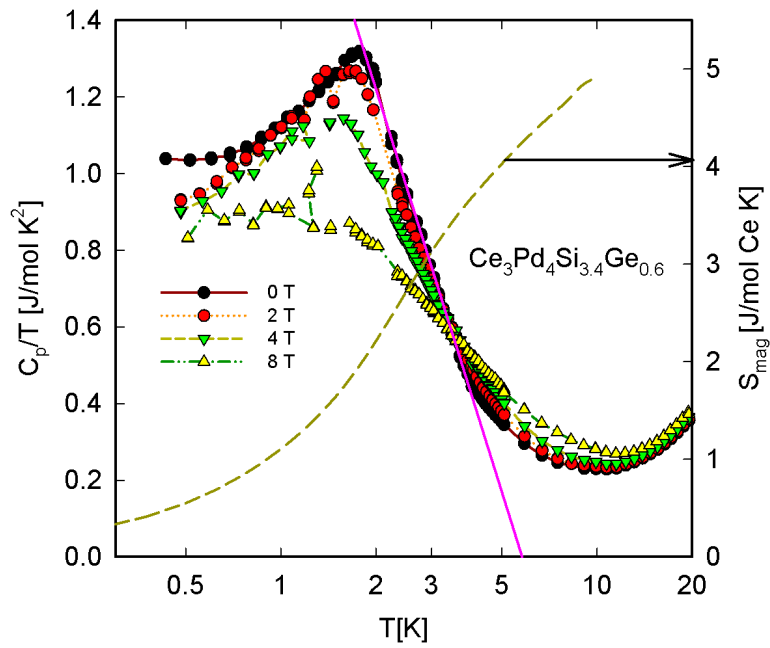


Figure 4.7.: Temperature dependent heat capacity $C_p(T)$ of $Ce_3Pd_4Si_{3.4}Ge_{0.6}$, plotted as C_p/T vs. $\ln(T)$. The solid line represents a least-squares fit to reveal negative logarithmic behaviour, which is characteristic for a non-Fermi liquid. The dashed line shows the calculated magnetic entropy referring to the right axis.

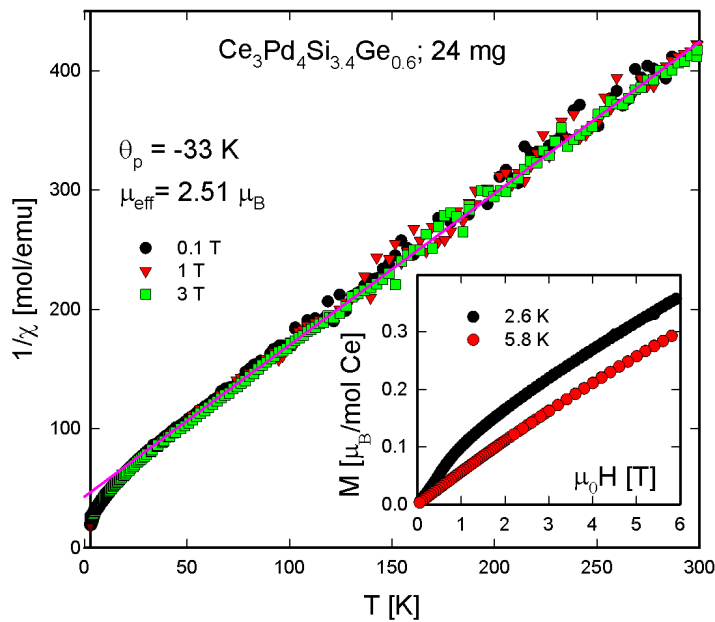


Figure 4.8.: Temperature dependent magnetic susceptibility $\chi(T)$ of $Ce_3Pd_4Si_{3.4}Ge_{0.6}$, plotted as $1/\chi$ vs. T . 3 measurements at different external fields (0.1 T, 1 T, 3 T) have been taken into account. The solid line represents a modified Curie-Weiss fit. The inset displays the isothermal magnetisation at 2.6 K and 5.8 K.

Looking more closely onto the inset of Fig. 4.8 reveals some interesting facts, displayed in Fig. 4.9. The first derivative of the isothermal magnetisation curve ($T = 2.6$ K) has a maximum at about 0.45 T. The non-linear rise of $M(H)$ in this region is a sign for a magnetic phase transition. $\text{Ce}_3\text{Pd}_4\text{Si}_{3.4}\text{Ge}_{0.6}$, being at 2.6 K in an antiferromagnetic ground state, becomes a field induced antiferromagnet for $H > 0.45$ T, as the spins get arranged in the external magnetic field. For the higher temperature measurement, no such phase transition exists, as there is also no antiferromagnetic ground state (thermal disorder). The transition can also be observed in Fig. 4.5, where magnetoresistivity shows an inflexion point at about the same field strength.

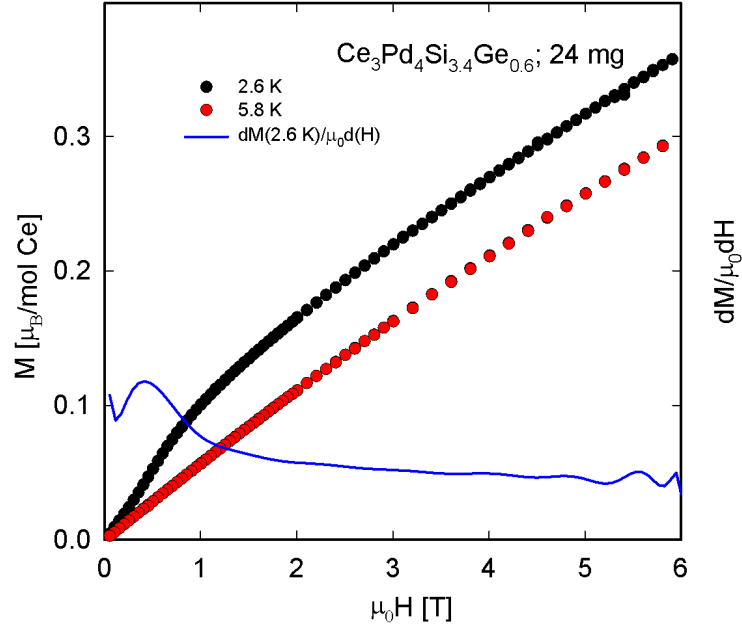


Figure 4.9.: Isothermal magnetisation curve of $\text{Ce}_3\text{Pd}_4\text{Si}_{3.4}\text{Ge}_{0.6}$. The blue line represents the first derivative of at 2.6 K, referring as well to the scale of the left axis. Only the units are different. As it can be clearly seen, the slope of the magnetisation curve at 2.6 K has a maximum at about 0.45 T. A non-linearity of the magnetization curve yields a transition from one magnetic state to another. In between it is called a metamagnetic state.

4.1.2. $\text{Ce}_3\text{Pd}_4\text{Si}_{2.8}\text{Ge}_{1.2}$

The second sample of the substitution series Si by Ge was the last suitable one. 1.93 g of the alloy were disposable for property studies. It possesses a molar mass of $M = 1011.85$ g. The X-ray diffraction pattern and subsequent analyses are shown in App. B (Fig. B.1) and in Tab. 4.1.

Temperature dependent resistivity is plotted in Fig. 4.10. A minimum can be observed at about 100 K. $\rho(T)$ also contains a maximum near to the lower limit of the measurement range. This, most likely, reflects Kondo lattice behaviour. The inset in Fig. 4.10 shows the resistivity on a logarithmic temperature scale. Furthermore, the magnetic contribution is represented by the solid line and obtained by subtraction of the resistivity of $\text{La}_3\text{Pd}_4\text{Si}_4$, i.e. a resistivity without magnetic contributions. Of course, a rather small error is made by doing so, inter alia due to the substitution. The dashed straight lines reflect the Kondo contribution in the presence of CEF

splitting. While at low temperatures, only the ground state is populated, more elevated temperatures cause the first excited state to be reached and thus a bend in the magnetic contribution. (cp. [12])

In comparison to the starting material $Ce_3Pd_4Si_4$, the pronounced maximum around 10 K vanished, but the more sharp kink around 10 K might reflect the onset of long range magnetic order. Although the chemical and thus electronic surrounding of Ce remains almost unchanged by the isostructural and isoelectronic substitution of silicon by germanium, the increase of the unit cell volume releases pressure. As a consequence, hybridisation weakens and thus the Ce $4f^1$ state becomes more localised.

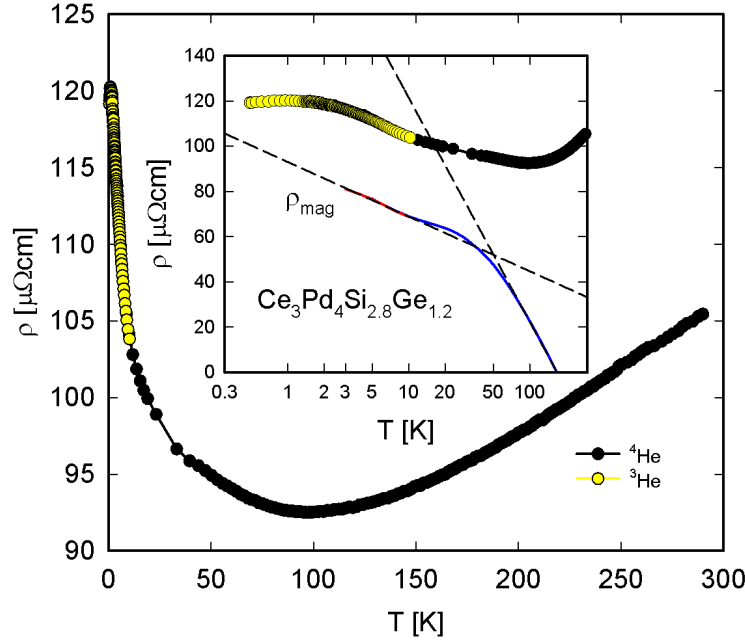


Figure 4.10.: Temperature dependent resistivity $\rho(T)$ of $Ce_3Pd_4Si_{2.8}Ge_{1.2}$ plotted on a linear and a logarithmic (inset) temperature scale. The solid line represents the magnetic contribution to electrical resistivity, while the dashed lines illustrate the Kondo effect on different CEF levels.

Figure 4.11 reveals the low temperature measurements with the 3He system. External magnetic fields of various magnitude are applied to the sample. The resistivity maximum shifts towards higher temperatures for augmenting magnetic fields, as also shown in Fig. 4.4b. Moreover, these external fields suppress the Kondo effect and yield a linearisation of the curve.

Magnetoresistivity measurements gave results similar to the ones of $Ce_3Pd_4Si_{3.4}Ge_{0.6}$. At 0.5 K, a change of curvature can be observed, when surpassing approximately 1.5 T. This is also a sign for a magnetic transition.

Figure 4.13 represents the (molar) heat capacity of $Ce_3Pd_4Si_{2.8}Ge_{1.2}$, measured at various external magnetic fields. A more detailed representation (inset) exhibits 2 local maxima for the zero-field curve at about 2 and 5 K, which become suppressed when external magnetic fields interact with the sample. Fig. 4.14, where C_p/T vs. T is plotted on a logarithmic temperature scale, reveals similar behaviour. The two local maxima can be interpreted as magnetic transitions. The dashed line represents the magnetic entropy, which possesses a saddle point at about 10 K. This is most likely due to a big energy gap between CEF levels in the Schottky contribution to specific heat.

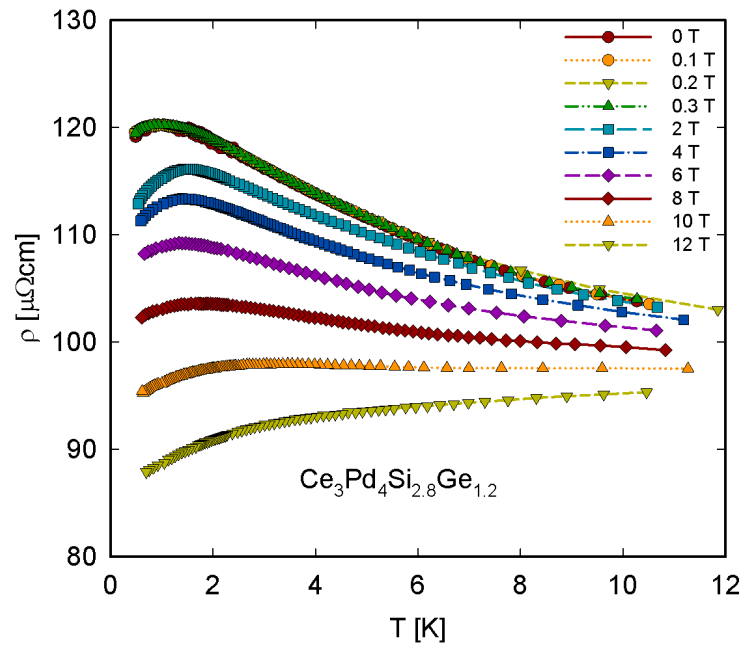


Figure 4.11.: Low temperature dependent electrical resistivity $\rho(T, B \neq 0)$ of $\text{Ce}_3\text{Pd}_4\text{Si}_{2.8}\text{Ge}_{1.2}$ at different externally applied magnetic fields.

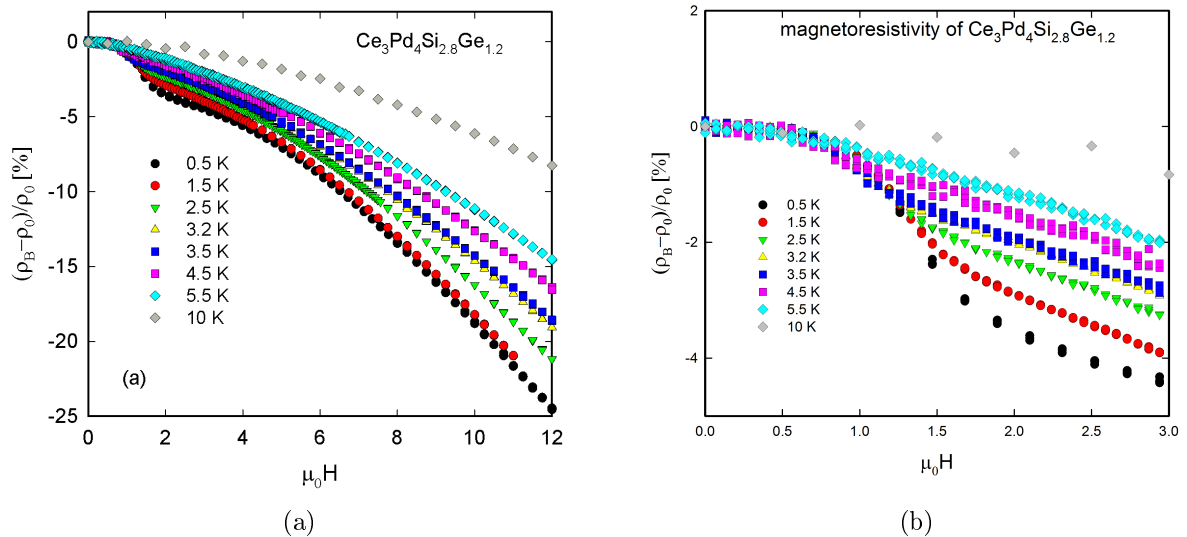


Figure 4.12.: Isothermal magnetoresistivity measurement of $\text{Ce}_3\text{Pd}_4\text{Si}_{2.8}\text{Ge}_{1.2}$ at different temperatures for external magnetic fields in the range of 0 T to 12 T. 4.12b displays the details of 4.12a regarding the magnetic transition at low fields.

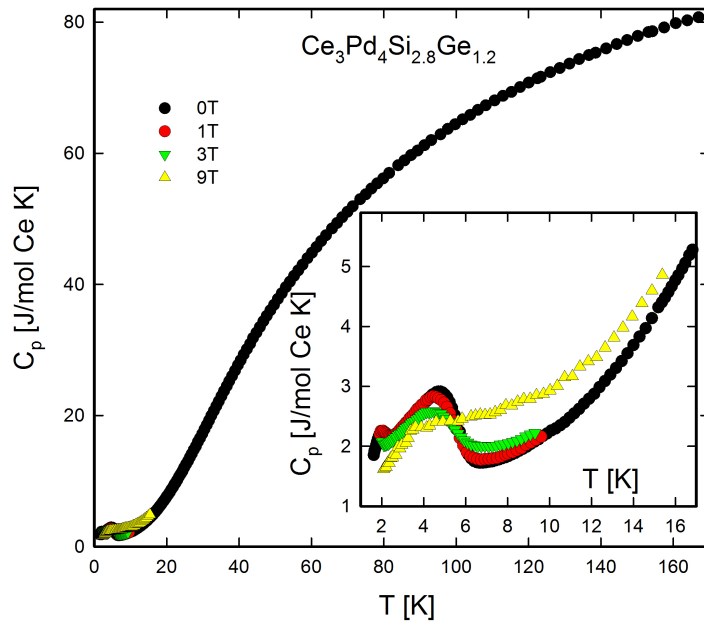


Figure 4.13.: Temperature dependent heat capacity $C_p(T)$ of $Ce_3Pd_4Si_{2.8}Ge_{1.2}$ in a large temperature range. Different external fields in the range of 0 T to 9 T have been applied to analyse the magnetic part of C_p . The inset shows details at low temperatures.

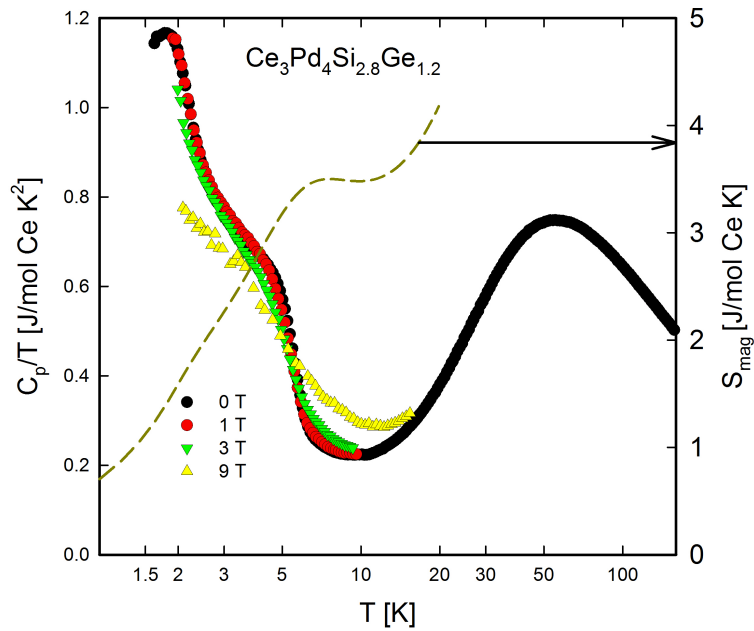


Figure 4.14.: Temperature dependent heat capacity $C_p(T)$ of $Ce_3Pd_4Si_{2.8}Ge_{1.2}$, plotted as C_p/T vs. $\ln(T)$. The dashed line represents the magnetic entropy S_{mag} , referring to the right axis.

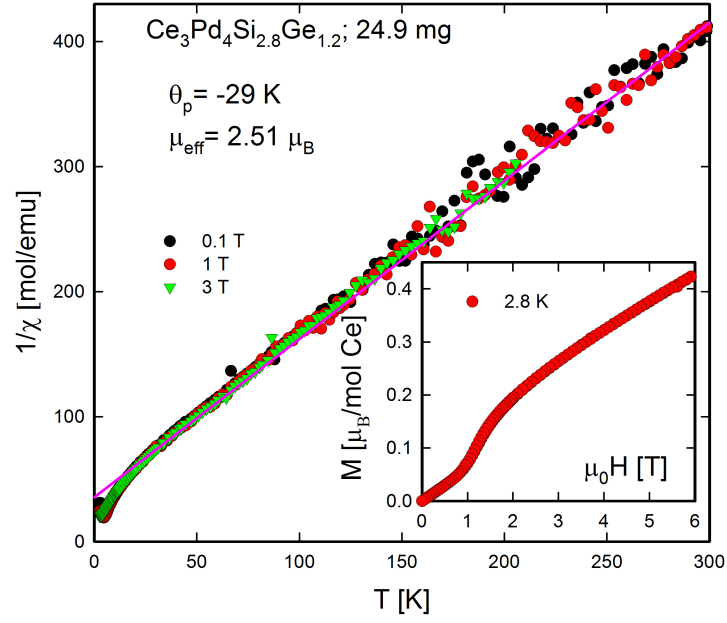


Figure 4.15.: Temperature dependent magnetic susceptibility $\chi(T)$ of $\text{Ce}_3\text{Pd}_4\text{Si}_{2.8}\text{Ge}_{1.2}$, plotted as $1/\chi$ vs. T . Three measurements at different external fields have been made. The solid line represents the modified Curie-Weiss fit. The inset displays the isothermal magnetisation at 2.8 K.

The magnetisation measurements show a similar behaviour like the preceding sample. In Fig. 4.15, the inverse susceptibility is plotted versus temperature. The isothermal magnetisation curve, shown in the inset, has an inflexion point at 1.4 T. A CW-fit revealed a paramagnetic Curie temperature of -29 K and an effective magnetic moment similar to the one of the free cerium ion.

In Fig. 4.16, the inset of Fig. 4.15 is displayed with a least-square fit of the lower temperature data. Furthermore, the first derivative dM/dH has a maximum at 1.2 T. Therefore, a transition from an antiferromagnetic state to a field induced, more ferromagnetic state occurs. In between, it's called a metamagnetic state. In our case, the external magnetic field destroys (antiferro)magnetic structures, thus causing a rise of magnetisation.

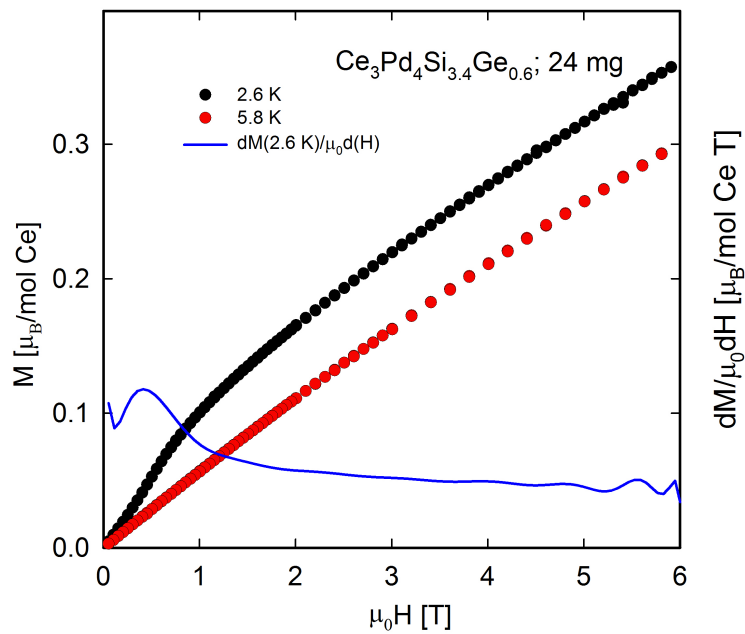


Figure 4.16.: Isothermal magnetisation curve of $Ce_3Pd_{4S}i_{2.8}Ge_{1.2}$. The blue line represents the first derivative of the curve, referring as well to the scale of the left axis. As it can be stated, the slope of the magnetisation curve at 2.8 K has a maximum at approximately 1.2 T. Like with the previously discussed alloy a non-linearity in the magnetization curve yields a transition from one magnetic state to another. In between it is called a metamagnetic state. The scale is used equally for the magnetisation and its derivative.

4.2. $\text{Ce}_3\text{Pd}_{4-x}\text{Ni}_x\text{Si}_4$ compounds

After the more or less successful attempts with substituting silicon, the next preparation step was to substitute palladium with nickel, two transition elements of the 10th group, i.e. isoelectronic. Palladium forms part of the 4*d* elements with an atomic weight of $A = 106,42$ and atomic number $Z = 46$, while nickel is a lighter element ($A=58.69$, $Z=28$) and member of the 3*d* elements. Results from x-ray diffraction measurements, i.e. unit cell parameters, are illustrated in Tab. 4.2 and in Fig. 4.17. The detailed X-ray diffraction patterns plus corresponding fits are shown in the appendix in Figs. B.2-B.5.

sample	a	b	c	V [nm ³]
$\text{Ce}_3\text{Pd}_4\text{Si}_4$	0.41618	0.42640	2.45744	0.4361
$\text{Ce}_3\text{Pd}_{3.75}\text{Ni}_{0.25}\text{Si}_4$	0.41837	0.42955	2.46030	0.4421
$\text{Ce}_3\text{Pd}_{3.5}\text{Ni}_{0.5}\text{Si}_4$	0.41706	0.42673	2.44955	0.4360
$\text{Ce}_3\text{Pd}_3\text{NiSi}_4$	0.41408	0.42195	2.42381	0.4235
$\text{Ce}_3\text{Pd}_2\text{Ni}_2\text{Si}_4$	0.41136	0.42032	2.41294	0.4172

Table 4.2.: Comparison of lattice parameters and cell volume of $\text{Ce}_3\text{Pd}_{4-x}\text{Ni}_x\text{Si}_4$ compounds. Substituting palladium ($Z = 46$) with nickel ($Z = 28$) yields smaller interatomic distances in the crystal. The unit used is nm

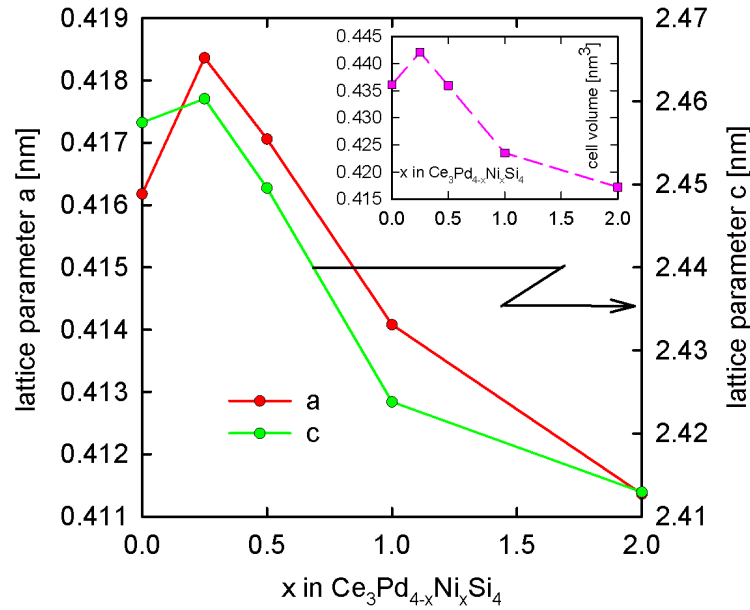


Figure 4.17.: Lattice parameters of $\text{Ce}_3\text{Pd}_{4-x}\text{Ni}_x\text{Si}_4$ samples as a function of the stoichiometric composition

Detailed summaries of the diffraction patterns of this series can be viewed in app. B. Fig. 4.17 clearly shows the decrease of lattice parameters and, therefore, of the unit cell volume in direction of higher nickel substitution rates.

4.2.1. $Ce_3Pd_{3.75}Ni_{0.25}Si_4$

For reasons of investigating changes in material properties at low substitution rates, this stoichiometric composition was chosen. The total molar mass adds up to $M = 946.45$ g. A total mass of 2.48 g was prepared.

Fig. 4.18 shows the electrical resistivity $\rho(T)$ in a temperature range of 0.4 K to 300 K. The results were obtained by four-point sensing resistance measurements in the 4He and the 3He cryostat. The inset exhibits the same curve in a logarithmic diagram. Kondo lattice behaviour can be observed. A minimum in the resistivity curve is located at approximately 150 K, whilst a maximum can be seen at 3.1 K. The magnetic contribution of $\rho(T)$ is again estimated by subtraction of $\rho(T)$ of the La-based compound. In between the minimum and the maximum, classical Kondo behaviour can be observed, inter alia in the inset of Fig. 4.18, where two straight lines in the logarithmic diagram represent the logarithmic Kondo contribution in the presence of CEF splitting. The relatively sharp maximum around 3 K might be a sign for long range magnetic order rather than for Kondo coherence.

In Fig. 4.19, the influence of an external magnetic field on $\rho(T, \vec{B})$ is depicted. Magnetic fields shift the maximum of the curve towards higher temperatures and lower resistivities. Nevertheless, the temperature shift in this sample is only small (0.7 K).

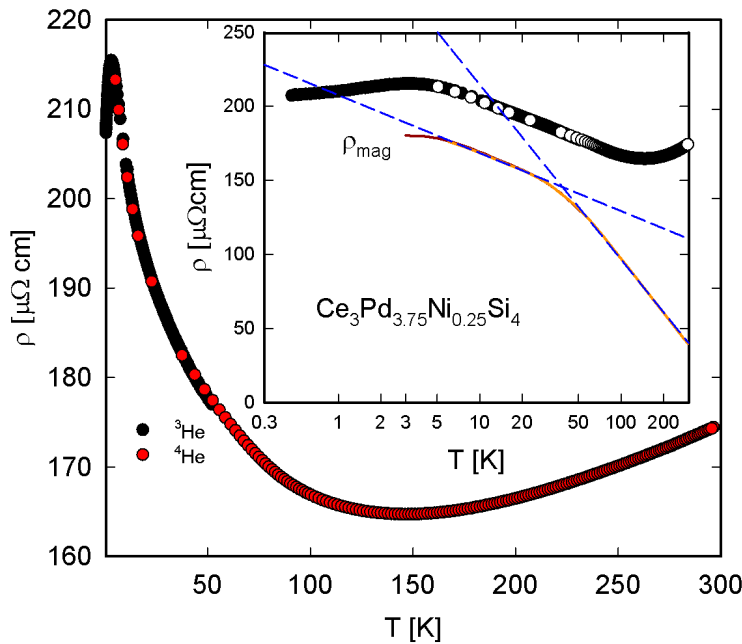


Figure 4.18.: Temperature dependent resistivity $\rho(T)$ of $Ce_3Pd_{3.75}Ni_{0.25}Si_4$ plotted over a linear and a logarithmic (inset) temperature scale. Moreover, the magnetic contribution is again represented by the solid line. A least squares fit according to Eqn. (2.33) was done for two crystal field levels represented by the dashed lines.

The isothermal magnetoresistivity $(\rho_B - \rho_0)/\rho_0$, given in percent is plotted in Fig. 4.20 for different temperatures. Within the lowest temperature curve, i.e. 1.5 K, a deviation in curvature can be observed, represented by the pink line in the inset. This is regarded as a sign of a phase transition.

Heat capacity (plotted in Figs. 4.21 and 4.22) was measured at the Institute's PPMS system using the 3He inset. At more elevated temperatures a power law can be observed. Just below

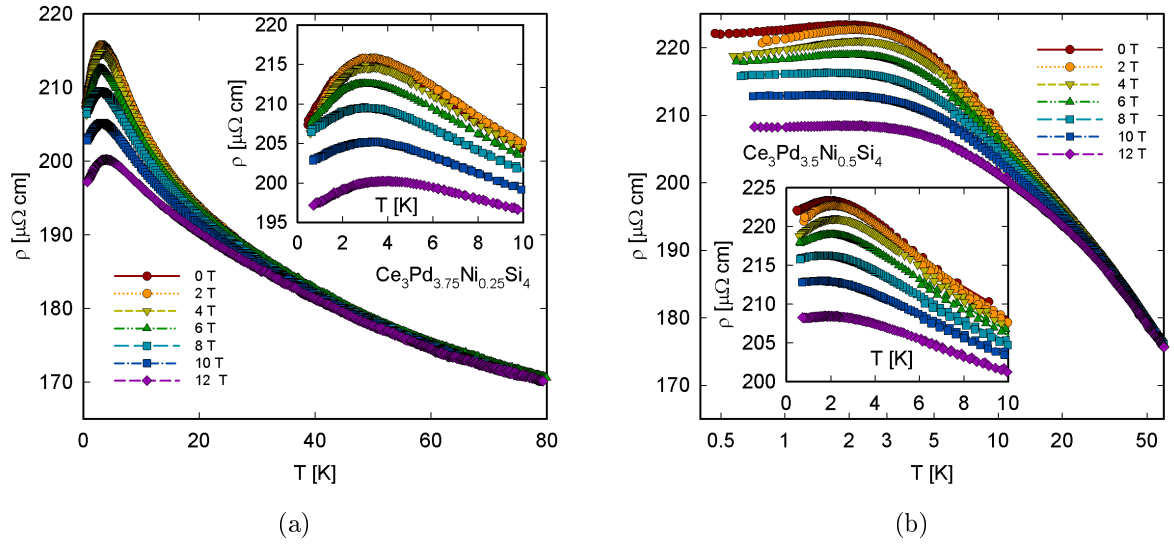


Figure 4.19.: Temperature dependent resistivity $\rho(T, \vec{B})$ of $\text{Ce}_3\text{Pd}_{3.75}\text{Ni}_{0.25}\text{Si}_4$ at different external magnetic fields. Fig. 4.19a features a linear temperature scale, while Fig. 4.19b is based on a logarithmic depiction. The inset of both figures presents details at low temperatures.

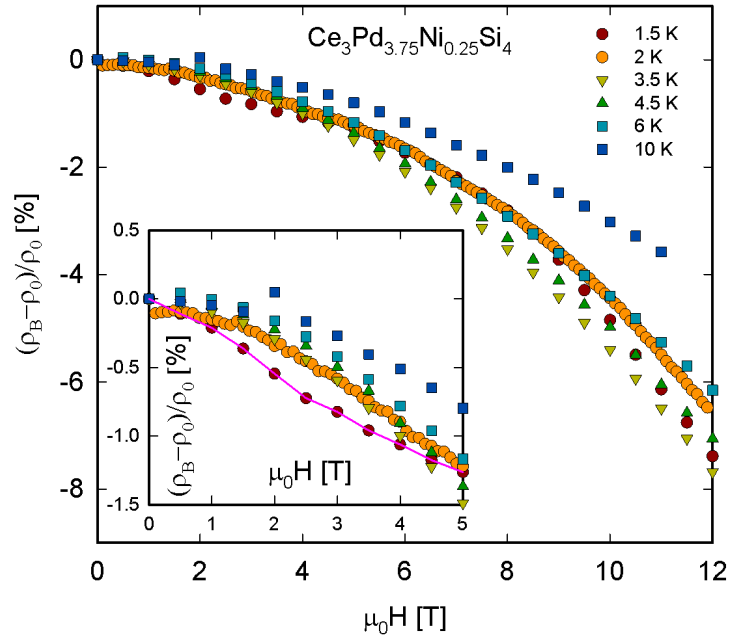


Figure 4.20.: Isothermal magnetoresistivity of $\text{Ce}_3\text{Pd}_{3.75}\text{Ni}_{0.25}\text{Si}_4$ at different temperatures. The inset depicts details at low temperatures. The measurement at 1.5 K is accentuated by the solid pink line, showing deviations from the other measurements. This is regarded as a sign of a phase transition between 1.5 and 2 K. Points were measured in an interval of 0.5 T except for the measurement at 2 K, where a smaller interval was chosen tentatively.

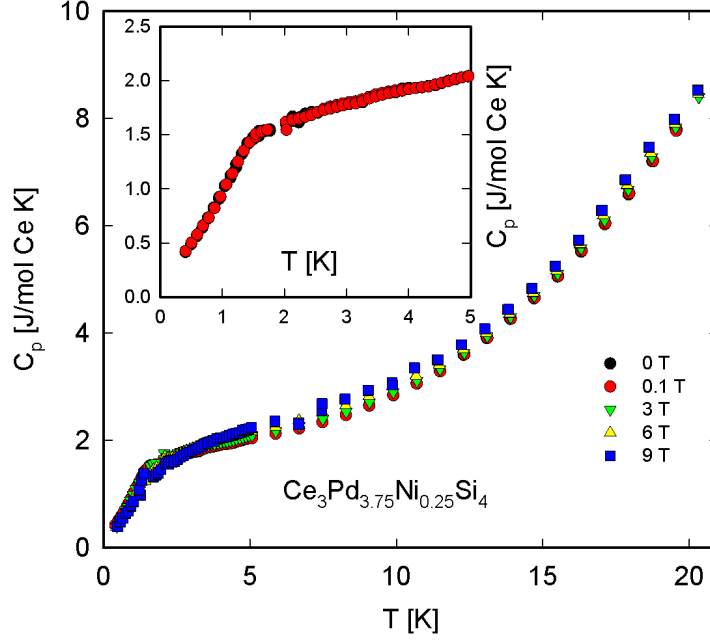


Figure 4.21.: Temperature dependent heat capacity $C_p(T)$ of $Ce_3Pd_{3.75}Ni_{0.25}Si_4$. The inset displays details for low temperatures and absence of strong magnetic fields. The results are given for three cerium atoms.

1.5 K, a bend can be seen in the curve. In order to take a closer look onto the low temperature properties, C_p/T is plotted over a logarithmic temperature scale in Fig. 4.22. Starting from high temperatures, the curve reaches a local maximum at 1.4 K, then decreases until 0.8 K, where a local minimum occurs. The magnetic entropy of $Ce_3Pd_{3.75}Ni_{0.25}Si_4$ was obtained by integration of C_p/T and is represented by the dashed line in Fig. 4.22. The distinct features in $C_p(T)$, in the context to observations made from transport data, unambiguously refer to the onset of long range magnetic order driven by the initial Pd/Ni substitution.

Magnetisation measurements yield a similar behaviour like in the Si/Ge substitution series with similar qualitative results. The paramagnetic Curie temperature was identified with -40 K, which is rather large. However, it drops even further towards the higher substitution. The effective magnetic moment amounts to $2.53\mu_B$, a value still near to that of the free cerium ion. The inset, where isothermal magnetisation is plotted, doesn't reveal any transition. Unfortunately, no further measurements have been performed yet.

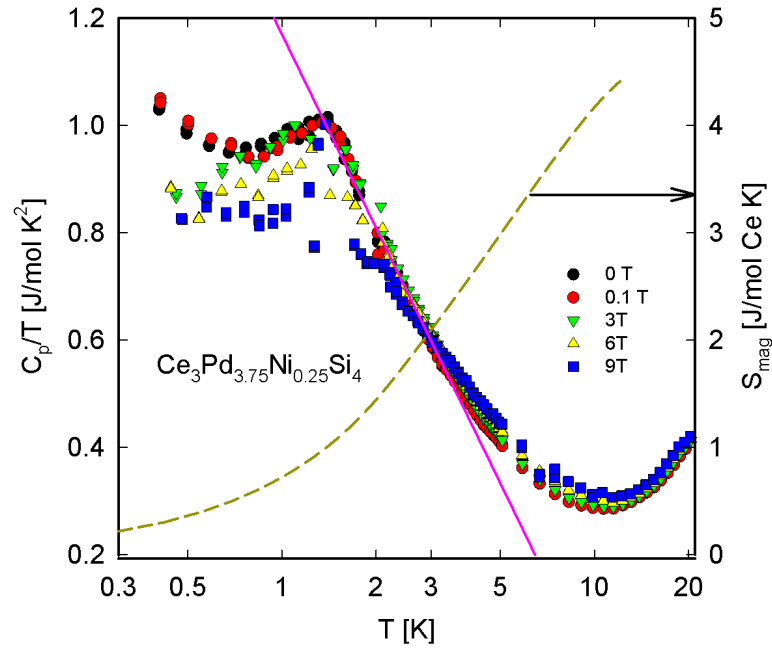


Figure 4.22.: Temperature dependent heat capacity of $\text{Ce}_3\text{Pd}_{3.75}\text{Ni}_{0.25}\text{Si}_4$ plotted as C_p/T vs. $\ln(T)$. The dashed line represents the magnetic entropy, which rises continuously. The solid line marks the negative logarithmic part in C_p/T , which is typical for non-Fermi-liquids.

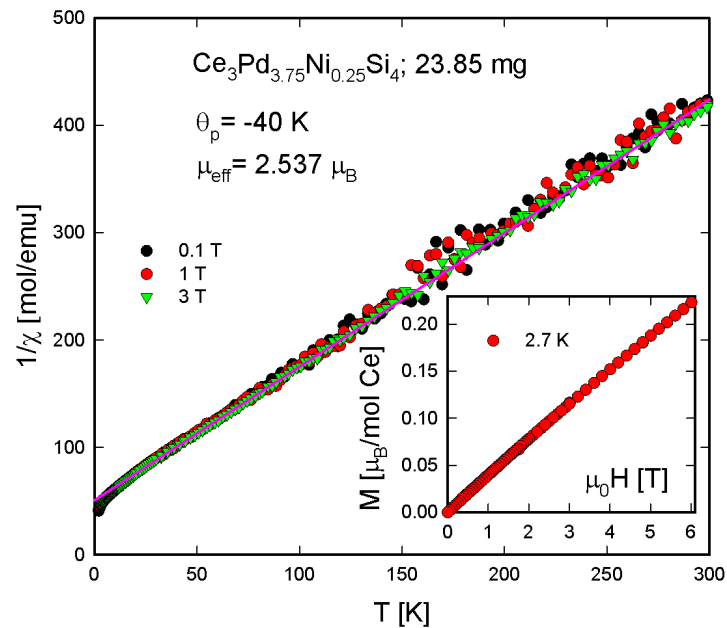


Figure 4.23.: Temperature dependent magnetic susceptibility $\rho(T)$ of $\text{Ce}_3\text{Pd}_{3.75}\text{Ni}_{0.25}\text{Si}_4$, plotted as $1/\chi$ vs. T . 3 measurements at different external fields, as seen in the picture, have been executed. A modified Curie-Weiss fit according to formula 4.2. The isothermal magnetisation at 2.7 K

4.2.2. $Ce_3Pd_{3.5}Ni_{0.5}Si_4$

2.37 g of this compound were prepared using the processes mentioned above. The molecular mass of $Ce_3Pd_{3.5}Ni_{0.5}Si_4$ amounts to $M = 934.5$ g.

The following figures reveal the behaviour of transport properties at low temperatures. Temperature dependent resistivity is plotted in Fig. 4.24 and Fig. 4.25. A minimum in the resistivity curve is located at approximately 175 K. The maximum at 2.1 K is difficult to spot, as the slope around is very moderate.

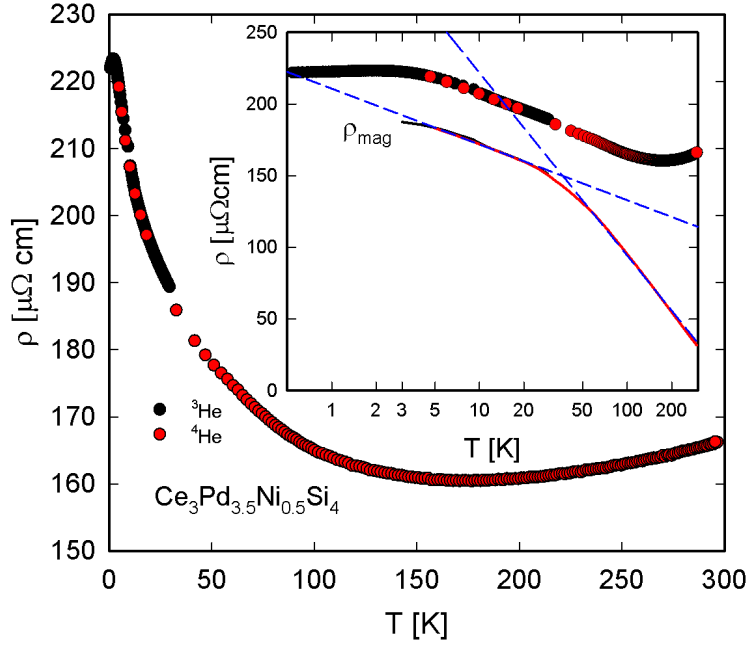


Figure 4.24.: Temperature dependent resistivity $\rho(T)$ of $Ce_3Pd_{3.5}Ni_{0.5}Si_4$ plotted over a linear and a logarithmic (inset) temperature scale. The solid line represents the magnetic contribution, which is calculated approximatively by subtracting $\rho(T)$ of the non-magnetic lanthanum compound. Again, measurements are separated in black and red, according as they have been done with the 3He or the 4He device. Blue, dashed lines represent a least squares fit of the logarithmic Kondo contribution in the presence of crystalline electric field splitting.

Magnetic field ramps, like shown in Fig. 4.26 look similar to that of $Ce_3Pd_{3.75}Ni_{0.25}Si_4$. Taking a closer look onto the 0.5 K measurement curve reveals a possible bend near 3 T.

Heat capacity measurements are plotted in Fig. 4.27 and fig. 4.28. C_p/T at low temperatures is characterised by a negative logarithmic contribution, being a characteristics of non-Fermi liquid behaviour due to the proximity of long range magnetic order near $T = 0$.

Last but not least, magnetisation measurements were performed again using the SQUID magnetometer. The pink line shows the least squares fit according to the modified CW-law. The paramagnetic Curie temperature even dropped to -42 K, while a lower value for μ_{eff} was calculated ($2.41\mu_B$). The negative θ_p is again a sign for possible antiferromagnetic interactions among the cerium ions. Nevertheless, neither $\chi(T)$ nor $M(\mu_0H)$ show any characteristic anomaly as respects magnetic order.

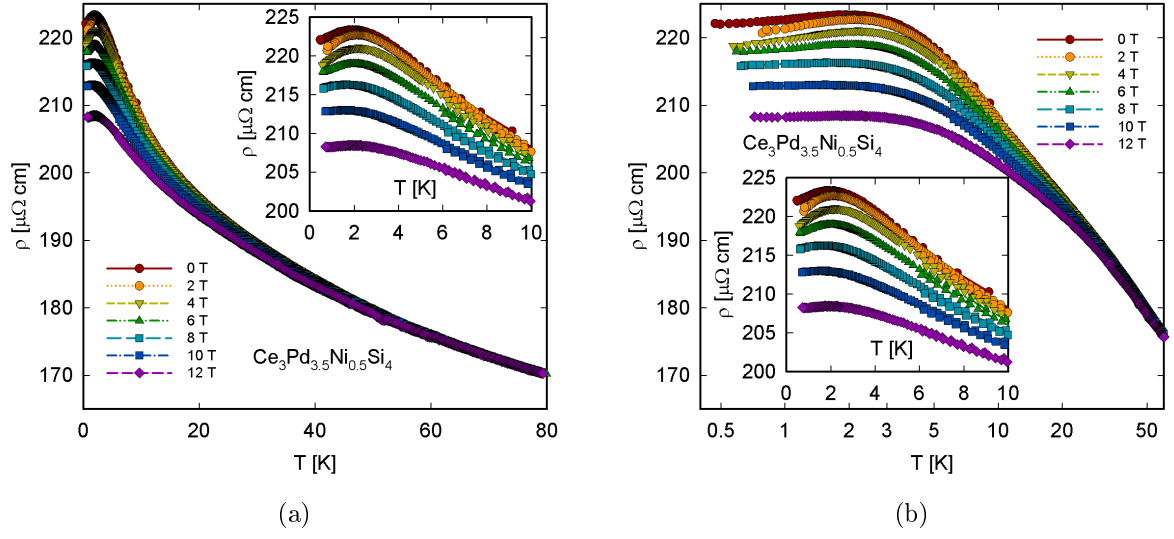


Figure 4.25.: Low temperature dependent electrical resistivity $\rho(T, B \neq 0)$ of $\text{Ce}_3\text{Pd}_{3.5}\text{Ni}_{0.5}\text{Si}_4$ at different externally applied magnetic fields in linear (4.25a) and logarithmic design.

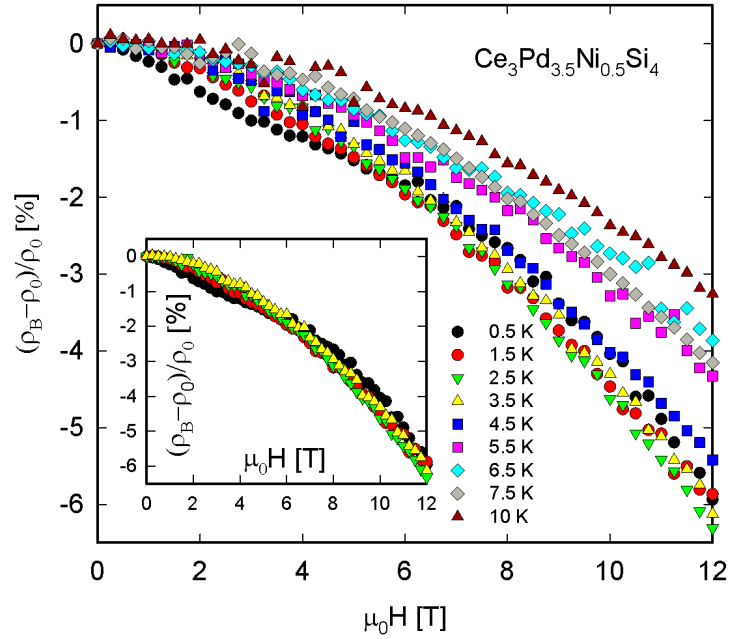


Figure 4.26.: Isothermal magnetoresistivity of $\text{Ce}_3\text{Pd}_{3.5}\text{Ni}_{0.5}\text{Si}_4$ at different temperatures. The inset depicts details at low temperatures.

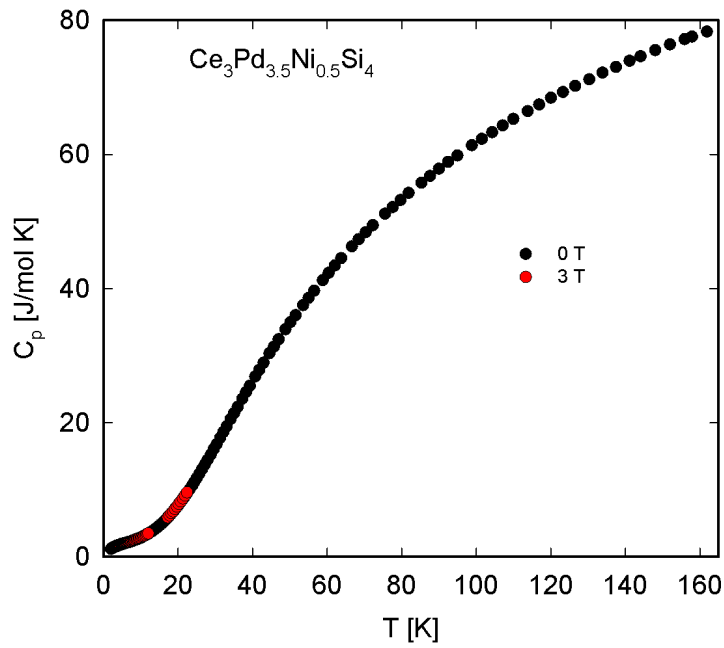


Figure 4.27.: Temperature dependent heat capacity $C_p(T)$ of $Ce_3Pd_{3.5}Ni_{0.5}Si_4$.

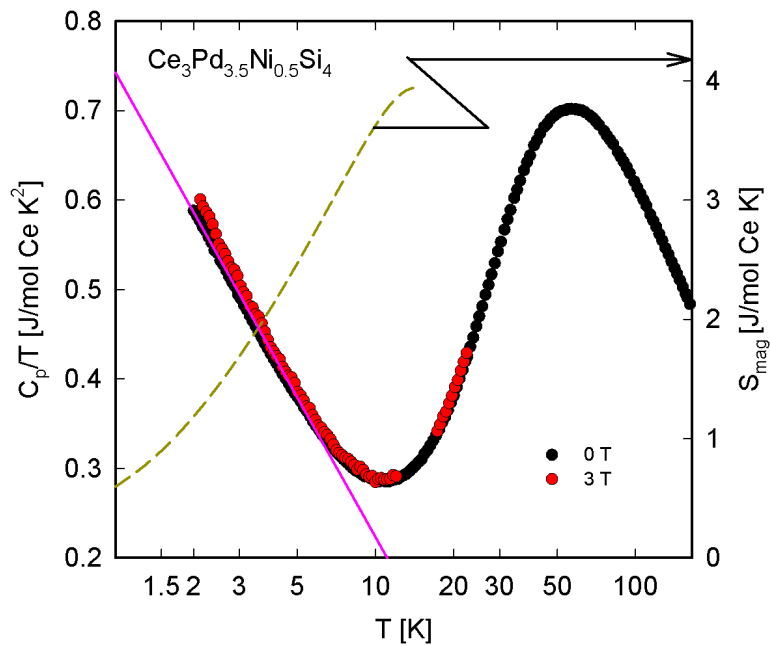


Figure 4.28.: Temperature dependent heat capacity of $Ce_3Pd_{3.5}Ni_{0.5}Si_4$ plotted as C_p/T vs. $\ln(T)$ with the solid line representing a least-squares fit of the negative logarithmic part in C_p/T , which occurs with non-Fermi-liquids at low temperatures. The dashed line stands for the calculated magnetic entropy.

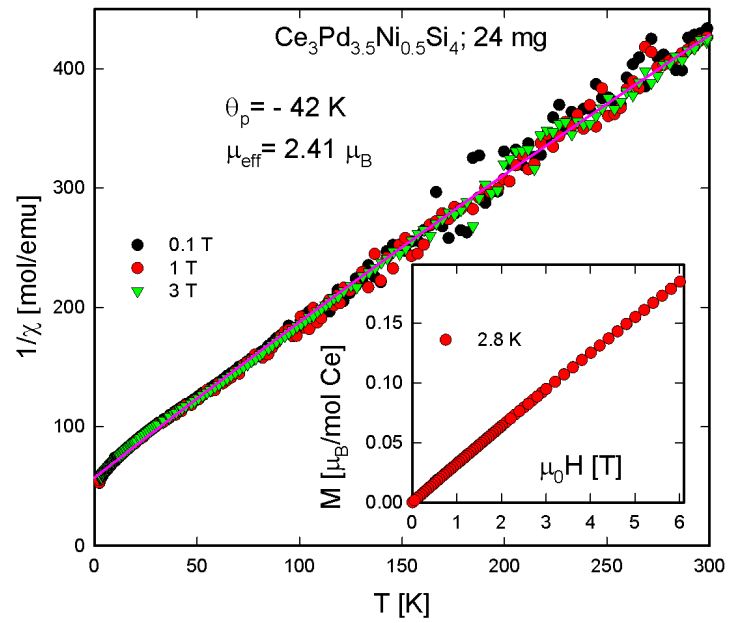


Figure 4.29.: Temperature dependent magnetic susceptibility $\chi(T)$ of $\text{Ce}_3\text{Pd}_{3.5}\text{Ni}_{0.5}\text{Si}_4$, plotted as $1/\chi$ vs. T . Three measurements at different external fields (0.1 T, 1 T, 3 T) have been carried out. The solid line represents the modified Curie-Weiss fit according to Eqn. (4.2). The inset displays the isothermal magnetisation at 2.8 K. The results are given for 1 cerium atom.

4.2.3. $Ce_3Pd_3NiSi_4$

2.47 g of this stoichiometric composition (molar mass $M = 910.94$ g) was produced for further analyses of this series. Transport properties were similar to the ones of the lower substitution rates. The resistivity, seen in Fig. 4.30, shows Kondo lattice behaviour with an observable minimum at approximately 210 K. When going down in temperature, a logarithmic increase of resistivity is at hand, leading to a maximum at 2.9 K with a small slope around it. Applying an external magnetic field during the measurement suppresses the maximum so that the low temperature resistivity up to 5 K is nearly constant (Fig. 4.31).

The magnetoresistivity, revealed in Fig. 4.32, is negative with only a small value of 2.5% at 12 T.

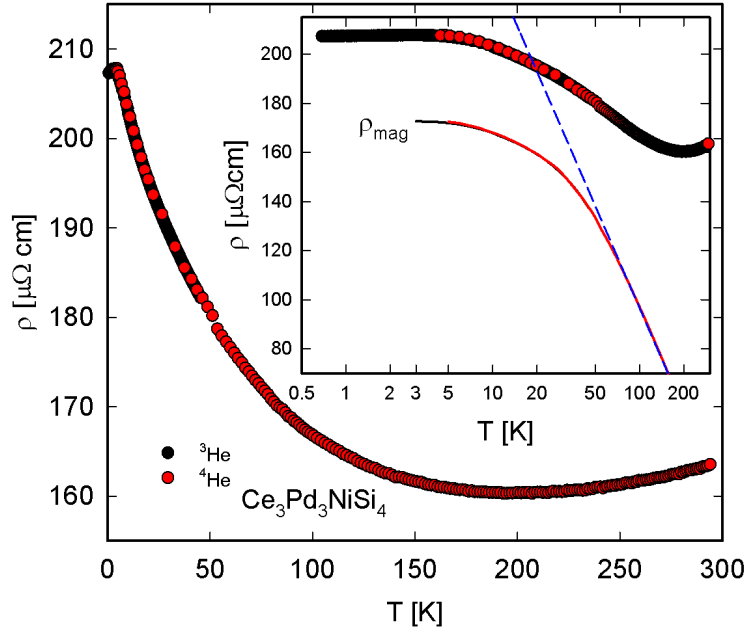


Figure 4.30.: Temperature dependent resistivity $\rho(T, B = 0)$ of $Ce_3Pd_3NiSi_4$ obtained from two devices (sec. 3.3) and plotted on a linear and a logarithmic (inset) temperature scale. Again, the magnetic part of resistivity is represented by the solid line, whereas the dashed line should emphasise Kondo resistivity.

The temperature dependent heat capacity was determined with the Nernst calorimeter and plotted in Figs. 4.33 and 4.34. At low temperatures a logarithmic behaviour of C_p/T is eminent, followed by a local minimum at 10 K. Slightly above 50 K, a maximum is reached with $\gamma = C_p/T = 0.7$ J/molK² computed for one cerium atom.

Magnetisation measurements with this sample were performed. Subsequent analyses yielded a large paramagnetic Curie temperature of $\theta_p = -62$ K as well as a high effective magnetic moment μ_{eff} of $2.59 \mu_B$. The corresponding CW-fit is plotted in pink in Fig. 4.35. Deviations from the fit at low temperatures can be observed below 20 K. There is no characteristic sign for any transition within this plot. As the cooling was executed using ⁴He cooling, only temperatures above 2 K can be reached. Possible transitions at lower temperatures are thus not visible.

4.2.4. $Ce_3Pd_2Ni_2Si_4$

In this compound palladium is half substituted by nickel, which is the highest substitution rate discussed within this thesis. This makes the total molar mass the lowest of all sam-

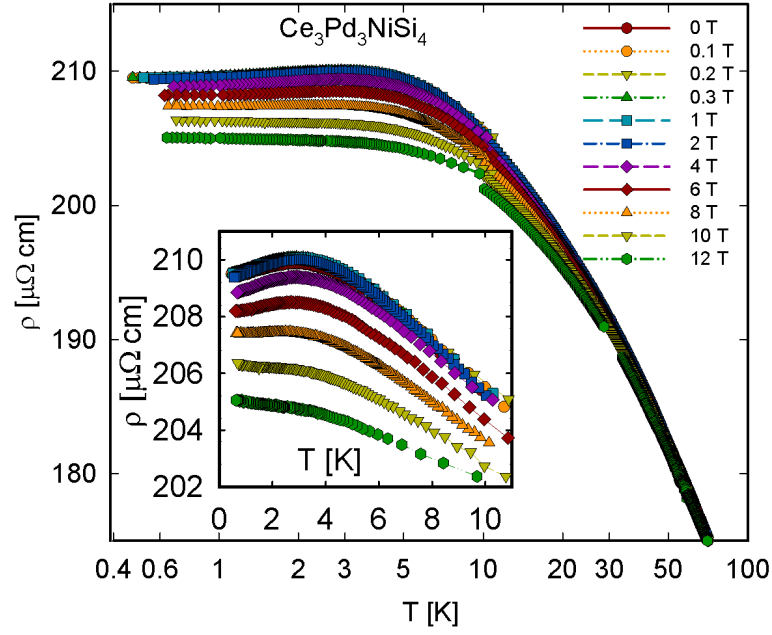


Figure 4.31.: Temperature dependent electrical resistivity $\rho(T, B \neq 0)$ of $\text{Ce}_3\text{Pd}_3\text{NiSi}_4$ at low temperatures plotted as $\rho(T)$ vs. $\ln(T)$. For a clearer view on the details, the inset displays the lowest temperature region on a linear scale.

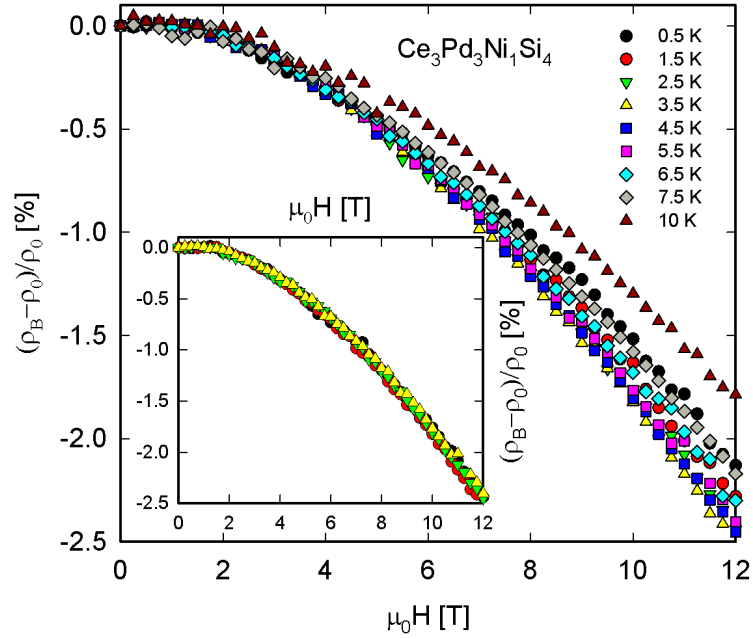


Figure 4.32.: Isothermal magnetoresistivity measurement of $\text{Ce}_3\text{Pd}_3\text{NiSi}_4$ at different temperatures for external magnetic fields in the range of 0 T to 12 T. In the inset the 4 lowest measured temperatures are displayed due to their possible concealment in the main picture.

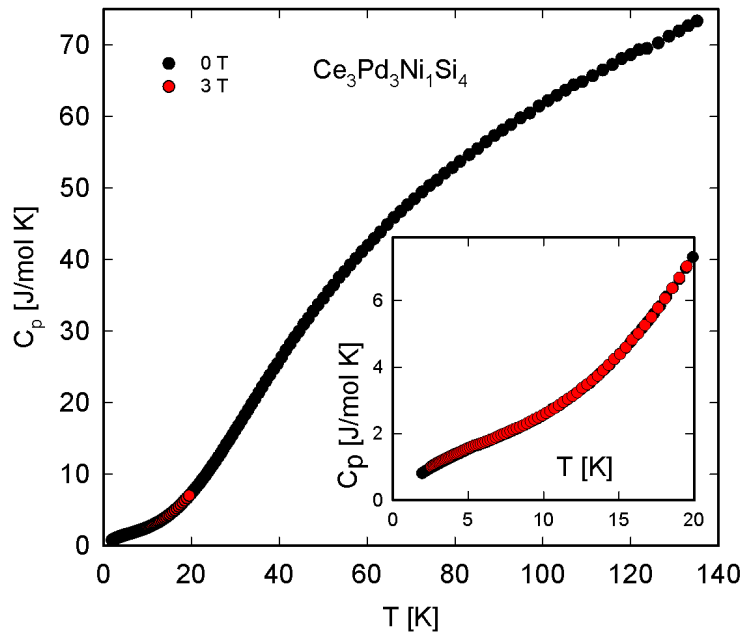


Figure 4.33.: Temperature dependent heat capacity $C_p(T)$ of $Ce_3Pd_3Ni_1Si_4$ in a large temperature range. The inset shows details at low temperatures.

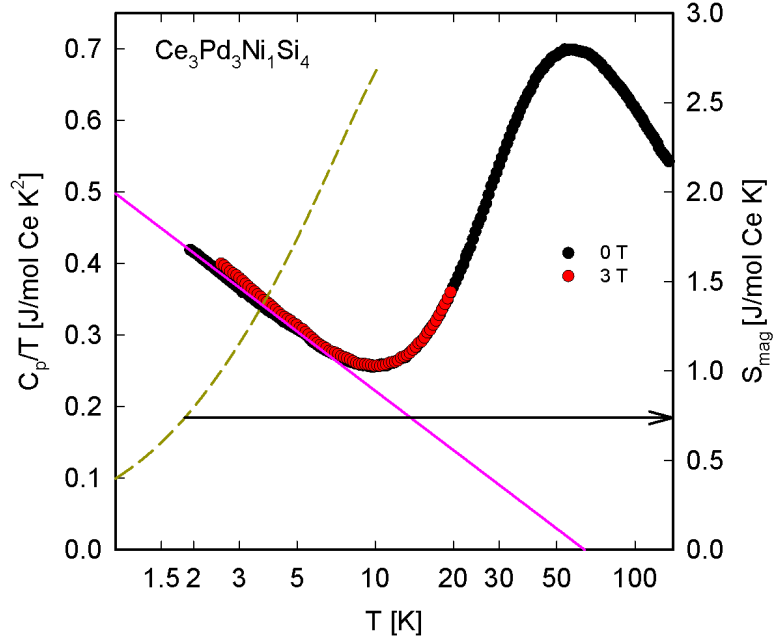


Figure 4.34.: Temperature dependent heat capacity $C_p(T)$ of $Ce_3Pd_3Ni_1Si_4$ plotted as C_p/T vs. T . The solid line represents a least-squares fit of the negative logarithmic part in $C_p(T)/T$, characteristic for non-Fermi-liquids. The dashed line stands for the calculated magnetic entropy.

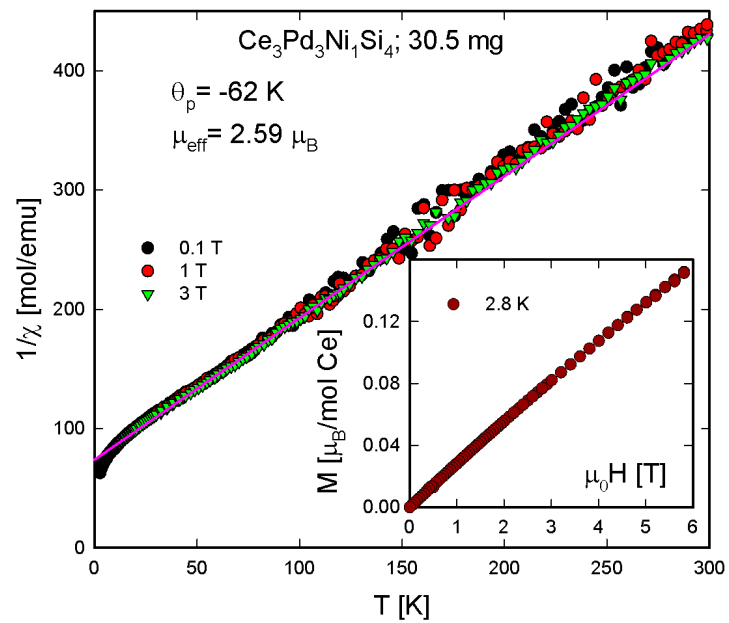


Figure 4.35.: Temperature dependent magnetic susceptibility $\chi(T)$ of $\text{Ce}_3\text{Pd}_3\text{Ni}_1\text{Si}_4$, plotted as $1/\chi$ vs. T . 3 measurements at different external fields (0.1 T, 1 T, 3 T) have been performed. The solid line represents a modified Curie-Weiss fit according to Eqn. (4.2). The inset displays the isothermal magnetisation at 2.8 K. The results are given for 1 cerium atom.

ples: $M = 892.93$ g. Actually, no strong modifications in the physical behaviour compared to $Ce_3Pd_3NiSi_4$ were expected.

Nevertheless, the routine measurement yielded astounding developments. While the maximum of $\rho(T)$ is located in the region of a few kelvin within the Si/Ge series and the $Ce_3Pd_{4-x}Ni_xSi_4$ series up to $x = 1$, here it occurs around 60 K, which is remarkable (Fig. 4.36). Below, resistivity relaxes to a rather low value compared to that of the maximum. In order to check the behaviour, a least-square fit was executed for the lower temperature region, according to the simple power law:

$$\rho(T) = \rho_0 + AT^n \quad (4.3)$$

This is a more general ansatz for looking onto the Fermi-liquid ground state. Taking into account temperatures up to the inflexion point at 25 K yielded for the coefficients the values: $\rho_0 = 237.6 \mu\Omega \text{ cm}$, $A = 0.46$ and finally $n = 1,34$. The exponent is small compared to the usual value $n = 2$ calculated for the Fermi liquid ground state in Kondo lattice systems. Consequently, one can assume the existence of non-Fermi liquid behaviour.

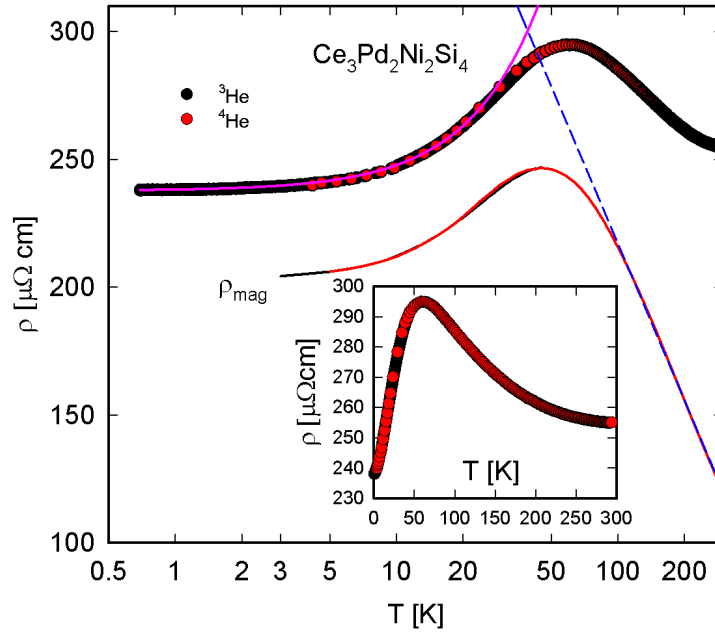


Figure 4.36.: Temperature dependent electrical resistivity of $Ce_3Pd_2Ni_2Si_4$ plotted as $\rho(T)$ vs. $\ln(T)$. Results were obtained from the two devices and fitted together. Moreover, the lower solid line represents the magnetic part of the total resistivity. The inset shows $\rho(T)$ on a linear scale. The pink solid line represents the least squares fit according to (4.3). The blue, dashed line does so in terms of the Kondo logarithmic part.

Moreover, applying magnetic fields only brings small deviations ($< 1\%$) to the curve progression, as illustrated in Figs. 4.37 and 4.38.

At the same time, it came out that magnetoresistivity took a turn from small negative slope to a very small positive one (Fig. 4.39). At 1.5 K and 12 T, only a deviation of 7/10% is obtained.

Measurements of heat capacity yielded ordinary metallic behaviour on the first sight, as shown in Figs. 4.40 and 4.41. From analysis, however, a small magnetic part of specific heat is calculated, which is much smaller than within the other samples. This is illustrated in Fig. 4.41b,

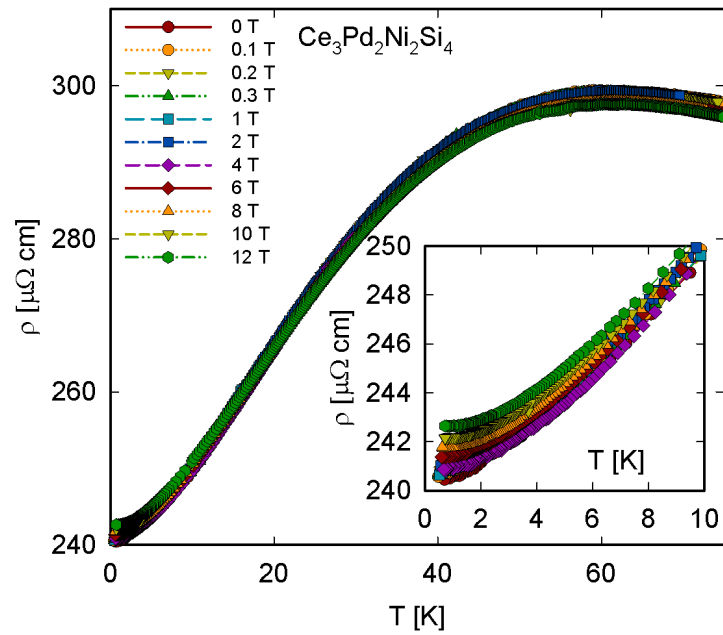


Figure 4.37.: Temperature dependent electrical resistivity $\rho(T, B \neq 0)$ of $\text{Ce}_3\text{Pd}_2\text{Ni}_2\text{Si}_4$ at low temperatures on a linear temperature scale. The inset shows details in the range of 0 K to 10 K.

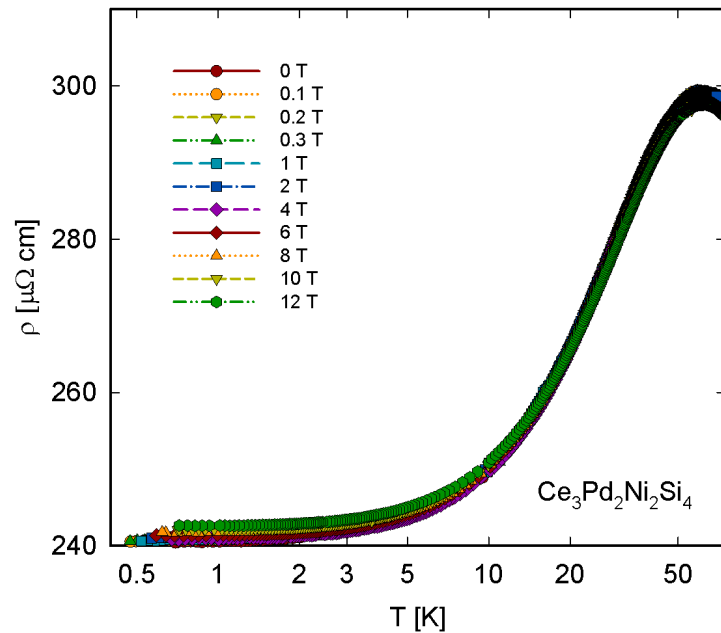


Figure 4.38.: Fig. 4.37 plotted as ρ vs. $\ln(T)$.

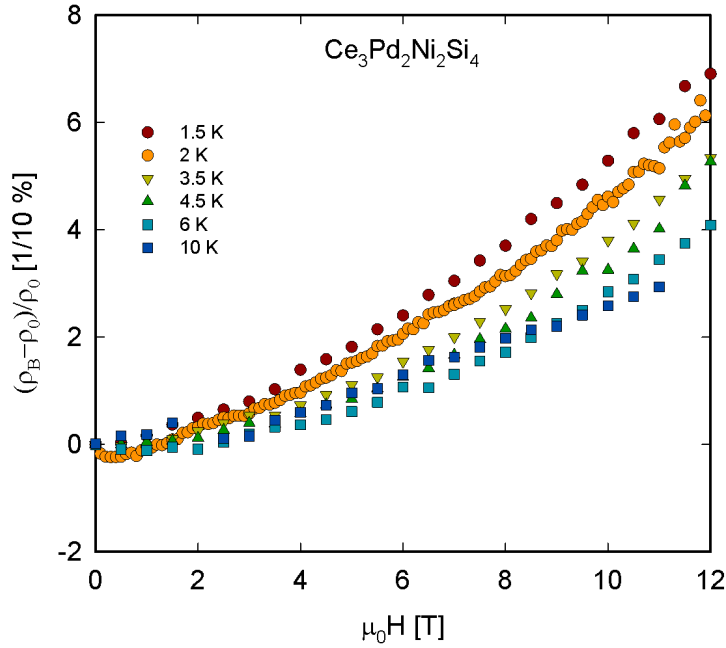


Figure 4.39.: Isothermal magnetoresistivity measurement of $Ce_3Pd_2Ni_2Si_4$ at different temperatures for external magnetic fields in the range of 0 T to 12 T.

where the magnetic entropy is one order of magnitude smaller than with initial $Ce_3Pd_4Si_4$. The small anomaly at about 6 K may be attributed to Ce_2O_3 . From the linear slope below 5 K, one can estimate the Sommerfeld coefficient, representing the electronic contribution, with $\gamma = 130 \text{ mJ/molK}^2$.

Finally, magnetisation measurements were made. The inverse magnetic susceptibility curve shows a smaller slope and higher initial values. This means that the compound's magnetic properties are much weaker compared to those analysed before. Hence, applying a reasonable Curie-Weiss fit emerged to be impossible. Comparing the results with theoretical curves for $\chi(T)/\chi(0)$ and different total angular momentum numbers j , calculated by Rajan [43], ended without success. Rajan used a Bethe ansatz solution for solving the Coqblin-Schrieffer model.

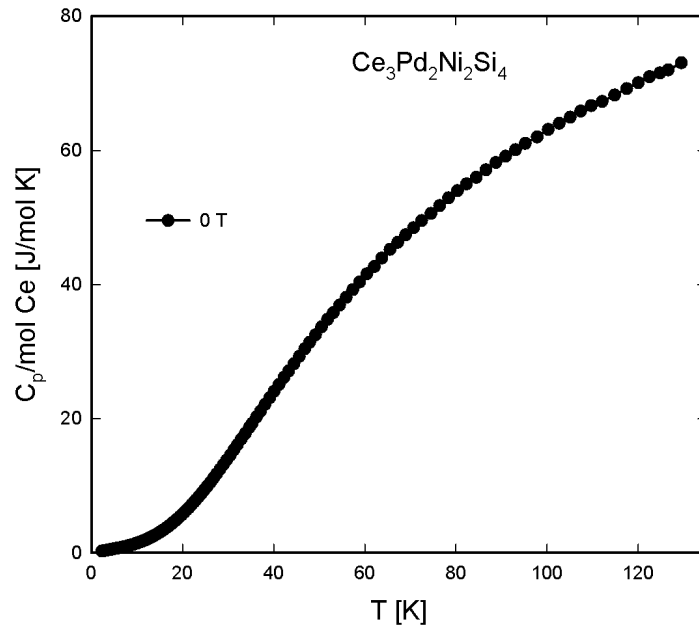
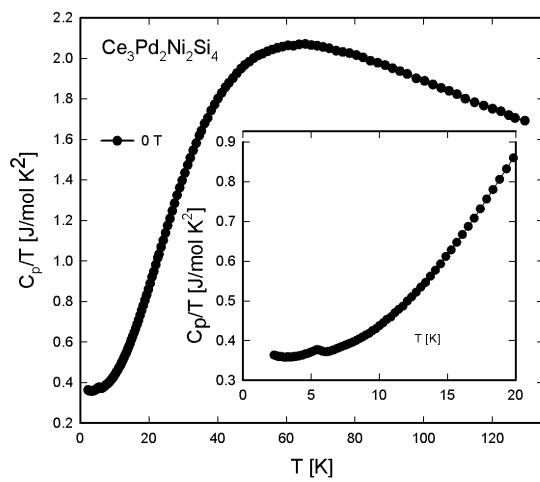
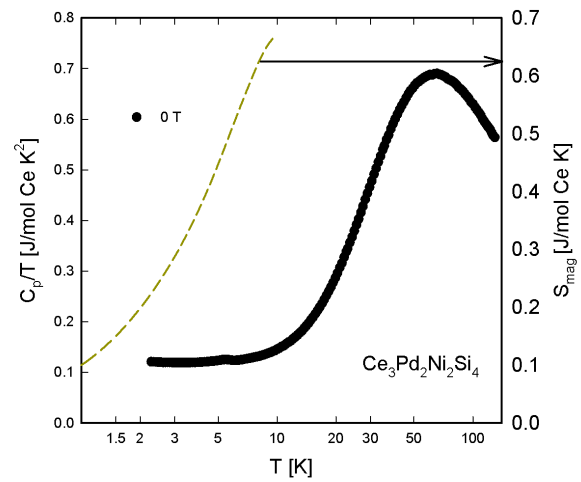


Figure 4.40.: Temperature dependent heat capacity $C_p(T)$ of $\text{Ce}_3\text{Pd}_2\text{Ni}_2\text{Si}_4$, normalised to one mol Ce and plotted using a linear temperature scale.



(a)



(b)

Figure 4.41.: Temperature dependent heat capacity $C_p(T)$ of $\text{Ce}_3\text{Pd}_2\text{Ni}_2\text{Si}_4$, plotted as C_p/T vs. T (Fig.4.41a) and vs. $\ln(T)$ (4.41b). The dashed line in the right picture displays magnetic entropy.

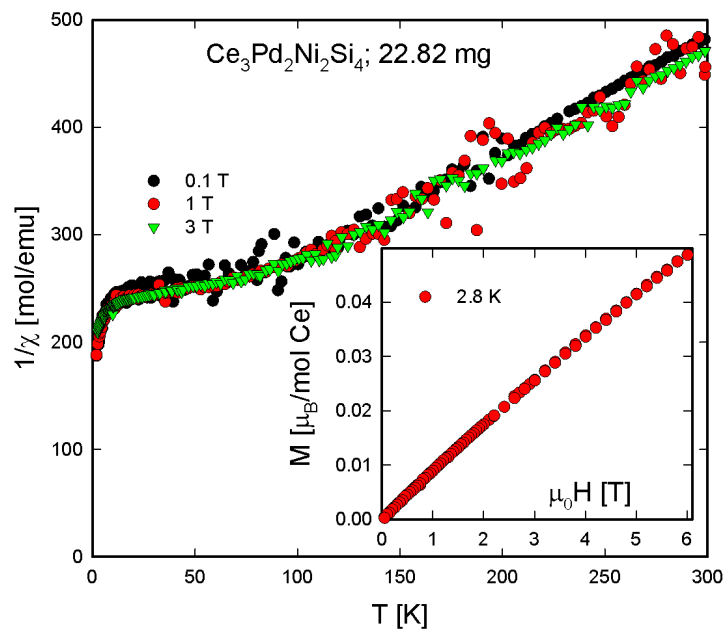


Figure 4.42.: Temperature dependent magnetic susceptibility $\chi(T)$ of $Ce_3Pd_2Ni_2Si_4$, plotted as $1/\chi$ vs. T . Three measurements at different external fields have been executed. As the behaviour of $\chi(T)$ turned out to be different from all of the other explored samples, applying a Curie-Weiss law yielded strange values. The inset of the picture shows the isothermal magnetisation at 2.8 K.

4.3. Overall analysis

The following section should provide information about correlations among the previously discussed samples. For this purpose, comparisons of different properties are made, also of external literature.

At the beginning, it's a good idea to have a look at X-ray diffractometry data for an improved discussion. Therefore, a comparison of lattice parameters is given for all samples in Fig. 4.43. It clearly states that the boundary component $\text{Ce}_3\text{Pd}_4\text{Si}_4$ represents the maximum, as respects lattice parameter a . Moving towards higher substitution rates diminishes the the cell volume $V = a \cdot b \cdot c$ in case of the Pd/Ni substitution, while an increase of the cell volume is observed with the Si/Ge substitution.

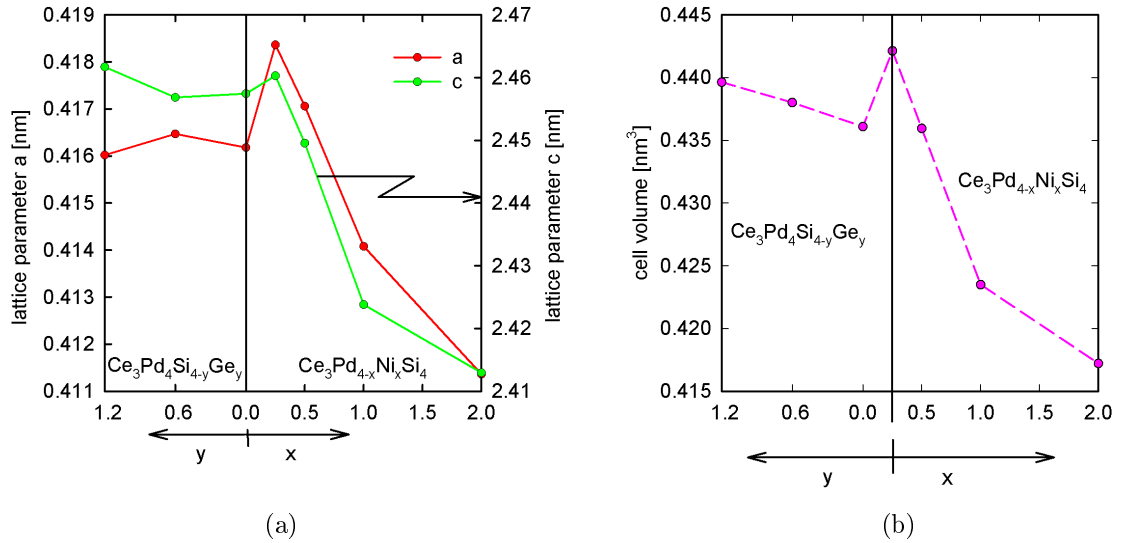


Figure 4.43.: Comparative depiction of lattice parameters (a) and unit cell volume (b) of $\text{Ce}_3\text{Pd}_{4-x}\text{Ni}_x\text{Si}_{4-y}\text{Ge}_y$. The vertical solid line represents the initial component $\text{Ce}_3\text{Pd}_4\text{Si}_4$. Left of it, the germanium samples are dealt with, while on the right side there the picture deals with the nickel substitution series. The cell volume increases for the Si/Ge substitution and decreases when substituting Pd by Ni.

From the results seen in Fig. 4.43, as well as in Fig. 4.17 in Tab. 4.2, one can deduce a significant decrease of the unit cell volume towards higher nickel substitution rates. It amounts to 4.3 % from the lowest to the highest considered substitution rate, i.e. $x = 2$. Thus, one can assume a high rate of chemical pressure acting on the compound and influencing its properties. An approximative calculation of chemical pressure generated can be done using the Murnaghan equation of state:

$$p(V) = \frac{K}{K'} \left[\left(\frac{V}{V_0} \right)^{-K'} - 1 \right]. \quad (4.4)$$

The quantity K is the bulk modulus of the alloy dealt with and K' corresponds to its first derivative with respect to pressure. As respects the cerium compounds, a bulk modulus of 1000 kbar was assumed, with K' being 5. These are common values of intermetallic compounds, suggested by E. Bauer according to his long research experience. Inserting $K = 1000$ kbar and $K' = 5$ yields a chemical pressure of nearly 50 kbar. This value is approximately 2.5 times as high as the highest applicable pressure in the Institute's pressure cell. Chemical substitution and externally

applied pressure result in similar modifications of physical properties, as long as substitution does not severely modify the electronic structure of the system.

Fig. 4.44 is taken from the publication by Kneidinger et al. [1]. Having a closer look on those two 3 – 4 – 4 compounds awoke interest in studying modifications of magnetic and transport properties when substituting one component by another in many directions. Initially, the series Ce-La was investigated by substituting cerium with lanthanum in [32]. After that, first attempts to substitute silicon with germanium, i.e. the semi-metal part, were made in [40] and are continued in this work. Long range magnetic order at low temperatures was found already for small substitution rates of one nonmagnetic element by another. Initial $\text{Ce}_3\text{Pd}_4\text{Si}_4$ didn't show any magnetically ordered groundstate.

The next issue on the list, which brought disproportional more new information, was to substitute the transition metal palladium by nickel, also as a part of this work. Further substitution ratios are planned. Moreover, several new substitution ideas have come up, e.g. substituting palladium by silver, cerium by ytterbium, palladium by copper etc.

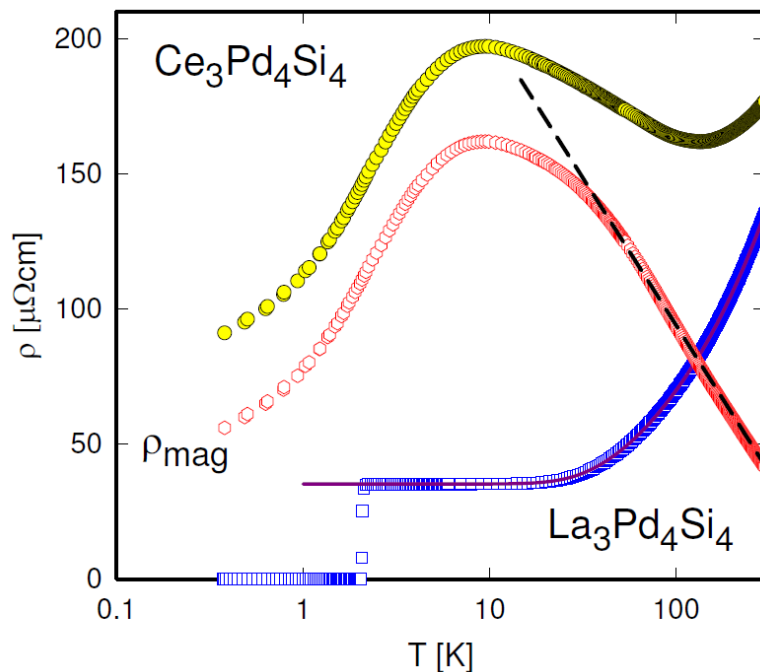


Figure 4.44.: Temperature dependent resistivity ρ of $\text{La}_3\text{Pd}_4\text{Si}_4$ and $\text{Ce}_3\text{Pd}_4\text{Si}_4$ plotted on a logarithmic temperature scale. The magnetic contribution $\rho_{mag}(T)$ of $\text{Ce}_3\text{Pd}_4\text{Si}_4$ is also shown in this plot, where the dashed line should emphasize Kondo interaction. [1]

The following figures (Fig. 4.45) were made to clarify the shifting of resistivity curves, at first only for the samples of the Ni series.

Fig. 4.46 and Fig. 4.47 present the overall temperature dependent resistivity $\rho(T)$. It is hard to compare quantitative results for each compound. This is due to measurement uncertainty and also uncertainties when preparing the samples (errors in the sample dimensions etc.). Sure enough, the most interesting part of the measurement is the qualitative behaviour. That's why e.g. resistivity is often plotted as $\rho(T)/\rho(300\text{K})$, the ratio of resistivity and resistivity at room temperature. In doing so, one can assure that every measurement curve has its upper start at the same point and only qualitative changes are visible. This is done here yielding interesting

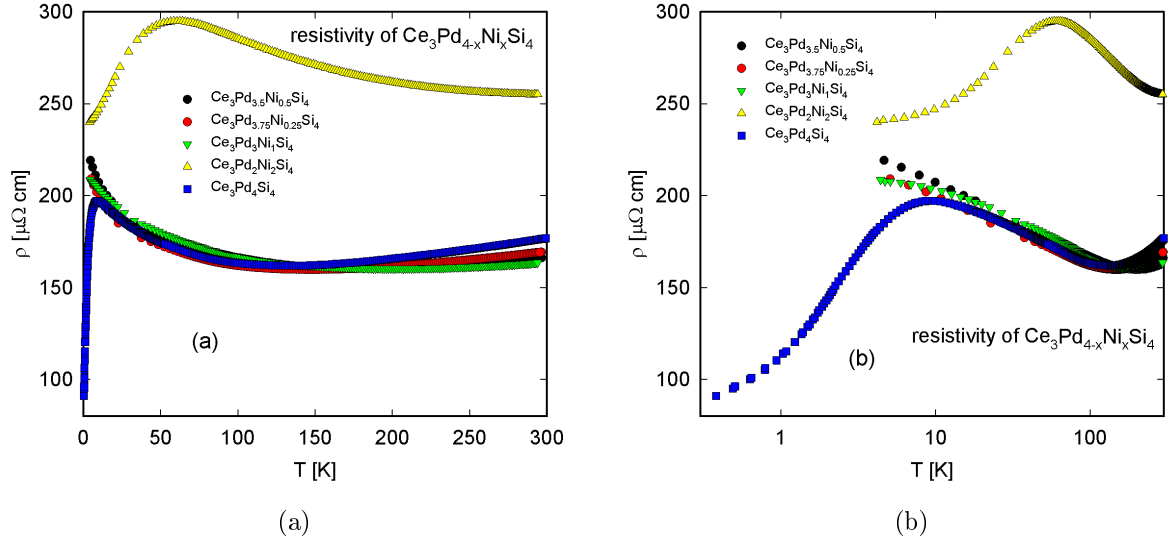


Figure 4.45.: Temperature dependent resistivity $\rho(T)$ of $\text{Ce}_3\text{Pd}_{4-x}\text{Ni}_x\text{Si}_4$, plotted over a linear (a) and logarithmic (b) temperature scale.

results especially in Fig. 4.47, where the slope of Kondo behaviour in the logarithmic diagram changes in line with the substitution rate. The higher the Germanium substitution rate is, the lower is the slope. On the other hand, the slope is proportional to the nickel substitution rate. In order to quantify this behaviour, a fit of the logarithmic part in the graphs was done using a simple law:

$$\rho(T) = \rho_0 + A \cdot \ln(T) \quad (4.5)$$

For a better visibility, dashed lines correspond to the fitting results.

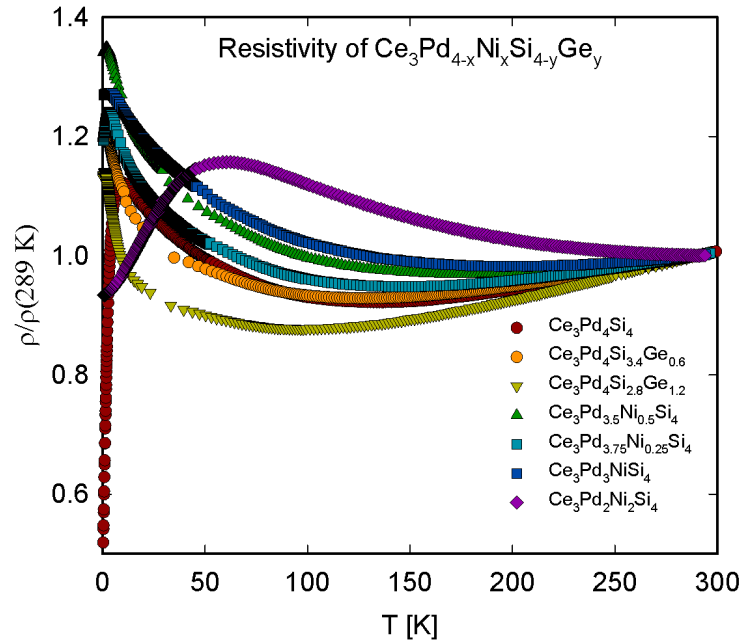


Figure 4.46.: Temperature dependent resistivity of all probed alloys.

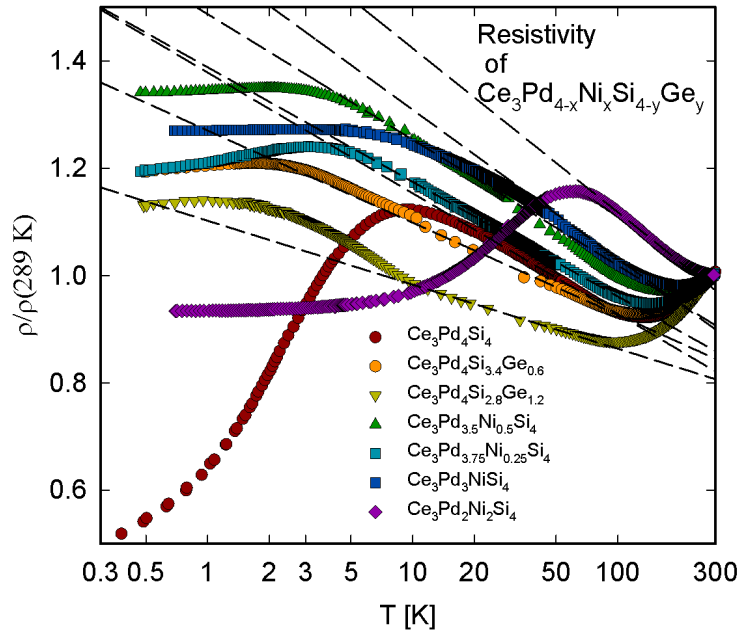


Figure 4.47.: Temperature dependent resistivity of all analysed samples plotted over a logarithmic temperature scale. The dashed lines represent a least-squares fit according to equation (4.5).

Furthermore, for reasons of comparison, $C_p(T, B = 0)$ of all samples is shown in Fig. 4.48. The physical behaviour is revealed more clearly in a C_p/T vs. T diagram like seen in Fig. 4.49. While at temperatures down to 10 K, few differences are visible, the low temperature development is distinct. Trends show a strong augmentation of C_p/T for the germanium substitution in the region, where magnetic ordering takes place. Going from less germanium to more nickel yields a continuing decrease of the slope. In $\text{Ce}_3\text{Pd}_2\text{Ni}_2\text{Si}_4$, there is no increase below 10 K at all, at least in the measurement range covered. Observing lower temperature behaviour for this compound will be necessary for further analyses.

Another interesting aspect is to explore the development of the magnetic entropy as a function of the composition. This was done for two temperatures in Fig. 4.50. Especially for the nickel compounds, a distinct trend, which can nearly be interpreted as a linear decrease, appears.

For reasons of finding connections between the magnetic properties of the samples analysed, Fig. 4.51 reveals the development of the paramagnetic Curie temperature as well as of the effective magnetic moment of $\text{Ce}_3\text{Pd}_{4-x}\text{Ni}_x\text{Si}_{4-y}\text{Ge}_y$. θ_p shows a definite tendency to drop towards higher nickel substitution rates. If one considers the value for $\text{Ce}_3\text{Pd}_{3.5}\text{Ni}_{0.5}\text{Si}_4$ to be an outlier, a positive slope is observable for the effective magnetic moment. Nevertheless, further compounds with higher nickel substitution rates should be prepared to clarify these tendencies.

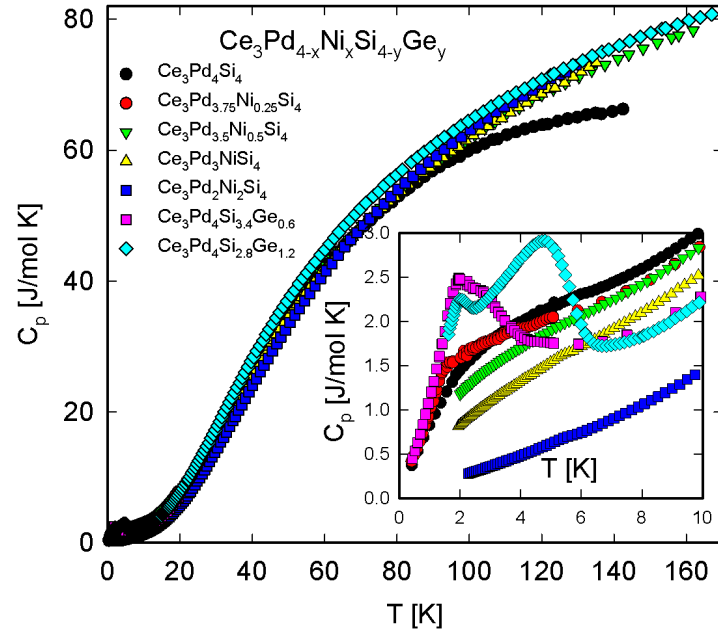


Figure 4.48.: Temperature dependent heat capacity $C_p(T)$ of $\text{Ce}_3\text{Pd}_{4-x}\text{Ni}_x\text{Si}_{4-y}\text{Ge}_y$ as an overall comparison. The high temperature behaviour coincides pretty much, while in the thrilling low-temperature region, strong deviations occur, especially in terms of possible transitions. For this reason, an magnification is plotted in the inset.

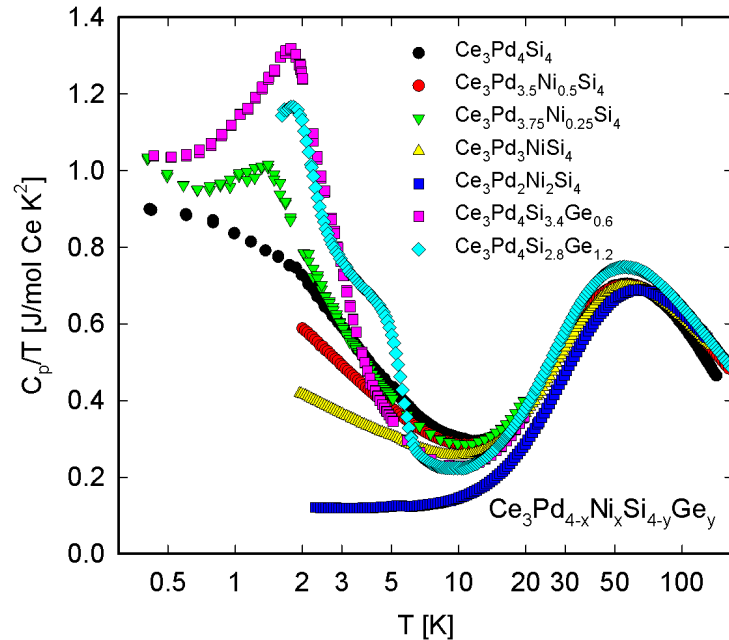


Figure 4.49.: Temperature dependent heat capacity $C_p(T)$ of $\text{Ce}_3\text{Pd}_{4-x}\text{Ni}_x\text{Si}_{4-y}\text{Ge}_y$ plotted over a logarithmic T scale.

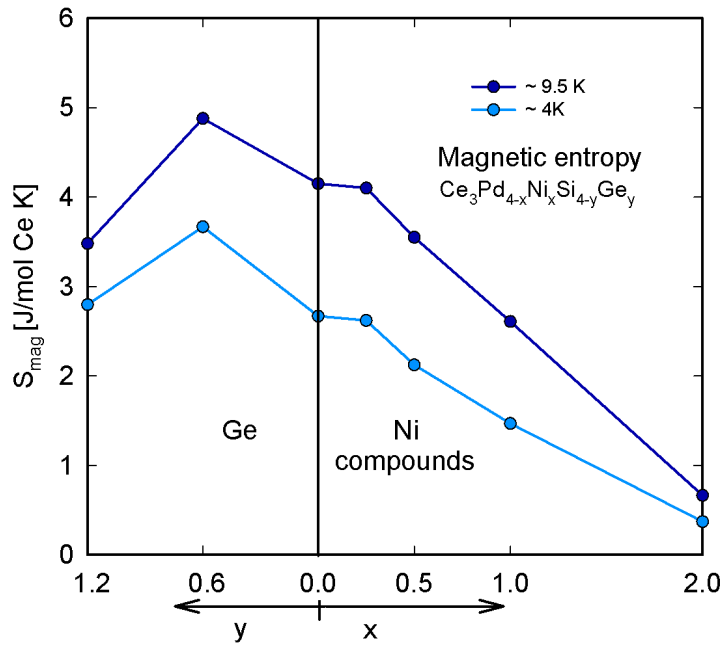


Figure 4.50.: Magnetic entropy at different temperatures plotted over the substitution rate.

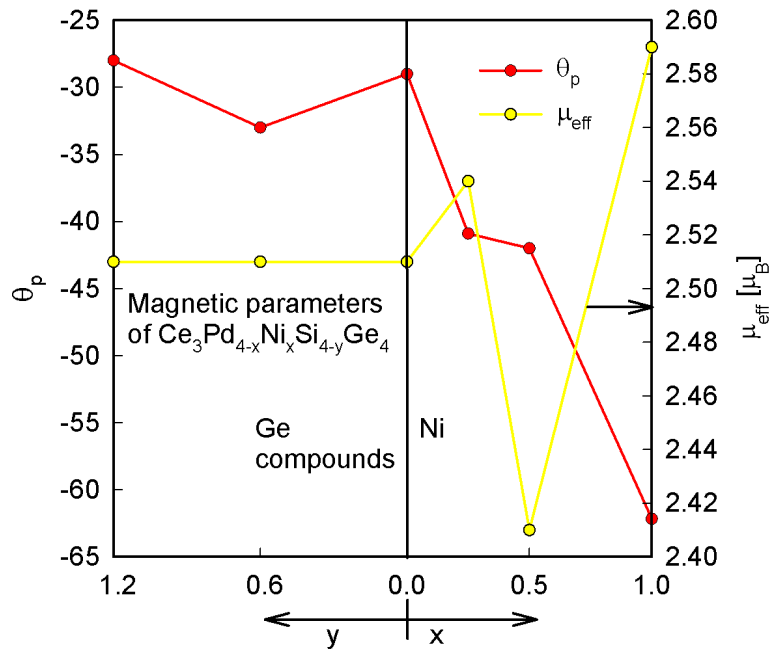


Figure 4.51.: Magnetic properties of $\text{Ce}_3\text{Pd}_{4-x}\text{Ni}_x\text{Si}_{4-y}\text{Ge}_y$ plotted versus the composition. The vertical line separates the substitution series and represents the initial compound $\text{Ce}_3\text{Pd}_4\text{Si}_4$.

4.4. Outlook

As it was already mentioned before, a significant interest in this kind of cerium 3 – 4 – 4 compounds arose after analysing the results. This gave rise to encourage the study of further substitution series, e.g. Pd – Ag and Pd – Cu. Nevertheless, the most interesting part was to take a more detailed look onto the nickel substitution by producing more compositions, including $\text{Ce}_3\text{Ni}_4\text{Si}_4$. This was already done by Khan Sirak [44] during a “Projektarbeit” at IFP of the TU Wien. Consequently, a short outlook onto further research shall be presented here by disclosing some measurement results.

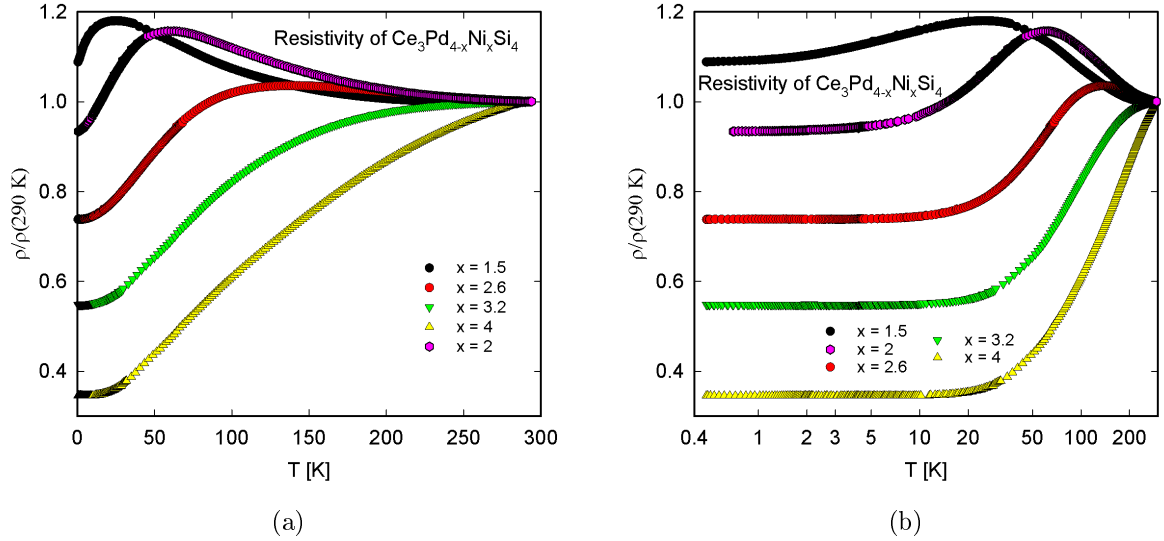


Figure 4.52.: Temperature dependent resistivity $\rho(T)$ of further $\text{Ce}_3\text{Pd}_{4-x}\text{Ni}_x\text{Si}_4$ compounds, plotted over a linear (4.52a) and logarithmic (4.52b) temperature scale including the boundary sample $\text{Ce}_3\text{Ni}_4\text{Si}_4$. High substitution rates cause a total vanishing of magnetic scattering and Kondo properties.

Fig. 4.52 exhibit interesting physical behaviour. Surpassing the highest nickel substitution rate of the author yields a continuous attenuation of magnetic properties. The Kondo effect vanishes, magnetic susceptibility drops to very small values. Substitution of a nonmagnetic material leads to a total extinction of magnetic properties. Further analysis is advised, e.g. by comparing the results with those of nonmagnetic $\text{La}_3\text{Ni}_4\text{Si}_4$.

5. Summary

Six specimen of the ternary system $\text{Ce}_3\text{T}_4\text{X}_4$ have be examined in terms of their electrical resistivity, heat capacity and magnetic susceptibility. The samples formed part of two substitution series, starting from the initial compound $\text{Ce}_3\text{Pd}_4\text{Si}_4$, previously investigated in Ref. [1]. Transition metal palladium was substituted by nickel and silicon by germanium. Only samples which exhibited high quality in x-ray diffraction analyses were looked upon as expedient. The members of the germanium substitution series all showed Kondo lattice behaviour and a transition into an antiferromagnetic ground state below a certain temperature. The latter was an unexpected finding, as the initial compound didn't exhibit this kind of behaviour. Furthermore, a twofold logarithmic temperature dependence of ρ_{mag} was discovered, yielding Kondo interaction in the presence of crystalline electric field splitting. Analyses of transport properties and heat capacity measurements showed clear signs for non-Fermi-liquid behaviour. External magnetic fields suppress the antiferromagnetic ground state and induce a ferromagnetic ordering of the magnetic moments.

Substituting palladium by nickel yields a creeping decrease of the magnitude of magnetic properties. While lower substitution rates exhibit a Kondo lattice behaviour with a maximum in $\rho(T)$ at approximately 5 K and a pronounced magnetic phase transition in case of $\text{Ce}_3\text{Pd}_{3.75}\text{Ni}_{0.25}\text{Si}_4$, a strong transformation occurs in between the compositions $\text{Ce}_3\text{Pd}_3\text{NiSi}_4$ and $\text{Ce}_3\text{Pd}_2\text{Ni}_2\text{Si}_4$ with the maximum shifting from a few kelvin to 60 K. Simultaneously, the magnetic entropy as well as the magnetoresistivity drops by one order of magnitude, while Curie-Weiss behaviour can't be attributed to measurements anymore. Heat capacity measurements show a maximum at the same temperature as the electrical resistivity.

Those interesting developments can probably be attributed to a shrinking of the unit cell volume by 4 %, which yields increased chemical pressure of approximately 50 kbar.

In summary, two interesting phenomena have been detected: Firstly, the occurrence of a transition into an antiferromagnetic groundstate due to RKKY-interactions, which wasn't observed for the initial ternary system without substitutions. Secondly, a diminishment of magnetic properties was observed, when substituting a non-magnetic element by another.

Bibliography

- [1] F. Kneidinger, H. Michor, E. Bauer, A. Griбанov, A. Lipatov, Y. Seropegin, J. Sereni, and P. Rogl. Superconductivity and non-Fermi-liquid behavior of $\text{La}_3\text{Pd}_4\text{Si}_4$ and $\text{Ce}_3\text{Pd}_4\text{Si}_4$. *Phys. Rev. B*, 88:024423, Jul 2013. URL: <http://link.aps.org/doi/10.1103/PhysRevB.88.024423>, doi:10.1103/PhysRevB.88.024423.
- [2] G. Hilscher, H. Michor, M. Reissner, and S. Bühler-Paschen. Festkörperphysik I. Vorlesungsskriptum TU Wien, 2011-2013.
- [3] E. Bauer and S. Bühler-Paschen. Strongly Correlated Electron Systems. Vorlesungsskriptum TU Wien, 2013.
- [4] P. Drude. Zur Elektronentheorie der Metalle. *Annalen der Physik*, 306:566–613, 1900. doi:10.1002/andp.19003060312.
- [5] P. Drude. Zur Elektronentheorie der Metalle; II. Teil. Galvanomagnetische und thermomagnetische Effecte. *Annalen der Physik*, 308:369–402, 1900. doi:10.1002/andp.19003081102.
- [6] E. Bauer, C. Eisenmenger-Sittner, and J. Fidler. Materialwissenschaften. Vorlesungsskriptum TU Wien, 2014.
- [7] E. Bauer. Kondo Systems and Heavy Fermions: Transport Phenomena. *Encyclopedia of Materials: Science and Technology*, pages 4372–4381, 2001.
- [8] R.T. Khan. *Pressure and field response of strongly correlated electron systems*. PhD thesis, Vienna University of Technology, 2010.
- [9] P. Coleman. Heavy Fermions: electrons at the edge of magnetism. *eprint arXiv:cond-mat/0612006*, November 2006. arXiv:cond-mat/0612006.
- [10] P. W. Anderson. Localized magnetic states in metals. *Phys. Rev.*, 124:41–53, Oct 1961. URL: <http://link.aps.org/doi/10.1103/PhysRev.124.41>, doi:10.1103/PhysRev.124.41.
- [11] B. Coqblin and J. R. Schrieffer. Exchange interaction in alloys with cerium impurities. *Phys. Rev.*, 185:847–853, Sep 1969. URL: <http://link.aps.org/doi/10.1103/PhysRev.185.847>, doi:10.1103/PhysRev.185.847.
- [12] B. Cornut and B. Coqblin. Influence of the crystalline field on the Kondo effect of alloys and compounds with cerium impurities. *Phys. Rev. B*, 5:4541–4561, Jun 1972. URL: <http://link.aps.org/doi/10.1103/PhysRevB.5.4541>, doi:10.1103/PhysRevB.5.4541.
- [13] Ernst Bauer. Anomalous properties of Ce-Cu- and Yb-Cu-based compounds. *Advances in Physics*, 40(4):417–534, 1991. URL: <http://dx.doi.org/10.1080/00018739100101512>, arXiv:<http://dx.doi.org/10.1080/00018739100101512>, doi:10.1080/00018739100101512.
- [14] C. Gold. *Über die Natur konkurrierender Wechselwirkungen in Cer-basierten 1-9-4 Verbindungen*. PhD thesis, Augsburg University, 2013.

- [15] S. Doniach. The Kondo lattice and weak antiferromagnetism. *Physica B+C*, 91(0):231 – 234, 1977. URL: <http://www.sciencedirect.com/science/article/pii/0378436377901905>, doi:[http://dx.doi.org/10.1016/0378-4363\(77\)90190-5](http://dx.doi.org/10.1016/0378-4363(77)90190-5).
- [16] M. A. Ruderman and C. Kittel. Indirect exchange coupling of nuclear magnetic moments by conduction electrons. *Phys. Rev.*, 96:99–102, Oct 1954. URL: <http://link.aps.org/doi/10.1103/PhysRev.96.99>, doi:10.1103/PhysRev.96.99.
- [17] Tadao Kasuya. A theory of metallic ferro- and antiferromagnetism on Zener’s model. *Progress of Theoretical Physics*, 16(1):45–57, 1956. doi:10.1143/PTP.16.45.
- [18] Kei Yosida. Magnetic properties of Cu-Mn alloys. *Phys. Rev.*, 106:893–898, Jun 1957. URL: <http://link.aps.org/doi/10.1103/PhysRev.106.893>, doi:10.1103/PhysRev.106.893.
- [19] A. Rosch. Disorder effects on transport near AFM quantum phase transitions. *Physica B Condensed Matter*, 280:341–346, May 2000. arXiv:cond-mat/9908245, doi:10.1016/S0921-4526(99)01730-5.
- [20] S. Bühler-Paschen and P. Mohn. Festkörperphysik II. Vorlesungsskriptum TU Wien, 2013.
- [21] A. Lipatov, A. Griбанov, A. Grytsiv, P. Rogl, E. Murashova, Y. Seropegin, G. Giester, and K. Kalmykov. The ternary system cerium-palladium-silicon. *Journal of Solid State Chemistry*, 2009.
- [22] J. Brentano. Focussing method of crystal powder analysis by X-rays. *Proceedings of the Physical Society of London*, 37(1):184, 1924. URL: <http://stacks.iop.org/1478-7814/37/i=1/a=326>.
- [23] Siemens Aktiengesellschaft. D5000 X-ray diffractometer operation manual. <http://ameri.fiu.edu/Backup/members/D5000%20Manual.pdf>, 1989.
- [24] Yu.D. Seropegin, A.V. Griбанov, and O.I. Bodak. Isothermal cross-section of the Ce–Pd–Ge phase diagram at 600°C. *Journal of Alloys and Compounds*, 269(1-2):157 – 161, 1998. URL: <http://www.sciencedirect.com/science/article/pii/S0925838898002473>, doi:[http://dx.doi.org/10.1016/S0925-8388\(98\)00247-3](http://dx.doi.org/10.1016/S0925-8388(98)00247-3).
- [25] F. Kneidinger. *Non-centrosymmetric superconductivity of intermetallic compounds in absence of strong correlations among electrons*. PhD thesis, Vienna University of Technology, 2014.
- [26] D. E. Tsatis. Thermal diffusivity of ge 7031 varnish. *Journal of Applied Physics*, 62(1):302, 1987. URL: <http://scitation.aip.org/content/aip/journal/jap/62/1/10.1063/1.339146>, doi:<http://dx.doi.org/10.1063/1.339146>.
- [27] Inc. Precision Cryogenic Systems. <http://www.precisioncryo.com/dewarvapo.html>.
- [28] L. Spindelhofer and B. Dangl. Tieftemperaturmesskopf (Luber). Projektarbeit TU Wien, 2010.
- [29] Cryogenic. ³He Insert and Superconducting Magnet System. Device Manual.
- [30] M. Doktor. Magnetowiderstand und Druckabhängigkeit von YbCu₄(AuAg). Master’s thesis, Vienna University of Technology, 1996.
- [31] S. Löffler. SQUID Magnetometrie. Projektarbeit TU Wien, 2006.

- [32] K. Sirak. Quantenkritikalität in $(\text{Ce}_x\text{La}_{1-x})_3\text{Pd}_4\text{Si}_4$. Bachelor's thesis, Vienna University of Technology, 2013.
- [33] Herwig Michor and Peter Mohn. Magnetische Messmethoden. Vorlesungsskriptum TU Wien, 2014.
- [34] R. C. Jaklevic, John Lambe, A. H. Silver, and J. E. Mercereau. Quantum interference effects in Josephson tunneling. *Phys. Rev. Lett.*, 12:159–160, Feb 1964. URL: <http://link.aps.org/doi/10.1103/PhysRevLett.12.159>, doi:10.1103/PhysRevLett.12.159.
- [35] B.D. Josephson. Possible new effects in superconductive tunnelling. *Physics Letters*, 1(7):251 – 253, 1962. URL: <http://www.sciencedirect.com/science/article/pii/0031916362913690>, doi:[http://dx.doi.org/10.1016/0031-9163\(62\)91369-0](http://dx.doi.org/10.1016/0031-9163(62)91369-0).
- [36] Quantum Design. Physical properties measurement system: Heat capacity option user's manual. http://www.mrl.ucsb.edu/sites/default/files/mrl_docs/instruments/hcapPPMS.pdf.
- [37] W. Nernst, 1910. Sitzungsber. K. Preuss. Akad. Wiss. 12, 261.
- [38] G. Schaudy. *Kalorimetrie in hohen Magnetfeldern*. PhD thesis, Vienna University of Technology, 1995.
- [39] C. Schmitzer, 1985. Dissertation, TU Wien.
- [40] I. Topic. Search for quantum critical behaviour in cerium 3:4:4 systems. Master's thesis, Vienna University of Technology, 2013.
- [41] I. Das and E. V. Sampathkumaran. Magnetism and Kondo effect in $\text{CePd}_2\text{Si}_{2-x}\text{Ge}_x$. *Phys. Rev. B*, 44:9711–9714, Nov 1991. URL: <http://link.aps.org/doi/10.1103/PhysRevB.44.9711>, doi:10.1103/PhysRevB.44.9711.
- [42] H.J. Im, Y.S. Kwon, and M.H. Jung. Electrical and magnetic properties of the new Kondo-lattice compound $\text{Ce}_3\text{Pd}_4\text{Ge}_4$. *Solid State Communications*, 2002.
- [43] V. T. Rajan. Magnetic susceptibility and specific heat of the Coqblin-Schrieffer model. *Phys. Rev. Lett.*, 51:308–311, Jul 1983. URL: <http://link.aps.org/doi/10.1103/PhysRevLett.51.308>, doi:10.1103/PhysRevLett.51.308.
- [44] K. Sirak. Quantenkritikalität in Nickel substituierten $\text{Ce}_3(\text{Pd}_x\text{Ni}_{1-x})_4\text{Si}_4$. Projektarbeit, Vienna University of Technology, 2014.

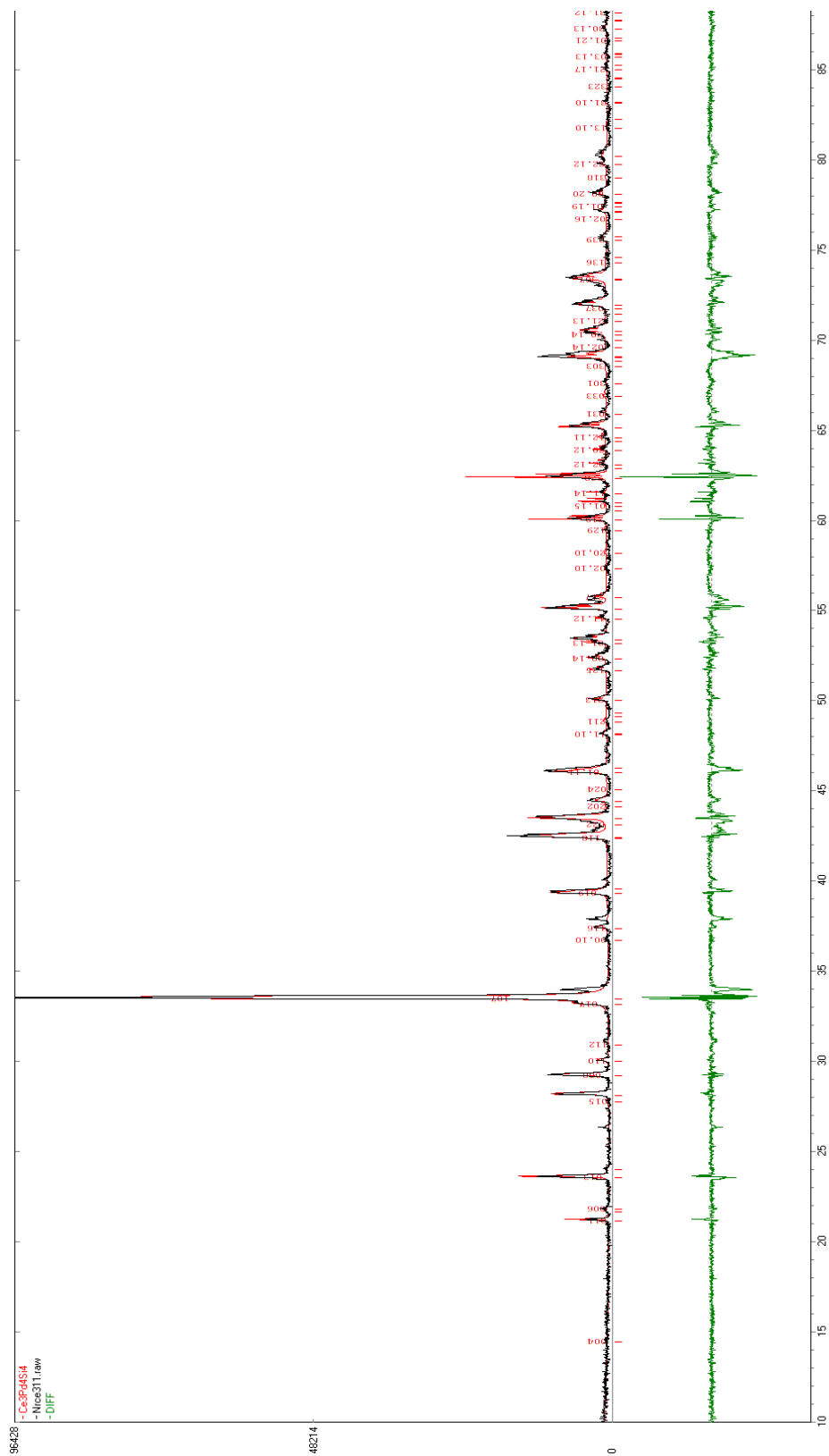
List of Tables

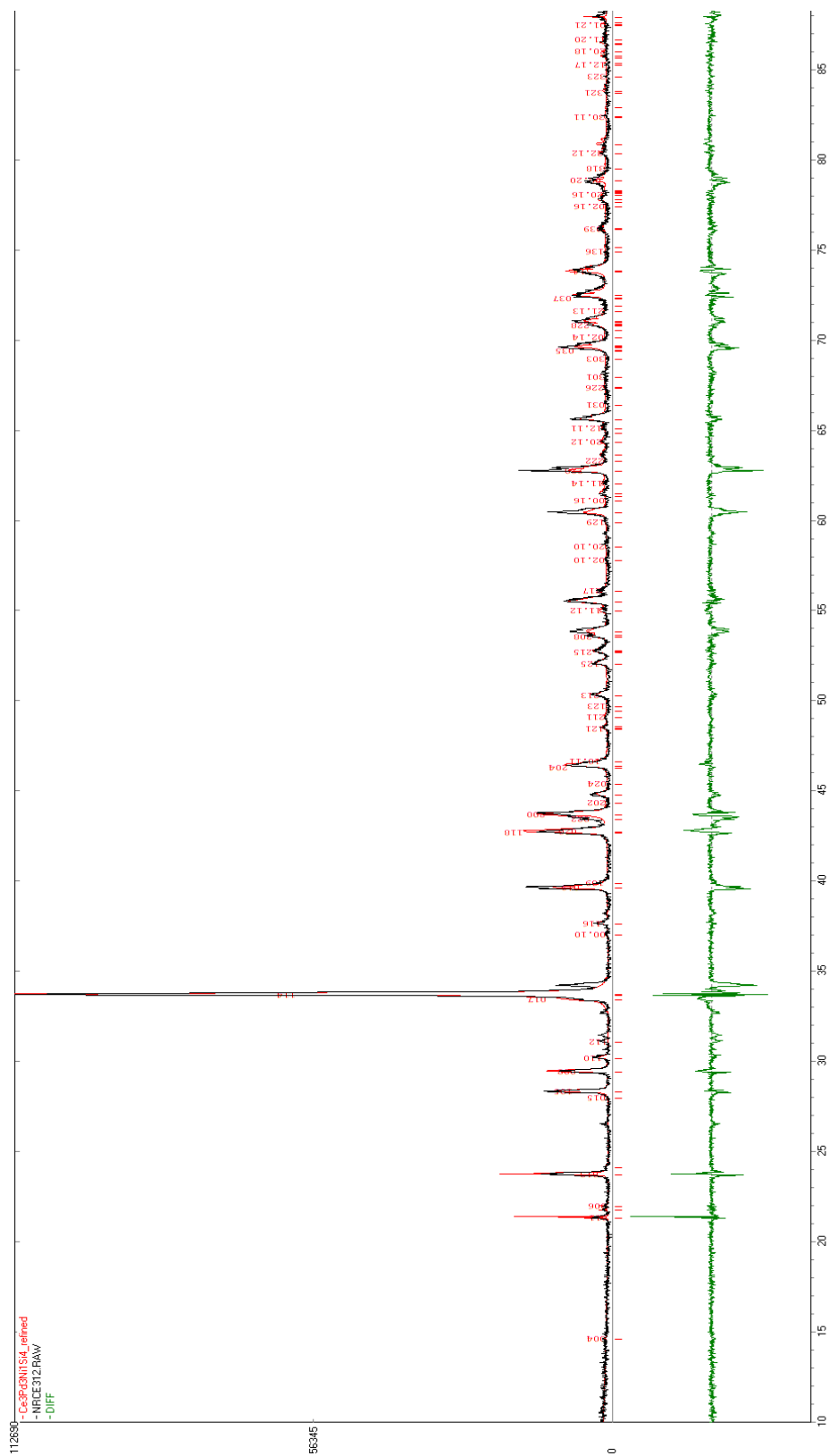
2.1.	13
4.1. Lattice parameters of sample $Ce_3Pd_4Si_{3.4}Ge_{0.6}$ and $Ce_3Pd_4Si_{2.8}Ge_{1.2}$	37
4.2. Lattice parameters of samples 3 to 6	48

B. X-ray diffraction patterns

This section discusses the analyses of the X-ray diffraction patterns, executed with the computer programme *PowderCell V. 2.4*.

The following five figures exhibit the diffraction patterns of $\text{Ce}_3\text{Pd}_4\text{Si}_{2.8}\text{Ge}_{1.2}$ and the four nickel-based samples. The analysis procedure starts with creating the theoretical composition of the unit cell. This is done by opening a new file. The important parameters, obtainable from literature, if existent, are the space group (or the space group number) and the lattice parameters. Furthermore, the atomic positions have to be entered for each element. When clicking onto the *OK*-button, the structure is constructed. In the *Diffraction* menu bar, it is firstly necessary to define the X-ray source and other parameters like the used geometry. This is done by clicking onto the *Experiment* button and subsequent modifying of the parameters in the pop-up window. After having done so, one can click onto the *Diffraction ON* button, thus the programme calculates the theoretical powder pattern and shows it in a separate window. Now, it is possible to load the measured powder pattern by clicking onto *Load powder pattern* in the *Diffraction* menu. Measured and calculated patterns are now placed on top of each other represented by counts versus angle $2\cdot\theta$. The measured pattern is black, while the first calculated pattern is red. Below the origin of the ordinate, the theoretical peaks are marked by red vertical dashes and further below the calculated difference between measured and theoretical data in a green line. For adapting theoretical parameters to the measured data, one needs to do a refinement procedure. This can be done either by hand by modifying the initial lattice parameters (*Structure* \rightarrow *Edit initial data*) or by automatical Rietveld refinement. The latter is done by clicking onto *Parameters* in the *Refinement* menu. In the tab *General*, one can choose the degree of the polynom for the fitting procedure of the background as well as the number of iterations. The check marks in the windows state, which quantities will be modified. This has also to be checked in the *lattice/profile* tab. By clicking onto *Start*, the refinement begins. Note here that derivations of theoretical and experimental powder pattern have to be small with the standard settings. If everything works out, the theoretical pattern is shifted in direction of the experimental one. Refined lattice parameters can be read in the *results* tab. It is also possible to export the theoretical pattern or the difference as data points by clicking onto the right mouse button and *export*. Impurity phases can be considered either by excluding some regions from the refinement or additionally by loading one or more impurity structures.

Figure B.2.: X-ray diffraction pattern of $\text{Ce}_3\text{Pd}_{3.75}\text{Ni}_{0.25}\text{Si}_4$.

Figure B.4.: X-ray diffraction pattern of $\text{Ce}_3\text{Pd}_3\text{NiSi}_4$.

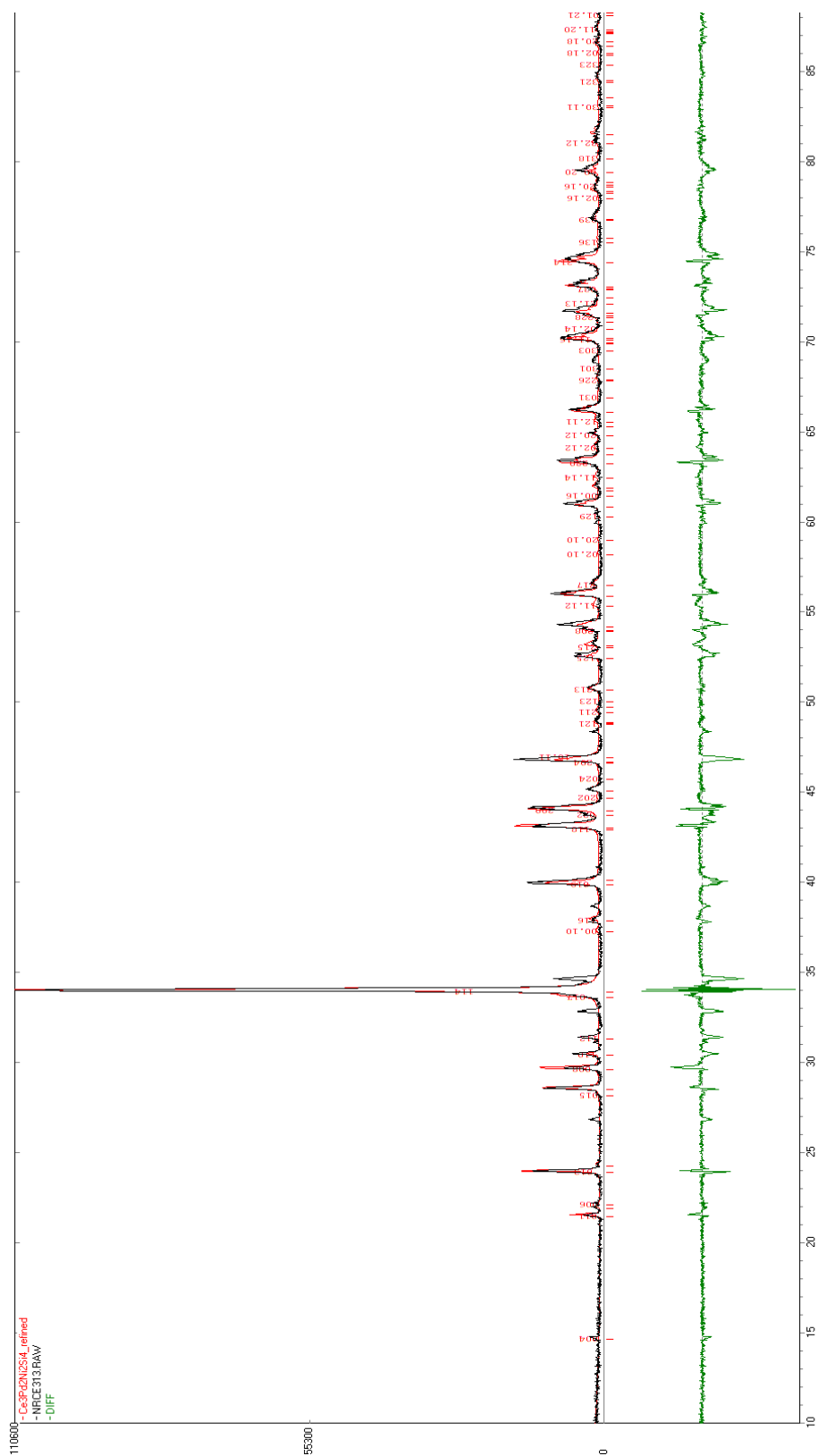


Figure B.5.: X-ray diffraction pattern of $\text{Ce}_3\text{Pd}_2\text{Ni}_2\text{Si}_4$. Small impurity peaks can be spotted at 27° , 33° and 35° .